

Title	Development of advanced 3D tissue models and O2 imaging methodologies
Authors	Jenkins, James
Publication date	2016
Original Citation	Jenkins, J. 2016. Development of advanced 3D tissue models and O2 imaging methodologies. PhD Thesis, University College Cork.
Type of publication	Doctoral thesis
Rights	© 2016, James Jenkins. - http://creativecommons.org/licenses/by-nc-nd/3.0/
Download date	2024-04-20 16:08:30
Item downloaded from	https://hdl.handle.net/10468/3660

Development of advanced 3D tissue models and O₂ imaging methodologies



A thesis submitted to the National University of Ireland, Cork

In fulfilment of the requirements for the degree of

Doctor of Philosophy by

James Jenkins

School of Biochemistry and Cell biology

National University of Ireland, Cork

2016

Head of School: Prof. David Sheehan

Supervisors: Prof. Dmitri Papkovsky and Dr. Ruslan Dmitriev

To my Family

Table of Contents

Declaration	6
Abstract	7
List of abbreviations	9
Chapter 1. Literature Review, 3D tissue models, their uses as disease models and analysis by the fluorescence imaging method	12
1.1 Introduction	12
1.2 Cell and tissue models	13
1.2.1 Pitfalls associated with 2D monolayer cell cultures compared to 3D	13
1.2.2. Scaffold free models, spheroids.....	16
1.2.3 Tissue slices	19
1.2.4 Scaffold-based 3D models	21
1.2.5 The future of 3D tissue models.....	23
1.3 Live fluorescence imaging	25
1.3.1 3D models and fluorescence imaging.....	25
1.3.2 Principles of fluorescence, intensity, lifetime, FLIM and PLIM.....	26
1.3.3 Fluorescent imaging dyes, probes, nanoparticles and biosensors.....	31
1.4 Fluorescent markers/probes for metabolic processes	34
1.4.1 Fluorescence-based pH probes	35
1.4.2 Fluorescence based NAD/NADP probes	37
1.4.3 Fluorescence based temperature probes	39
1.4.4 Monitoring intracellular calcium	43
1.4.5 Phosphorescent O ₂ dyes, sensors, probes	46
1.5 Importance of O ₂ imaging in cells and tissues	52
1.5.1 Effect of hypoxia on cells and tissues physiology.....	52
1.6 Summary	57
1.7 Thesis aims	57
Chapter 2. Materials and Methods	59
2.1 Materials	59
2.2 Cell culture	61
2.3 Preparation of O ₂ -sensitive 3D scaffolds	62
2.4 Growth and treatment of cells in the O ₂ scaffolds.....	62
2.5 Measurement of PtTFPP dye leaching using micro-plate reader	63

2.6 DNA transfection and hypoxia treatment of adherent cell culture.....	63
2.7 RNA extraction and PCR analysis	64
2.8 Production and analysis of spheroids	65
2.9 Protein extraction and western blotting.....	66
2.10 ATP and ECAR measurements	67
2.11 Immunofluorescence	68
2.12 Widefield PLIM microscopy	69
2.13 Confocal FLIM-PLIM microscopy	70
2.14 Data analysis and statistics	72
Chapter 3. Evaluation of novel photoluminescence based O₂ and temperature probes	73
Abstract	73
3.1 Constructing O ₂ -sensing scaffold structures for 3D tissue models	74
3.1.1 Preparation of O ₂ scaffolds and their sensing properties.....	75
3.1.2 Cell growth and viability in O ₂ -sensitive tissue scaffolds	77
3.1.3 Monitoring oxygenation of different cell types in O ₂ scaffolds	79
3.1.4 Monitoring gene expression changes in scaffolds because of depth-dependent deoxygenation	81
3.1.5 Metabolic cell stimulation in O ₂ scaffolds.....	83
3.2 Evaluation of conjugated polymer, nanoparticle-based O ₂ probe	86
3.2.1 Probe characteristics and optical sensor properties	86
3.3 Sulforhodamine-based temperature-sensitive nanoparticle probe (T probe) ...	89
3.3.1 Evaluating the cell staining properties and probe toxicity.....	89
Chapter 4. Physiological imaging studies with 3D tissue models and new probes	95
Abstract	95
4.1 Optimisation of spheroid models	96
4.1.1 Spheroid formation methods.....	96
4.1.2 Optimisation of the size and shape of 3D spheroid model using three different methods of production	97
4.1.3 Cell viability and proliferation capacity	98
4.1.4 Further evaluation of the Lipidure TM method.....	104
4.1.5 Staining of spheroids with nanoparticle probes and imaging of O ₂ and T gradients.....	105

4.2 Measuring O ₂ changes following drug stimulation in two different 3D models	110
4.2.1 PC12 cell aggregates seeded in O ₂ sensitive scaffolds	110
4.2.2 TPZ treatment of HCT116 tumour spheroids	112
4.3 Simultaneous monitoring of Temperature and O ₂ gradients in tumour spheroid	114
4.3.1 Measuring dynamic changes in O ₂ and temperature distribution	114
4.3.2 Destabilising the 3D structure of spheroids using HSP70 inhibitor cantharidin	115
4.3.3 Effect of metabolic stimulation on gradients of temperature and O ₂	117
4.4 Ca ²⁺ /Mn ²⁺ -ATPase, SPCA2 is regulated by O ₂ availability and affects Mn ²⁺ dependent cell cycle progression in colon cancer cells	121
4.4.1 SPCA2 is the only Ca ²⁺ transporting ATPase significantly affected by hypoxia and cell density	122
4.4.2 SPCA2 expression in 3D tumour spheroids	126
4.4.3 SPCA2 expression correlates with MIST1 and is dependent on HIF-1 α	128
4.4.4 SPCA2 is involved in regulation of cytosolic Mn ²⁺	130
4.4.5 SPCA2 is involved in the regulation of Mn ²⁺ -dependent cell cycle progression	134
5. General Discussion	137
6. Overall conclusion	145
7. Thesis outcome	148
8. Bibliography	151
9. Acknowledgements	185

Declaration

This thesis has not been submitted in whole or part to this or any other university for any degree, and is, unless stated, the original work of the author.

James Jenkins

September 2016

Abstract

Live cell imaging to monitor biological oxygenation and respiration are on the cutting edge of bioanalysis, including cell metabolism, bioenergetics, mitochondrial function and drug toxicity studies. This thesis presents the development and evaluation of new luminescent sensors and probes, optimisation of the tumour spheroid model and the various applications for these *in vitro* tissues combined with novel O₂ and temperature nanoparticle probes.

Here a new method for O₂ sensing was introduced, measuring extracellular oxygenation with solid state polystyrene scaffold (Alvetex™) impregnated with the phosphorescent dye PtTFPP. We assessed the toxicity, sensitivity and photostability of the O₂-sensitive scaffolds, as well as monitoring cell oxygenation following seeding with both PC12 and HCT116 cells. Using time-correlated single photon counting and phosphorescence lifetime imaging microscopy multiplexed with fluorescent markers and fluorescent staining we could non-invasively correlate lifetime values with toxicity and drug stimulation under mild imaging conditions (534 nm excitation, 650 nm emission).

Several novel O₂ and temperature-sensitive nanoparticle probes were evaluated. These probes displayed sufficient brightness, photostability and sensitivity. Furthermore, they showed minimal toxicity and were capable of penetrating 3D tumour spheroids in depth, showing efficient staining and even distribution, an advantage over previous probes which had limited diffusion across thick biological samples.

We applied the imaging methodology to the 3D spheroid model, investigating which method of formation from "free floating", "hanging drop" and Lipidure™, produced the most uniform, viable and metabolically active *in vitro* tissue. Probe staining

techniques were also optimised in the chosen spheroid model, ensuring monitoring gradients in various analytes was possible.

Numerous applications were improved and aided by the new O₂ measuring platforms. Combining the novel probes with our new 3D models we could monitor the effects of chemotherapeutic drugs in both seeded O₂ scaffolds and 3D spheroids. The nanoparticles were used to demonstrate the application of FLIM method for multi-parametric analysis of O₂ simultaneously with temperature and confirm the existence of temperature gradients in the 3D cell-based model. Finally, we applied the O₂ probe and its measurement via PLIM (phosphorescence lifetime imaging microscopy) method to elucidate the function of SPCA2 in human colon cancer HCT116 cells, grown in ambient and decreased O₂ levels. We could correlate SPCA2 upregulation with hypoxia in both monolayer and in spheroids. Furthermore, we discovered that SPCA2 is up-regulated by cell density, playing a role in Mn²⁺ transport and cell cycle progression in cancer cells.

Results show that the developed probes and techniques provide a useful tool for the highly sensitive imaging of intracellular and extracellular O₂, temperature and other important parameters. The new improvements allow for cell metabolism and mechanistic studies, as well as enabling us to study cell/tissue adaption to hypoxia and drug stimulation.

List of abbreviations

2D - two-dimensional
3D - three-dimensional
AntA - antimycin A
ADP - adenosine diphosphate
ATP - adenosine triphosphate
BrdU - 5-bromo-2-deoxyuridine
CAN - cantharidin
CoCl₂ - cobalt(II) chloride
CTX - cholera toxin, subunit B, Alexa Fluor 488 conjugate
DAPI - 4',6-diamidino-2-phenylindole
DIC - differential interference contrast
DMEM - Dulbecco's modified eagles' medium
DMOG - dimethyloxaloylglycine
DMSO - dimethyl sulfoxide
DNA - deoxyribonucleic acid
ECM - extracellular matrix
ECA - extracellular acidification
EGF - epidermal growth factor
ER - endoplasmic reticulum
FBS - fetal bovine serum
FCCP - carbonyl cyanide-4-(trifluoromethoxy)phenylhydrazone
FGF - fibroblast growth factor
FLIM - fluorescence lifetime imaging microscopy
FF - "free floating"
GFP - green fluorescent protein
HIF - hypoxia inducible factor
HSP - heat shock protein
LED - light emitting diode

LTR - LysoTracker Red

NAD - nicotinamide adenine dinucleotide

NIR - near-infrared

NP - nanoparticle

O₂ - molecular oxygen

OCR - oxygen consumption rate

OGB - Oregon green BAPTA-1

OM - oligomycin

OXPPOS - oxidative phosphorylation

PBS - phosphate buffered saline

PCR - polymerase chain reaction

PDL - poly-D-lysine

PLIM - phosphorescence lifetime imaging microscopy

PMCA - plasma membrane Ca²⁺ ATPase

PtTFPP - Pt(II)-tetrakis(pentafluorophenyl)porphine

RNA - ribonucleic acid

ROI - region of interest

ROS - reactive oxygen species

RT - room temperature

SCO2^{-/-} - lacking, SCO2 cytochrome C oxidase assembly protein

SERCA - sarco/endoplasmic reticulum calcium transport ATPase

SFM - serum free media

SPCA - secretory pathway Ca²⁺-ATPase

T - temperature

TBST - tris-buffered saline, tween 20

TCSPC - time-correlated single photon counting

TH - tyrosine hydroxylase

TMRM - tetramethylrhodamine, methyl ester

TPZ - tirapazamine

TR-F- time-resolved fluorescence

WT - wild type

Chapter 1. Literature Review, 3D tissue models, their uses as disease models and analysis by the fluorescence imaging method

1.1 Introduction

The cell constitutes the smallest, basic structural and functional unit of all living organisms, capable of replicating independently, often in the presence of neighbouring cells. Tissue is made up of a complex ensemble of similarly specialised cells and intercellular matter acting together to perform a specific function in the organism, with an organisational structure level intermediate between cells and a fully formed organ. Normal functioning of the tissue requires proper organisation and a healthy state for all its cells, while abnormalities in either of these features leads to a disease state. Cell models are too simplistic for gaining detailed understanding of a diseases effect on human tissue. Tissue models attempt to bring together single cells, forming structured, organised aggregates replicating the *in vivo* tissue microenvironment *in vitro*. 3D tissue models are useful in the study of cell metabolism and disease, mimicking the cellular interactions, signalling pathways and cellular morphology of natural tissues. They help elucidate mitochondrial dysfunction, drug delivery, disease mechanisms, cellular alterations and changes in gene expression, improving diagnostics and treatment and our overall understanding of tissue function.

1.2 Cell and tissue models

1.2.1 Pitfalls associated with 2D monolayer cell cultures compared to 3D

2D mono-layer is the most convenient cell culturing method, providing high viability and ease of use. 2D cultures are easier to manipulate, allow for the strict control of environmental factors and aid cell observation studies by conventional microscopy and biochemical assays. 2D models were instrumental in increasing our knowledge of cellular function, metabolism, signalling and many disease states. However, basic 2D monolayer cell cultures are poor models of the *in vivo* microenvironment. They are deficient in the extensive cell-cell and cell-extracellular matrix (ECM) signalling and prominent gradients of metabolites and bio-molecules typical for mammalian tissue *in vivo*. This limits the ability of 2D cultures to mimic natural differentiation, proliferation [1] metabolism and physiology of cells within tissue [2-4]. The disparity in structure leads to striking differences in morphology and gene expression [5-7]. Mono-layered cells also lack the interplay associated with an active, complex stroma [8]. Physical cell differences include flattening, stretching and metamorphosis of the cytoskeleton as a result of being grown on the surface of a cell culture flask [9] (Fig. 1.1). 2D proves to be a polarised model displaying a much greater number of binding proteins on the surface attached to the flask or dish [10]. Growth on a flat surface also ensures cells receive an even distribution of nutrients and growth factors from the media, an unrealistic distribution when compared to the natural gradients found *in vivo* [11].

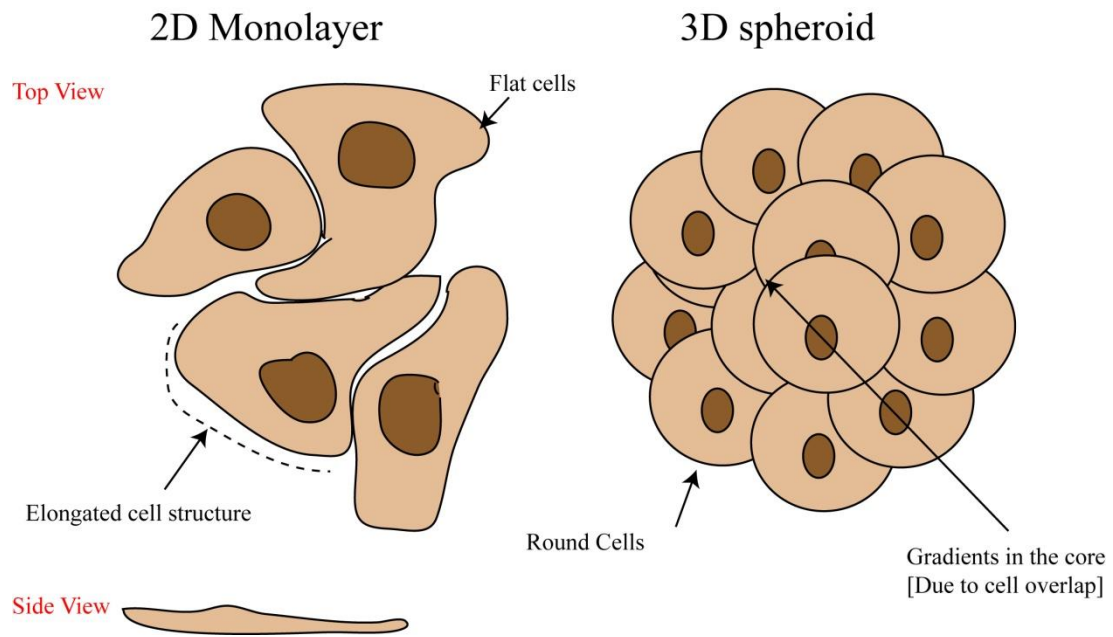


Figure 1.1 Simplified comparison of 2D and 3D cell models.

Furthermore, changes in the regulation of transcription and translation are associated with cell adaptation to its new un-natural *in vitro* microenvironment. Gene expression studies with breast, colon and lung have shown that there are up to 30% of genes differentially expressed in cell lines compared to the original native tissue [12]. Genes of particular interest are those associated with negatively controlling proliferation, noticeably down-regulated in 2D culture. [11]. The continued use of 2D culturing in the drug development industry may hinder progress in the field [13]. The failure of some drugs to pass phase 3 has been attributed to the poor effect and lack of efficacy of the drug on the unnatural 2D monolayer micro environment [11, 14].

Many of the pitfalls associated with 2D may be addressed by transferring studies to 3D tissue models. 3D models ensure cells are more closely aligned to tissue, with a more uniform spread of adhesion molecules [15]. These models have normal cell shape, structure and function with minimal interference from external stimuli (Fig.

1.1). They allow cells to form complicated interactions increasing cell signalling, local gradients of bio-molecules and cell-cell communication. Additionally they reduce stresses and responses that arise when cell lines must adapt to a flat environment [9]. The discrepancies that exist between 2D and 3D cell culturing are clearly shown in a diverse range of studies some of which we highlight here. For example it was possible to reverse the malignant phenotype of human breast cells by introducing integrin-blocking antibodies in 3D cell aggregates, a result not reproducible in the less physiologically relevant 2D cultures [16, 17]. Drug toxicity studies further highlight the importance of 3D structure and the heterogeneous microenvironment. Culturing cells in 3D tumour spheroids alters sensitivity to drugs, including cisplatin or doxorubicin [18]. This transformation in sensitivity can be attributed to the insufficient drug delivery [19], hypoxia experienced by cells in the spheroid core [20], cell-cell interactions aided by E-cadherin [21] and the production of extracellular matrix proteins combined with multi drug resistant pumps [22]. There are also those drugs which show greater effectiveness on 3D spheroids. PX-866 which inhibits PI-3 kinase subdues proliferation of the U87 glioblastoma, as well as HCT116 colon cancer cell spheroids [8, 23]. Significant differences in protein expression have also been observed in 3D cultures, compared to their 2D counterparts. Ovarian cancer cells cultured in 3D have exhibited a significant increase in the mRNA levels of $\alpha_2/\alpha_5/\beta_1$ integrins, a family of cell surface receptors as well as the protease MMP9 [24]. Protein expression changes have also been studied in non-cancer cell lines. The human submandibular salivary gland (HSG) has been transferred to 3D culture models to study salivary gland regeneration repair. HSG cells developed in 3D showed an increase in the production of acinar proteins, brought about via translational regulation [25].

The number of unrelated studies, displaying contrasting results for 2D culturing compared to 3D, highlight the importance of using a more physiologically relevant cell model. The incorporation of 3D tissue models into biomedical research, regenerative medicine and basic cell biology [26] is spreading, aided by the advancement of modelling techniques ensuring ease of production, manipulation and as a result a closer representation of *in vivo* tissue. The versatility of 3D models is apparent, being used for identifying biomarkers in breast cancers, through co-culturing in laminin-rich extracellular matrix [27] and more recently drug development and testing [28]. The number and complexity of available 3D tissue models are increasing. They can however be divided into two main categories, scaffold-based or scaffold-free systems [26].

1.2.2. Scaffold free models, spheroids

Scaffold-free tissue culturing involves the creation of tissues through self-assembly and the formation of multi-cellular aggregates, with cells forming their own extracellular matrix components [9, 29]. One common scaffold-free model is the spheroid. The overall spheroid morphology and shape are dependent on the cell line used [11]. In a study of spheroid formation using a panel of 25 breast cancer cell lines four distinct types of spheroid structures were identified [30]. The first, round type, displays strong cell-cell adhesion, with the nuclei organised around the centre of the colony, often having a lumen form in the centre [31]. Mass-type spheroids are spherical in shape but the nuclei are no longer organised and they develop strong cellular communication. They are often larger than their round counterparts, and despite over-expressing luminal keratin 8 and keratin 18, they lack a lumen [11]. The ‘grape like’ spheroid is loosely formed with less cell-cell interactions. The final type,

stellate, have cells with elongated bodies and invasive phenotypes, displaying the ability to bridge colonies and invade matrices [32].

Several methods are available for spheroid formation. In the simple "hanging drop" method the cells aggregate spontaneously under gravity in the droplet of culturing media [2, 33, 34]. The liquid overlay technique relies upon the suspension of cells in a non-adherent substrate, encouraging cells to aggregate and not attach [35] or growth of cells in stirring culture systems such as spinner flasks [36]. Spheroids may also be formed using non-adherent micro patterned surfaces [29]. The increased relevance of the spheroid model broadens its usage in high throughput screening of drugs and the production of complex tissue grafts [20, 37].

The ability of spheroids to mimic cell-cell and cell-matrix interactions, tissue contraction and condensation makes them useful for mechanistic studies. Thus, chondrocytes seeded in droplets to acquire the high density of chondrogenic condensations have been used to study the regulation of chondrogenesis by RAC1 and Cdc42 [38]. The role played by adhesion molecules may be examined in tumour spheroids which have shown greater resistance to some chemotherapeutic drugs compared to monolayer cultures. The expression of either the more prevalent negative E-cadherin or the wild type, in the form of Ewing Sarcoma tumour cell spheroids can decrease or increase resistance to chemotherapy respectively [39]. Intracellular adhesion proteins connexins and pannexins have also been studied [40], revealing Panx1 accelerates the formation and compacting of spheroid culture and helps develop a more complete F-actin cytoskeleton [41]. Necrosis, the initiation of programmed cell death in the absence of apoptotic markers, has also been observed in spheroids [42].

While spheroid technology began as simple formation of cell aggregates it has developed towards fabricating more complex and physiologically relevant, tissue like structures. As tissues are heterogeneous, it is important to ensure that the 3D microenvironment accounts for complex structures, different cell types and their interplay. Tissue structures have been replicated *in vitro* in spheroid models, including pancreatic tissue [43], cardiac muscle [44] and pituitary glands [45]. Challenges in engineering such constructs relate to their size and the gradients of nutrients and oxygen (O_2) in the tissue. Vascularisation of 3D tissue models and grafts can help to address this problem [46, 47]. The dense environment of co-cultured spheroids allows for the mimicking of the natural vascularised environment and thus support cell growth e.g. cardiac tissue [48], or pre-vascularised bone [49]. Simple vascular structures formed when spheroids produced using human MSCs were co-cultured with human umbilical vein endothelial cells (HUVECs) [50]. The engineering of such vascular networks help the survival of implanted cells [51] and development of the spheroid model. Vascular architecture within these spheroids will also help mimic the endosteal niche *in vitro* [29].

While vascularisation helps to improve the distribution of O_2 and nutrients, the existence of a hypoxic core and naturally forming gradients within large spheroids can be advantageous in anti-cancer drug screening [52] and the study of cellular responses to changing O_2 levels [53]. Spheroids are of particular interest in cancer research since they are made up of proliferating cells on the periphery and quiescent cells at the core [54]. Cancer cells can adapt to this absence of blood vessels, O_2 , and nutrients by halting cell cycle progression and becoming dormant. This cancer cell dormancy can lead to anti-cancer drug resistance, as the primary mechanism of action for cytostatic drugs is to attack proliferating cells. Multicellular tumour spheroids, which have these

naturally occurring dormant regions have been utilised to identify drugs that specifically target the dormant inner core [20]. The formation of larger more robust spheroids can lead to formation of a necrotic core, mimicking more closely the conditions of tumours *in vivo* [55]. They have been used to culture cancer stem cells and investigate cancer relapse induction [56]. Human colon tumour spheroids have highlighted the changes in gene expression between 2D and 3D, with 3D spheroids maintaining CD133 expression and showing increased survival following chemotherapy-induced apoptosis [57]. Ovarian cancer cell spheroids have the ability to self-renew and possess a more aggressive invasive phenotype [58]. Hypoxic-induced, cancer stem cell spheroid structures have been discovered *in vivo*, in the blood, contributing to metastasis [59]. Further development and improvement of spheroid models will no doubt ensure their continued use in biomedical research.

1.2.3 Tissue slices

Fresh tissue slices have been used to study individual tumour stages, grades and alternative slow and fast growing tumour subgroups [8]. The investigation of tissue responses to chemotherapeutic drugs and small molecule inhibitors have also been carried out [8, 60, 61], as well as identifying the location and migration of immune cells within tumours [62]. Tissue slices have been used as a platform for new anti-cancer treatments including oncolytic viral infection and gene therapy [63-65]. However, in order to maintain high viability, continued proliferation and tissue structure, slices can only be grown *ex vivo* for 3-7 days [8]. Even with the correct procedure for extraction and maintenance [66] this model displays high variability and inconsistency, even within tumours from the same entity [61] with noted changes in proliferation [67] and the overall cell make up [68]. This model also has problems

regarding the procuring of tissue material from patients and providing appropriate control samples [8]. The tissues are vulnerable to stresses and may lead to changes unrelated to the disease itself but because of surgery or handling, or changes in O₂, temperature and nutrient availability during its slicing and maintenance. These factors may influence drug sensitivity and results obtained while using them [8]. While they have their disadvantages tissue slices are not limited to tumour studies, with brain slices used extensively in scientific research, contributing massively to modern day neuroscience. They can usually maintain the architectural characteristics from the original tissue as well as preserving neurochemical activity and connectivity of synapses. Organotypic slice cultures have been taken from several brain regions, including the cortex, spinal cord and cerebellum [69]. However once again there are problems arising regarding slice preparation, with the “protective cutting” method leading to neuronal cell death, particularly in what is referred to as superficial layers [70]. The effect of this damage was apparent in a study carried out using thalamocortical slices from mice ranging from post-natal day 5 to day 20, monitoring the developmental decrease of neuronal chloride concentration. In contrast to the deeper in the tissue it was observed that there were elevated chloride levels in the superficial layers of the neocortical and thalamic brain slices in all ages, both susceptible to trauma. The possible reasons for this increase include disruption of the extracellular matrix and sectioning of neuronal processes [71].

Tissue slices derived from the liver, kidney and heart have also been used in several diverse studies. Liver slices were a popular *in vitro* model used to observe hepatotoxicity, testing the toxic effects of cocaine, endotoxin and paraquat to name a few. They also aided in research involving the metabolism of endogenous and exogenous substrates, most notably caffeine metabolism. Furthermore, lipogenesis,

gluconeogenesis and ureagenesis were all investigated in the liver. Kidney slices have been used to look at renal responses to toxicants and renal metabolism, as well as being important models in transport studies involving the kidney. Heart slices are appealing for research as normal cell-cell interactions are maintained. They have been employed in assessing toxicant-induced injury to myocardial tissue. Ventricular slices aided in work involving mechanistic studies of sodium pumps, vital for the contacting of the heart. Other studies looked at the effect of diet and age on these pumps [72].

1.2.4 Scaffold-based 3D models

Scaffolds are specially designed materials engineered to form a desirable environment for cellular interaction, mimicking extracellular matrix, helping form new *in vitro* tissue like structures. Scaffold based models involve the seeding of cells on a 3D matrix or the spreading of cells in a liquid hydrogel, followed by polymerisation. The common scaffold components include natural materials such as collagen [5] or synthetic material including polymers [73]. The important characteristics required are compatibility with cell culture, low toxicity and adhesion sites for cell attachment. Natural materials already contain adhesion sites and biocompatibility, while synthetic materials have a definite chemical composition and may be modified for improved cell differentiation [74] or adhesion [75] and more reproducible framework. Scaffolds may be further sub-divided into either hydrogels or solid scaffolds. The hydrogel method involves the encapsulation of cells in a loose hydrogel comprised of cross linked materials including agarose and collagen [76]. Use of these structures should be confined to short experimental periods, due to the challenges associated with nutrient delivery [77]. Solid scaffolds also have their merits as a readymade support structure aiding cells in their creation of models akin to natural tissue. Cells are simply

seeded onto an open pores structure. These scaffolds are of particular use when the cells must form well defined architecture, with layers of alternating cell types, e.g. in artificial skin grafts, with the scaffold actively contributing to the creation of layers of epidermal and dermal tissue [9]. Osteon structures have been produced using scaffolds produced via the electro-spinning method [78] while more porous scaffolds have been employed in the growth of equine keratinocytes [79]. Scaffolds themselves tend to be either fibrous or porous in their structure. Fibrous scaffolds are prepared by delivering a polymer jet through an electric field, collecting the resulting structure on a chosen surface [80]. Porous scaffolds have pores of defined shape and size, which can be predefined, produced using the particulate leaching method. The polymer is casted around beads called porogens, often a salt or saccharide which latter dissolves leaving behind the desired pores. Pore size can have a major effect on growth, for example larger unconnected pores can lead to the development of a heterogeneous culture of isolated cells within the 3D microenvironment [9, 81]. Scaffolds manufactured using biodegradable materials like poly(lactic acid) and poly (glycolic acid) and their copolymers [poly(lactic-co-glycolic acid)] have been applied to 3D modelling for tissue repair [82]. However, there is trepidation in their use for *in vivo* studies, as the degradation may lead to by-product release, adversely affecting the cells behaviour. Population of interior regions of scaffolds with cells is also challenging This problem may be overcome by using inert non degradable materials, such as 200 µm thick polystyrene membranes [83]. The sheer number of materials and production methods which can be combined and altered make scaffold materials a useful tool for *in vitro* tissue manufacture.

1.2.5 The future of 3D tissue models

An exciting new advancement for 3D modelling is bio-printing, which involves the patterning of biological products including cells and bio molecules to produce tissue mimicking constructs [84-86]. 3D bio-printing helps produce tissue mimicking constructs for transplantation [87], 3D heterogeneous structures for developmental biology [88] and drug screening [89], cellular and extracellular parts of a tissue through mimicking of specific cell structures and functions [86]. The earliest, method of bio-printing uses droplets to capture cells and non-living materials layered upon a suitable substrate [90]. This process can be carried out cheaply and with a high cell viability following printing. Laser bio-printing uses a laser beam to focus on a ribbon, exciting cells and collecting the 3D construct on a substrate facing the ribbon [91]. The extrusion method relies on an ejector system in conjunction with a three axis robotic stage [92]. A piston is used to transfer bio ink onto the appropriate building substrate [87]. Mimicking natural tissue with these methods requires an in depth knowledge of the cells physiology and cell-extracellular matrix interactions [93]. 3D microenvironments are reconstructed using natural materials such as collagen and fibrin, synthetics including polyglycolide, polyethylene glycol or hybrids that combine both [86]. The creation of vascular grafts via printing negate some of the problems associated with nutrient and O₂ diffusion. Vascular grafts have been printed combining multiple cell types including smooth muscle cells, endothelial cells and fibroblasts [94]. Bio-printing of skin tissue may be helpful in the development of topical drugs, studying of wound healing and dermal toxicology research [86]. An example of skin production was developed using fibroblasts and keratinocytes on a stable matrix using the laser method [95]. The printing of neural cells provides a model for new therapeutic approaches for Alzheimer's and Parkinson's [96] yet challenges remain due

to the complex nature of the multi layered brain, specifically in the medial and sagittal plane [97] Drug screening will no doubt benefit from 3D bio-printing, offering better predictive and cheaper results when compared to *in vitro* and animal screening. Furthermore it will provide the added incentives of personalisation of medicine and an increase in the number of drugs completing drug screening [86]. Drug screenings have been carried out using different bio-printing platforms including cell spheroids [98] and micro-fluidic systems [99]. In a more recent study a 3D lung for drug evaluation studies was produced using a valve based bio-printer [100]. 3D bio-printing has the potential to help make artificial tissue that is more physiologically relevant and will aid in improving our understanding of cell interactions and tissue formation.

Spheroids will continue to be an important research model in the future, particularly with advances in combining multiple cell types. Culturing tumour cells together with fibroblasts, monocytes, embryonic bodies or endothelial cells allow for spheroids with stromal architecture to be produced [8]. Importantly, stromal cells play a major role in cancer cell development, being associated with cell-cell communication, tumour growth, metastasis [101] and mammary epithelial cells. Thus, spheroids produced from MCF10A (normal human breast epithelial cell line), human mammary fibroblasts (HMF) and human adipose-derived stem cells (hASCs) expressed much higher amounts of α -casein mRNA, hinting at its role in differentiation of mammary epithelial cells [102]. Stroma-derived micro-environmental cues can reduce the effect of anti-cancer drugs. To study this phenomenon spheroids were produced using DLD-1 colon cancer cells combined with HS27A stroma cells. Results showed a reduced potency of the MEK kinase inhibitor Trametinib when compared to the control monospheroid model [103]. In another study, colorectal cancer cells (HCT116) were combined with primary normal dermal fibroblasts to monitor differences in response

to electrochemotherapy. Spheroids produced using only tumour cells were destroyed following electrochemotherapy, while those produced with normal cells survived. In the mixed spheroids only normal cells remained viable, with selective destruction of the cancerous cell line [104]. Co-culturing produces a more physiological model, showing promising results for drug stimulation studies.

Further advancements in co-culturing and bio-printing will aid in the production of more complex 3D tissue models capable of accurately mimicking *in vivo* conditions. They will no doubt become more widely used, increasing our knowledge of cell metabolism and disease, signalling pathways, gene expression, cellular morphology and functioning of natural tissues.

1.3 Live fluorescence imaging

1.3.1 3D models and fluorescence imaging

New *in vitro* tissue models must develop hand in hand with efficient new protocols, dyes and probes for their detailed characterisation, control or operation and analysis of cellular function during culturing. The list of key system parameters is large and includes O₂, pH, and calcium (Ca²⁺), viability, MMP, ROS, apoptotic markers, for which corresponding probes and measurement techniques are required. For multi-cellular structures and 3D tissue models live fluorescence imaging is one of the main techniques, which allows real-time monitoring of such structures and individual cells within with sub-cellular resolution. Development of new instrumentation and microscopy integration has helped overcome challenges associated with high resolution imaging in complex, thick tissues with high light scattering [105]. Developments include super-resolution fluorescence imaging coupled with either

single molecules [106], or photoswitchable probes, achieving dynamic imaging of specific structures in live cells with 30-60 nm spatial resolution [107], or the use of deep-tissue fluorescence imaging with time-reversed ultrasound-encoded light, capable of imaging depths of up to 2.5mm in biological tissues and decreasing background signals [108]. Fluorescence imaging has been extensively used to study the differentiation of 3D-stem cell models [109], increase the depth at which thick biological samples can be imaged [110], monitor cell viability in multi-cellular glioma spheroids [111] and analyse drug therapies on organoids, enabling the prediction of drug responses in breast cancer [112].

1.3.2 Principles of fluorescence, intensity, lifetime, FLIM and PLIM

Luminescence is an all-encompassing term for the emission of light, not related to high temperatures. Processes included under this heading are chemiluminescence, bioluminescence, fluorescence and phosphorescence [113]. In this chapter I will focus on the latter two. Fluorescence is the method of energy dispersal for the lowest vibrational energy level of the first electronically excited singlet state back to the electronic ground state, through the emission of photons. Absorbed light is usually of a shorter wavelength than the emitted light with the difference between the exciting and emitted wavelengths called Stokes shift [114]. Fluorescent lifetime (τ), is the average time a fluorophore stays in the excited state following excitation, [115-117] with a duration in the nanosecond (ns) range [118]. Fluorescence lifetime imaging microscopy (FLIM) relies upon the principles of fluorescence (Fig. 1.2).

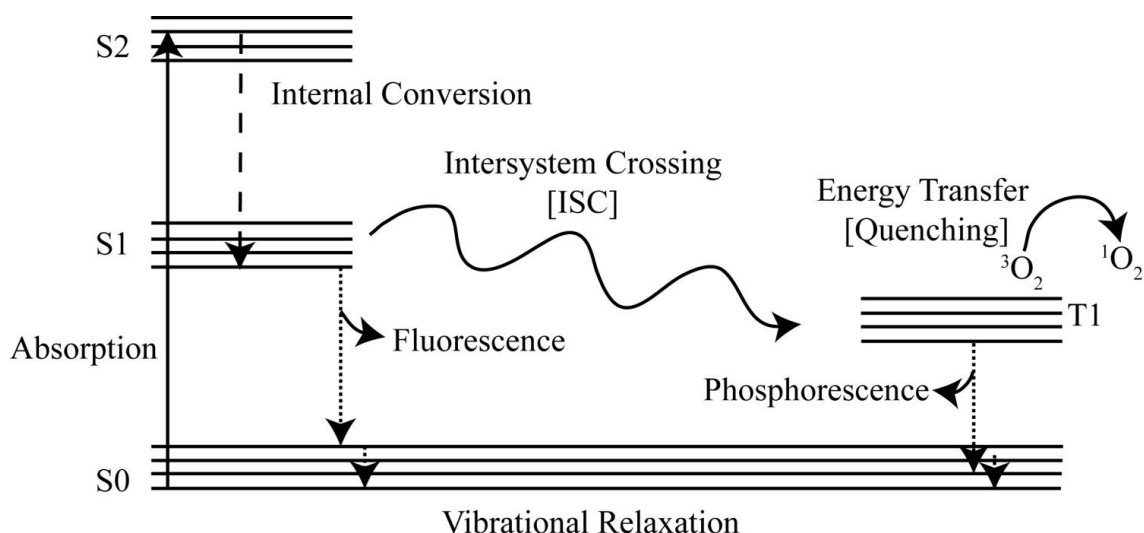


Figure 1.2 Simplified Jablonski diagram.

Phosphorescence Lifetime Imaging Microscopy (PLIM) is like FLIM but uses phosphorescent dyes. While fluorescence emission stops as soon as the excitation source is removed, phosphorescence displays more prolonged, longer lifetimes, in the microsecond (μs) range. Phosphorescent compounds are capable of retaining energy longer than their fluorescent counterparts [118]. When excited by a laser pulse the electrons are excited to the higher singlet energy levels with a subsequent filling of the triplet state using the intersystem crossing. The resulting lifetimes are longer as the transition from the triplet to ground state is quantum mechanically forbidden, requiring a change of spin [119]. These processes are described by the Jablonski diagram (Fig. 1.2), with singlet and triplicate states indicated by S and T. The loss of energy non-radiatively from the excited fluorescent molecule via collisions with other molecules is referred to as dynamic quenching. This process provides us with the opportunity to accurately measure various analytes using either fluorescence or phosphorescence imaging. Fluorescence lifetimes decrease following collisions with different analytes as a result of the formation of metastable complexes, resonance

energy transfer or electron transfer [118]. In the case of O_2 , a primary by-product of this quenching is the singlet O_2 , a short lived O_2 that usually returns to the ground triple state O_2 (Fig. 1.2). However it may also affect other molecules, including the dye, lipids, proteins and affect measurements of samples when using the sensor [120, 121].

Fluorescence microscopy has become an indispensable tool in the study of biological pathways, cell behaviour and for the investigation of cell processes in animals and tissues. This is in part due to its compatibility with living cells and tissues and the minimal invasiveness of the technique. The forerunner techniques in fluorescence imaging involve the use of confocal and wide-field microscopy, capable of resolving many of the cells organelles as well as providing information on other proteins and bio-molecules in the cell [122]. Widefield microscopy has developed through the improvement of microscope design, light filters, mirrors and objectives, aiding in faster detection of low-light fluorescence and improving greatly the signal to noise ratio. Widefield offers good XY dimension resolution and in most cases, requires the least amount of excitable light compared to other techniques, protecting the sample. Laser scanning confocal microscopy improves imaging resolution using beam steering optics, scanning mirrors and objectives which when combined focus the excitation light onto a specific region of the sample. Emission light is steered towards light sensing detectors through a pinhole, ensuring spatial filtering. The pinhole placed in the conjugate image plane to the focal point on the sample allows for optical sectioning, acting as a barrier to light coming from other focal planes. Confocal microscopy offers many advantageous additions including being compatible with 3D sectioning software, or facilitating data acquisition for techniques like Fluorescent Resonance Energy Transfer (FRET) and Fluorescence Recovery After Photobleaching

(FRAP) [123]. Fluorescence imaging can be conducted using either Intensity or Lifetime (FLIM/PLIM) imaging depending upon the required modality.

Intensity measurements are the most simple and straight forward method for monitoring photoluminescence. There are however associated disadvantages. Factors affecting intensity signals include concentration of the dye or probe, the photo-bleaching of the dye, auto-fluorescence and light scattering by biological samples, thus ensuring that its uses are primarily qualitative rather than quantitative. Optical interference, high light scattering and auto-fluorescence can all have drastic effects on the probes calibration in intensity mode, possibly leading to incorrect readings [120]. The improvement of intensity based measurements can be achieved using 'time resolved fluorometry' (TR-F), which fine tunes the signal-to-noise ratio paired with more reliable quantification and monitoring of the probes emission decay. This method measures luminescence intensity at specific times following a short excitation pulse. A delay time follows to extract the influence of short-lived scattering of light and auto-fluorescence after which the intensity signal is collected [120, 124, 125]. A corresponding simplified method referred to as rapid lifetime determination (RLD) [126], takes emission intensity signals (F_1 , F_2) at two different delay times labelled (t_1 , t_2) following the excitation pulse. Using these values, it is possible to calculate the lifetime of the probe using the following formula:

$$\tau = \frac{t_2 - t_1}{\ln \frac{F_1}{F_2}}$$

Fluorescence polarization anisotropy (FPA) is a technique used to study molecular interactions, enzymatic activity and for high throughput drug screening. FPA relies on the fact that light emitted by a fluorophore has unequal intensities along different

axes of polarization i.e. the polarization of a fluorophore is inversely related to its molecular rotation, driven by Brownian motion, affecting the anisotropy/decay values. The anisotropy values are not dependent on the concentration of the fluorophore. FPA can be quantitatively measured by taking the difference of the emission light intensity parallel and perpendicular to the excitation plane, normalised by fluorescence emission intensity [127, 128].

Although intensity measurements are useful a more advanced and accurate means of measuring fluorescence in complex biological samples is via fluorescence lifetime imaging. The advantage of lifetime imaging over the intensity imaging method is that results are not dependent upon the method of measurement. It is not affected by the excitation of the wavelength, light exposure or photo-bleaching as well as being independent of the intensity and concentration of the fluorophore [129]. Luminescence lifetime refers to the average amount of time a molecule stays in its excited state before emitting a photon, returning to the ground state. The lifetime of the fluorophore is associated with the energetically unstable state and as such makes the fluorescence lifetime sensitive to external factors including temperature, polarity and the presence of fluorescence quenchers [118]. Often the energy absorbed with the photons is lost because of quenching i.e. the dissipation of energy, leading to a decrease in fluorescence lifetime. Quenching by environmental factors like temperature and polarity lead to adjustments in fluorescent lifetime through conformational changes. An alternative means of quenching involves the reversible changes through electron distribution in the excited state [118]. Lifetime measurements can be classified into either phase modulation or time domain methods. Phase fluorimetry involves the excitation of a sample with an intensity modulated light

source at different time intervals with the emission phase shift (Φ) of the luminescent signal measured and used to calculate lifetimes using the equation:

$$\tau = \frac{\tan(\Phi)}{2\pi\nu}$$

where ν is the excitation frequency. There may be issues regarding auto fluorescence and light scattering when using this method for complex biological samples. Time domain technique involves the excitation of the chosen luminophore using short pulses to accurately measure lifetime values. It directly measures the dyes decay curve using a time gated detector, ensuring the detector gate time follows the excitation. Time correlated single photon counting (TCSPC) detects the arrival time of individual photons, emitted after a short surge of excitation, re-constructing a complete decay curve. This method provides high detection sensitivity, accurate lifetime measurements and when combined with confocal microscopy the ability to conduct optical sectioning [130].

1.3.3 Fluorescent imaging dyes, probes, nanoparticles and biosensors

A reliable fluorescent dye must possess a number of pre-requisite properties: high fluorescence quantum yield and molar extinction coefficient, long wave absorption and emission ranges, good photo-stability and selectivity [131]. Traditional xanthene dyes such as rhodamine B and Fluorescein-5-isothiocyanate (FITC) are used in many cell and molecule labelling experiments [131, 132], however the latter has low photo-stability. This can be circumvented through the introduction of versatile substitutions to the original dye scaffold [133]. Thus, sulfonated rhodamine and cyanine dyes displayed increased brightness, hydrophobicity, stability in various pH and decreased

aggregation [131]. Newer dyes excitable in the Near Infra-Red (NIR) [700-900 nm] [134] range are useful for *in vivo* imaging due to the increased depth the fluorescence can penetrate the tissue sample, >100-300 μm in some cases [135, 136]. Cyanine dyes have tunable spectra ranging from 400-800 nm through the addition of vinylene units [131]. Difluoroboron dipyrromethene dyes (bodipy, 4-bora-3a,4a-diaza-s-indacene) also have this NIR range, good solubility and optical properties [133, 137]. The widely available methylene blue fluorophore used in the staining of tissues for fluorescent guided surgery [138] has low toxicity, water solubility and fluorescence in 600-900 nm i.e. NIR range.

The coupling of fluorophores with cancer-specific moieties, such as folate, cyclic arginine-glycine-aspartic acid (cRGD) peptides or antibody fragments [131, 139, 140] allows imaging of tumours *in vivo*. Some heptamethine dyes, such as IR-808 and IR-783, naturally accumulate in tumours even without chemical attachment of tumour specific ligands [141]. Other fluorescent probes only emit light or become active when they contact the target tissue under pre-ordained conditions [142]. The protease activatable Cy5.5-based fluorochrome is triggered when its non-fluorescent internal quencher is cleaved by the proteolytic enzyme, primarily located in the tumour [143-145] producing the fluorescent signal in the tumour microenvironment.

Nanoparticle-based (NP) fluorescent probes have advantages over small molecule dyes, particularly allowing incorporation of high concentration of fluorophores, increased retention in cells and reduced degradation. Furthermore, in NP structures, fluorescent reporter dye can be protected from interactions with the biological environment and can be coupled with targeting moieties. Fluorescent NP probes can be manipulated to ensure biocompatibility, biodegradability, low toxicity and improved signal-to-noise ratio [131]. NPs can be produced with known, specific

structure, composition and size and surface charge and chemical groups ensuring specific targeting and manipulation [146, 147]. Common polymers used in NP probes include poly(lactic-co-glycolic acid)(PLGA) and poly(ϵ -caprolactone)(PCL), both displaying biocompatibility and stability [131], and functional groups for dye attachment, such as chitosan [148, 149].

Techniques used to embed fluorophores in the NP structures include the physical trapping of the dye molecule into the hydrophobic core. Another method involves in situ polymerisation of monomers in an emulsion which creates nanostructures. Emulsion polymerisation works by forming oil droplets containing the monomer units that are then stabilised in water by surfactants [150]. The covalent attachment of the fluorophores to the polymer backbone ensures no leakage as well as reproducible dye loading into nanoparticles [131].

Several key parameters determine NP behaviour and analytical performance as probes. Size is important, with small diameter of less than 30 nm showing efficient cell uptake but a risk of being cleared from the cell. Larger sized nanoparticles >200 nm show a decrease in cell internalisation and accumulation in the liver and spleen [151]. Shape can also affect the uptake of probes into cells, with rod shaped nanoparticles entering cells quicker than spherical ones [152]. The nanoparticles surface must also be considered, regarding its charge, hydrophobicity, ligand and polymer attachments which will affect the interaction of the probe with cells and its surrounding microenvironment [131]. Particles with a positive charge have been shown to have higher uptake into cells via endocytosis due to increased interaction with the negatively charged cell membrane, but have disadvantages including non-specific interactions and localising in undesirable locations within the cell [151, 153]. Negatively charged nanoparticles avert problems with non-specific interactions but

have a lower cellular uptake [153]. Like negative nanoparticles, neutral nanoparticles have lower cellular uptake when compared to positive nanoparticles as a result of reduced interactions with the cell membrane [153]. Fluorescent dyes for imaging have shown to be more effective with improved results when introduced to NP.

1.4 Fluorescent markers/probes for metabolic processes

Fluorescent/phosphorescent lifetime and intensity markers and probes have been used extensively in the field of metabolic imaging. They are being applied to measure the distribution of numerous important analytes within cells and tissues including O₂, Ca²⁺ and NADH as well as having the capabilities to monitor changes in temperature and pH. These parameters are closely linked to this thesis material and will be covered in-depth in this introduction. It is important to highlight, fluorescent sensors are not limited to these examples and are capable of measuring many other molecules including glucose [154] and lactate [155]. Fluorescent nanoparticles, produced using organic fluorophores in a polymer matrix are important in the fields of *in vivo* cancer imaging [131], disease diagnostics, use as chemo-sensors and for monitoring environmental changes [156]. FRET (fluorescent resonance energy transfer) based sensors rely on the principle that energy can be transferred from a donor to an acceptor molecule if the donors' emission spectrum overlaps with that of the acceptor excitation spectrum. They have proven to be popular, being used as indicators for protein interactions [157].

1.4.1 Fluorescence-based pH probes

Cytoplasmic pH is highly regulated in eukaryotic cells, maintained at between 7.0-7.4 via an ion transport system and the cytosol's ability to act as a pH buffer. pH is of utmost importance for enzyme activity, each having an optimum in which they function most efficiently, for example phosphofructokinase, the rate limiting enzyme in glycolysis increases its activity significantly with a small rise in pH [158]. It has also been shown to be critical for controlling cell cycle and as a result the proliferation of cells [159]. Abnormal pH leads to improper cell functioning, growth and division, being implicated in common diseases like cancer, and Alzheimer's [160], with an increase by a minimum of 0.4 pH units observed in multi-drug resistant cells [161]. An increase is also observed in DNA and RNA production following a rise in pH within the physiological range [158]. The numerous cellular functions controlled by pH make it a prime candidate for probe development, to more accurately measure its changes within cells. Fluorescence lifetime imaging can be used to determine pH values in cells and tissues, as the protonation of the fluorophore can lead to shifts in lifetime values. However, issues arise as the fluorescence lifetime of many fluorophores are not sensitive to change in the pH region (pH 4.8-7.4) seen in normal cells. Exceptions include fluorescein based indicators, such as 2',7'-bis(2-carboxyethyl)-5-(and-6)-carboxyfluorescein, displaying lifetimes ranging from 2.75-3.9 ns for pH 4.5-8 respectively [162, 163]. Fluorescent imidazoles lifetimes range from 0.3-0.5 ns, for their protonated and deprotonated states [164]. These fluorophores can be utilised for both ratiometric and direct pH measurement following calibration. Recently acid sensitive fluorescent nanoparticles which emit in the near-infrared (NIR) have also been shown to have pH sensitive lifetime values in the physiological

range [165]. The fluorescence based NIR probe LS482 displays pH sensitivity and distinct lifetimes for both acidic and basic conditions [162].

Polymer microcapsules containing SNARF-1-dextran, a pH sensitive conjugate have been successfully introduced to both MB-435S breast cancer cells and NRK fibroblasts, via adsorptive endocytosis, before storing them in endocytotic vesicles. SNARF-1 has a pH-dependent emission shift, shifting from green to red fluorescence in acidic and basic conditions respectively, allowing for measurements of pH in the range 6-8. These microcapsules enabled monitoring of pH changes from the cell media (alkaline) to the endosomal/lysosomal cellular compartments (Acidic), with minimal toxicity upon internalisation of the capsules into the cells [166]. SNARF has also been used in numerous other biological studies measuring intracellular pH, introduced into many cell types including lymphocyte murine B cell line A20 [167], single type-1 cells isolated from the carotid body of neonatal rats [168], and adult cardiac myocytes [169] to name a few.

Further works produced fluorescent pH indicators displaying high stability as well as emission in the NIR, produced using BF₂-chelated tetraarylazadipyromethene dyes (BODIPY). The emission in the NIR has many advantages, reducing background signals and auto-fluorescence, lowering light scattering in samples as well as increasing the penetration depth at which the probe can be imaged [170]. More recently further BODIPY based fluorescent pH probes for bio imaging have been developed, displaying long wave emission in the far-red and NIR spectral range (650-900 nm). The dyes are highly fluorescent, have intense absorption and high fluorescent quantum yield, are insensitive to polarity and pH and display good photo-stability making them ideal for biological studies. Thus, far red and NIR probes based on BODIPY dyes have been designed for common targets including pH, metal ions, and

oxidant species. These pH-sensitive probes have a proton receptor, usually a N-alkylated moiety, which acts as an electron donor, quenching the fluorescence lifetime via photo-induced electron transfer (PET) or intra-molecular charge transfer ICT [171]. These studies demonstrate the value of using fluorescence imaging as a reporting method to both monitor and explain pH mediated events within cells.

1.4.2 Fluorescence based NAD/NADP probes

NADH and NADPH are the major endogenous fluorophores present in cells, playing a role in cell metabolism, reductive biosynthesis, cell signalling, immunological function, aging and apoptosis. In broad terms, NAD^+ is primarily involved in regulating energy production, driving ATP generation in the cytosol by glycolysis and in the mitochondria via oxidative phosphorylation, while NADP^+ is primarily involved in antioxidant defence and free radical generation. Both act as "electron carriers". Defects in these pathways can lead to diabetes, neurodegenerative diseases and cancer. Because of this, the measurement of the reduced forms NADH and NADPH can be a good indicator of the functional status of the cell and tissue. Both possess their very own intrinsic fluorescence due to the presence of fluorescent biomolecules [162, 172]. In many cell types the pool of NAD is larger than NADP. NADP as an electron donor is mostly needed in a reduced state ensuring a high $\text{NADPH}/\text{NADP}^+$ ratio, while NAD as an electron acceptor is maintained in an oxidised state with a low NADH/NAD^+ ratio. Issues arise however as the light absorption properties of NADH and NADPH are identical, with a spectral peak at 340 nm, and emission spectra at 460nm, which give a combined signal often referred to as NAD(P)H. Thus, they cannot be distinguished based on fluorescence lifetimes, however steps are being taken to find FLIM based methods for separating the two. It was shown that enzyme-bound NADPH has a much

higher lifetime value than enzyme bound NADH. From this it was determined that bound NADH and bound NADPH have finite, distinct lifetimes in the cell with the relative contribution of each cofactor in the combined fluorescence signal could be calculated. Using two-photon excitation at 700 nm and a 435-485 nm detection window, the intracellular fluorescence lifetimes of NADH and NADPH were predicted to be 1.5 ± 0.2 and 4.4 ± 0.2 ns respectively, a pattern that was seen across a number of cell types including isolated ventricular cardiomyocytes and neurons in culture or brain slices [173]. It must also be considered that imaging of NAD(P)H may require either a UV laser or two-photon excitation, as a result of their blue-shifted absorption wavelength [172]. The ratio of NADH/NAD⁺ is key to understanding the redox state of cells and tissues, shown to be important in regulating numerous enzymes, such as dehydrogenases, polymerases and ADP-ribosyl cyclases [174]. Very recently genetically encoded fluorescent probes have been created that can measure the NADH/NAD⁺ redox state. This was made possible using the Rex family of transcriptional repressors, which are extremely sensitive to deviations in NADH in cells, allowing for the measurement of NADH/NAD⁺ ratios in both the mitochondria and cytoplasm [174]. NAD⁺ also acts as an essential substrate for sirtuins and poly(adenosine diphosphate-ribose) polymerases, enzymes localised in the nucleus, cytosol and mitochondria, with fluctuations in NAD⁺ regulating their activity. To monitor the changes in free NAD⁺ a fluorescent biosensor has been developed [175], made up of a fluorescent protein (cpVenus) combined with a NAD⁺ binding domain, that uses NAD⁺ as a substrate exclusively. When the NAD⁺ binds, it decreases fluorescence in a dose dependent manner, a process which is also reversible increasing fluorescence upon elution of NAD⁺. This new probe was used to monitor the pools of NAD⁺ and dynamic changes in the nucleus, cytoplasm and mitochondria of both

HEK293T and HeLa cells [175]. Measuring the amount of reduced NADH inside the mitochondria can act as an indirect method for evaluating O₂ supply within cells [176]. The NADH auto-fluorescent signals [177, 178] change as a result of O₂ deprivation, a phenomena measured in monolayer single cells, tissue slices and *in vivo* [176]. As an indicator of O₂ supply, NADH auto-fluorescent imaging has aided studies looking at the adverse effect on epidermal cells from *ex vivo* human skin following O₂ deprivation [179]. Using the less harmful method of Two-photon excited fluorescence (TPEF) in the near infrared spectrum it was possible to increase both deeper penetration for *in vivo* measurement of mitochondrial NADH fluorescence as well as allow for lengthier imaging sessions. This aided the study of how protein bound and free NADH behaved in rat skin following ischemia [180]. Both NAD⁺ and NADP⁺ are crucial to many important cell pathways and as such it is of great importance to produce probes capable of measuring them individually. Great leaps forward have been made in this regard using new fluorescent based probes and methods.

1.4.3 Fluorescence based temperature probes

The maintenance of temperature within cells is vital for the governing of almost every cellular biological interaction [181-183]. Temperature distributions within a cell can be an indicator of the thermodynamics and cellular functions of different cell organelles [184]. A rise in cellular temperature as heat production increases in cancerous cells is a common occurrence [185]. In contrast to conventional thermometers, measuring temperature using fluorescent probes provides a promising new method for analysing the distribution of intracellular temperatures and studying temperature dynamics at a molecular level [186-188]. Probes developed for this purpose must satisfy several criteria to be deemed successful, including high

temperature resolution, high brightness, biocompatibility, display stability with no changes in lifetime because of pH or surrounding bio molecules and concentration. This decreases the number of viable candidate probes that can efficiently measure intracellular temperature distribution [189]. Thermal infrared imaging systems [190] are useful in medical imaging but have limited spatial resolution. Fluorescence imaging and T-sensing probes can overcome these limitations ensuring quantitative measurement and imaging of cell and tissue gradients in real time in 2D and 3D [66, 191]. Recently several optical sensors capable of measuring temperature using fluorescent signals have begun to emerge. A newly developed fluorescent polymeric thermometer (FPT) has been shown to be photostable, cell permeable and capable of monitoring temperature (25-40 °C range) in many mammalian cell lines including HeLa, COS7 and NUH/3T3 via FLIM. The probe relies on a poly(N-n-propylacrylamide) (polyNNPAM) temperature sensitive unit, an ionic (potassium 3-sulfopropyl acrylate, SPA) and a water-sensitive fluorescent unit (N-(2-[(7-N,N-dimethylaminosulfonyl)-2,1,3-benzoxadiazol-4-yl](methyl)amino) ethyl-N-methylacryamide, DBD-AA). The polyNNPAM unit has an extended conformation due to hydrated amide linkages at low temperatures, which weaken and shrink at higher temperatures, while the DBD-AA fluorescence is quenched in the presence of water molecules. Thus, the fluorescence increases at higher temperatures. The SPA unit increases hydrophobicity, preventing aggregation of the probe in cells. The FPT successfully entered the cells and diffused throughout, including the cytosol and nucleus. It did however show cytotoxicity at high concentrations, inhibiting cell proliferation and cell adhesion [192].

Intracellular temperatures have also been measured using green fluorescent proteins, ensuring biocompatibility, high resolution imaging and fast read out. The concept

upon which this GFP measurement is based is the measurement of fluorescent polarization anisotropy (FPA) [193]. Fluorophores illuminated by linearly polarized light re-emit some polarised fluorescence as a result of the random orientation of the molecular dipoles [194]. Increasing the temperature leads to acceleration of the Brownian rotational motion, a subsequent loss of memory of the incident light polarization and thus an increasing number of re-emitted photons. This in turn causes a decrease in PFA [193]. In short increased temperatures decrease anisotropy, with much more emission light intensity being lost to rotation. By transfecting live HeLa and U-87MG cancer cells with GFP, non-tagged proteins throughout the entire cell, it was possible to map temperature during and following stimulation using a heating laser. This method shows potential for studying the heating changes that occur during cellular processes at a single cell level [193]. The fluorescent dye rhodamine is sensitive to changes in temperature as well as displaying high brightness and excitation bands in the visible range [195, 196]. The most popular dye used in laser-induced fluorescence (LIF) temperature measurements is rhodamine B (RhB), predominantly used in micro-fluidic systems [197, 198]. Fluorescence lifetime change in response to temperature are due to a drop in rhodamine B emission quantum yield as temperatures increase, caused by the rotation of the diethylamino groups present on the xanthene ring [196, 199]. The measuring of temperature with RhB probes is made possible via emission lifetime measurement or ratio metric evaluation using intensity values [200]. The temperature sensitive rhodamine B dye has been incorporated into latex particles, displaying high fluorescent signals, with a linear and reversible calibration for temperatures in the range 30-50 °C. These nanoparticles show promise in the study of temperature changes in biological, micro-fluidic and micro-electrical systems [196]. RhB due to its non-toxic effects in concentrations of around 40 nM [200] has also been

used to measure the temperature changes that occur in rat tendons following stimulation with radiofrequency radiation [201].

FLIM has also been utilised to directly monitor temperature changes within cell organelles using both the small molecule-based fluorescent thermosensor comprised of the small molecule ER thermo yellow (compound BDNCA346) [202] and the fluorescent protein mCherry. ER thermo yellow specifically locates to the ER, and proved to be cell permeable, photostable, is independent of pH and viscosity and doesn't aggregate making it possible to measure Ca^{2+} -induced heat production in real time in microtubules. The lifetime of the ER thermo yellow sensor decreased with temperature increase when measured in HeLa cells between 23-40 °C, forming a linear relationship between temperature and lifetime [202]. Expressing mCherry via transfection was used to examine temperature changes in the cytosol of C2C12 myotubes. Like the ER thermo yellow the mCherry has a linear relationship between fluorescence lifetime and temperature. However ER thermo yellow displayed advantages over mCherry including higher incorporation into cells, with mCherry showing low expression efficiency [203].

While new T probes look like a promising method for temperature measurement, their performance is still being compromised by aggregation, cross sensitivity, poor cell staining, viscosity and unstable calibrations. This can lead to misrepresentation of temperature gradients, making it necessary to carry out strict evaluation of possible measurements in cross interference in newly developed probes with various biological models.

1.4.4 Monitoring intracellular calcium

Ca^{2+} present in both the cytosol and different cellular organelles including golgi and endoplasmic reticulum (ER) is important for intracellular signalling pathways. It is stored primarily (95%) in bone with the other portion (5%) in dynamic equilibrium, ensuring cellular Ca^{2+} homeostasis. Ca^{2+} is involved in charge transfer across biological membranes through functioning of ion channels, in microtubule assembly and disassembly by inducing microtubule depolymerisation, and acts as a positive modulator of epithelial and mesenchymal cell proliferation by regulating DNA synthesis. Ca^{2+} is also critical in cell-cell adherence, muscle contraction, metabolic regulation and ensuring communication between cells is possible [204]. There is a 10,000-fold gradient of free Ca^{2+} that exists across the plasma membrane and similar gradients between ER compartments and the cytosol. Cytosolic Ca^{2+} signalling cascades involve the rapid movement of Ca^{2+} ions down an electrochemical gradient across the plasma and ER membranes. Ca^{2+} entry to the cell is mediated by numerous Ca^{2+} -permeable channels including voltage-gated L-type and transient receptor potential channels with gating mechanisms including ligands, mechanical stress and temperature changes channels. Ca^{2+} mobilization is mediated by two families of Ca^{2+} release channels, the ryanodine receptor (Ryr) and inositol 1,4,5-trisphosphate receptor (IP_3R). ER depletion stimulates store operated Ca^{2+} entry, mediated by STIM1 on the ER and Orai1 on the plasma membrane. Ca^{2+} homeostasis is achieved by extrusion across the plasma membrane by $\text{Na}^+/\text{Ca}^{2+}$ exchangers and Ca^{2+} -ATPase and resequestration into the store by the ER Ca^{2+} -ATPase [205].

Hypoxia leads to an increase in Ca^{2+} concentration in the cytosol. This increase is brought about by several pathways including voltage-operated Ca^{2+} channels, reverse mode of the plasma membrane $\text{Na}^+/\text{Ca}^{2+}$ exchanger and through a non-specific

membrane pathway [206]. Hypoxia in cells also leads to membrane depolarisation, increasing intracellular Ca^{2+} . This is mediated by inhibition of the O_2 -sensitive potassium channel, Kv1.2 and the up-regulation of the α -subunit of the Kv1.2 channel or K^+ channels such as Kv1.5. The depolarisation induced inhibition of the Kv channels activates voltage-gated Ca^{2+} channels, leading to an increase in $[\text{Ca}^{2+}]_i$ [207]. Ca^{2+} signals are produced by sudden increases in Ca^{2+} ion concentration inside cells. One of the most important things to consider when selecting a Ca^{2+} -sensitive dye is its affinity for Ca^{2+} . The dissociation constant (K_d) must be selected as appropriate for the concentration of Ca^{2+} in specific compartments. For cytosolic Ca^{2+} measurements, where values of 100-1000 nmol L^{-1} can be expected, a dye such as fura-2 with a K_d of 225 nmol L^{-1} is needed. However for measuring Ca^{2+} in the ER where the concentration will be approximately 50-300 $\mu\text{mol L}^{-1}$, dyes like Mag-fura with K_d values of 30-50 $\mu\text{mol L}^{-1}$ are better [208]. Ca^{2+} indicators capable of fluorescence constitute the largest single application of fluorescence detection in living cells [209]. Fluorescent imaging coupled with fluorescent Ca^{2+} indicators advanced the field of research of the Ca^{2+} signalling pathway with a high degree of spatial and temporal resolution. These imaging approaches have been used in numerous tissues, organs and animal models, reviewed extensively in [210-213].

Fluorescent Ca^{2+} indicators are based on genetically encoded fluorescent proteins [214] or small fluorescent organic molecules [215]. Many of the dyes on which these probes are based emit green fluorescent signal, including Oregon Green 488 BAPTA-1 and calcium Green-1 [216]. BAPTA a chelating group has high Ca^{2+} binding affinity, which following fusion to a fluorophore producing a fluorescence spectral shift in response to ion binding without diminishing binding affinity [209]. Ca^{2+} probes that emit red fluorescence include Rho-2 based on a rhodamine derivative [217]. These red

emission probes based tend to locate to the mitochondria due to their cationic nature limiting measurement of Ca^{2+} changes to mitochondria only. New fluorescent probes have been developed that emit in the red spectral region, displayed high cell membrane permeability and high fluorescence and also has the ability to measure cytoplasmic Ca^{2+} [216]. Another FLIM base probe capable of measuring intracellular Ca^{2+} is called G-CaMP, based on a single green fluorescent protein (GFP) molecule with a high affinity for Ca^{2+} . The probe contains calmodulin, which when bound to Ca^{2+} undergoes a conformational change, changing fluorescent intensity signals. The probe itself displayed a high signal-to-noise ratio, capable of measuring dynamic intracellular changes of Ca^{2+} [218, 219]. This original sensor has since under gone many upgrades, improving its quantum yield [220] and signal to noise ratio [221].

The most popular FRET based sensors for Calcium sensing are the Cameleon sensors. They are made up of the calmodulin protein, fused to the calmodulin-binding domain of myosin light chain kinase M13 placed in between two fluorescent proteins like CFP and YFP. When calcium binds to the calmodulin it induces a conformational change, the M13 chain then binds to the calmodulin protein ensuring the two fluorophores are close enough to transfer energy. Other FRET based sensors use Troponin C as the calcium-binding moiety. Troponin C is selectively expressed in skeletal muscle cell; thus, it doesn't influence normal cell processes when introduced to cells not derived from myocytes. The TN-L15 sensor is made of a chicken skeletal muscle Troponin C segment in between the fluorescent proteins ΔC11CFP and YFP. To improve the efficiency of energy transfer, 14 amino-acids of the N-terminus of the Troponin C fragment were removed. Binding of calcium to the binding sites lead to a conformational change, bringing the fluorophores close together, again allowing the transfer of energy. The FRET biosensor called mTFP-TnC-Cit was constructed by

replacing the CFP fluorophore within TN-L15 with mTFP1. This addition ensured the FRET sensor fits well to a two-component donor fluorescent decay model allowing easy fitting, less sensitivity to changes in environmental factors like temperature or emission wavelength, making it more suitable for FLIM experiments compared to CFP-based probes [222].

The wide use of fluorescence based imaging methods has ensured great leaps have been made in the knowledge of Ca^{2+} signalling pathways and the role of Ca^{2+} dynamics within the cell.

1.4.5 Phosphorescent O₂ dyes, sensors, probes

O₂ is required for the production of cellular energy reserves via ATP formation, energy required for many cellular enzymatic reactions and physiological functions [223]. A decrease in the concentrations of O₂ or an imbalance between the available O₂ and cell consumption can lead to disease and a decrease in cell/tissue viability [224]. O₂ can be considered a marker of cell viability and metabolic activity in cells and organisms that consume O₂. The most popular and widely used O₂ probes rely on the measurement of photoluminescence, specifically phosphorescent signals in relation to O₂ quenching. These probes are continually being developed and improved due to the high demand for monitoring *in vitro* and *in vivo* O₂. Quenched phosphorescence imaging for O₂ measurement has seen an increase in its popularity as advances have been made in synthetic, polymer chemistry, fluorescence, spectroscopy and optical and bio imaging [225]. Quenching-phosphorescence O₂ detection is based on the direct, non-chemical and reversible quenching of phosphorescent signal because of the collision of the phosphorescent dye and O₂ molecules. Quenching of the dye molecules

reduces the phosphorescence lifetime in a concentration-dependant manner [225]. The O₂ sensitive materials are often based on synthetic indicator dyes including macrocyclic complexes of heavy metal ions with lifetimes in the microsecond (μ s) range [226-228]. There are numerous different indicator structures for O₂, the most dominant structures are a small number of dyes, displaying the necessary spectral and O₂ sensing properties, bio-compatibility, availability and cost. Phosphorescent Pt(II) and Pd(II) porphyrins are the most popular, exhibiting lifetimes of approximately 40-100 μ s for the Pt-porphyrins and 400-1000 μ s for the Pd-porphyrins displaying medium to high O₂ quenching. Pt-porphyrins are ideal for O₂ measurements from 0-200 μ M i.e. physiological range, while Pd-porphyrins are more useful only in the lower <50 μ M O₂ range [120]. Some of the more popular dyes include PdTCPP, PtTFPP, PtCP and Ru(dpp)₃²⁺. O₂ indicator dyes that emit in the visible range (550 nm-700 nm) are ideal for biological cell monolayer studies [225]. For studies involving tissues and samples with a more complicated structure indicators which are excitable and emit in the red and near infrared spectrum (600-900 nm) are preferred, such as Pt-benzophorphyrins. PtTFPP would be the favoured dye in high resolution microscopy due to its high photo-stability and brightness. Pt-porphyrins are also preferred over complexes containing Pd as a result of their shorter emission lifetimes allowing for much quicker acquisition times [227]. Dyes based around Ru(II) tend to have problems with low sensitivity to the O₂, lower brightness compared to porphyrins, as well as photo-toxicity issues [229]. They also have much shorter lifetimes ranging from 1-5 μ s [120]. The phosphorescent quenching principle and these phosphorescent dyes measure O₂ in two main formats, either as an O₂ sensing probe or as a solid state O₂ sensor.

Solid state O₂ sensors involve the reliable, accurate measurement of extracellular O₂, or O₂ concentration in specific regions of liquid or air. Solid state sensors are used primarily in O₂ micro-sensors [230], sensor coatings [231] and integrated systems [232]. Specific examples include the fibre optic (Micro) sensors, which can measure O₂ inside tissues using a needle sensor, however they are invasive for cells. The main uses of this type of measurement system is the point measurement of O₂, OCR and scanning of O₂ distribution [233]. There are also spot sensors available for point measurements of dissolved O₂, useful for long term measurements, are non-invasive (for pericellular measurements) and display high optical signals [225]. When developing solid state sensors, the choice of supporting material is important as it affects dye staining and retention, and ensure the dye maintains its photochemical and photo-physical properties. Material must also have favourable optical properties and be O₂ permeable [234]. Different options are available as supporting materials. Organic materials such as beads based on poly(styrene-block-vinylpyrrolidone) have been used to measure O₂, Cl⁻ and Cu²⁺ ions [235]. Organic polymers including polyethylene, poly(methylmethacrylate), poly(vinylchloride) and fluoropolymer are ideal for O₂ imaging as a result of their high permeability and low light absorption [234, 236]. Inorganic polymer sensors produced using the sol-gel method can be produced with a known composition, have 3D structures ensuring the dye entrapment in pores and is easily manipulated by altering pH and temperature in the preparation phase. Sol-gel materials however have lower quenching sensitivity and tend to be fragile [234]. Hybrid sensing films made up of a mix of organic and inorganic polymers [237, 238] ensure resistance to high temperatures, have flexibility, are less fragile and allow high gas permeability [239, 240]. Hybrid O₂ sensors are categorised into two groups, either van der Waals force or covalent bond dependent upon the force

between the organic and inorganic molecules [241]. Hybrid films show higher sensitivity, faster responses and better linearity of the Stern-Volmer plot compared to their uniquely organic or inorganic counterparts [234]. The Stern-Volmer equation predicts a linear relationship between the lifetime/intensity values of the probe and O₂ concentration in a heterogeneous microenvironment. However, in many practical cases the indicator dye has a heterogeneous micro-environment, leading to non-linear Stern-Volmer plots. These effects can be accounted for using the appropriate mathematical or physical model, such as the "two-site" model [226] and the corresponding formula:

$$I_0/I = 1/(f_{\alpha 1}/(1+K_{sv1}[Q])+f_{\alpha 2}/(1+K_{sv2}[Q]))$$

where $f_{\alpha 1}$ and $f_{\alpha 2}$ are the two fractions, and K_{sv1} and K_{sv2} their quenching constants [242].

The second option is the use of soluble probes. These can diffuse across cell membranes into respiring cells and tissues measuring intracellular O₂. Efficient cell loading involves dye modifications through addition of peripheral groups, including charged groups or protein binding domains that mediate probe interaction with the plasma membrane [243]. They can efficiently stain 3D tissue models, providing a high degree of flexibility compared to solid state sensors. However they can have much lower signals, and since they are introduced to biological samples must be rigorously checked for cell toxicity [225]. Other important parameters to be considered with intracellular O₂ probes include uniform staining, concentrations and loading times to achieve the required optical signals [243]. Distinct categories of probe exist, including small molecule probes, based on derivatives of the PdTPCPP [244], Ru(II) [245] and PtCP [246] dyes, with PtTFPP due to its brightness, photostability and price being the

most popular. Small molecule probes are produced through functional modifications of the dye. They are made up of a hydrophilic dye structure making them highly soluble in aqueous media due to the attached carboxylic and sulfonate groups. They have their disadvantages however including self-aggregation, hydrophobic cores, binding non-specifically to proteins and cell surfaces because of their hydrophobic regions and vary in their cell localisation [120]. Another group, micro and nanoparticle (NP) based probes involve the covalent or non-covalent incorporation of a dye inside a polymer shell, shielding from unwanted molecular interactions and interference from the local environment. They are usually larger in size due to their polymeric nature. Nanoparticle probes show greater flexibility with the indicator dyes modified to ensure the addition of functional groups or by pairing dyes for ratiometric and FRET based O₂ measurements [247, 248]. The uptake of NPs into cells is believed to be by electrostatic interactions with the plasma membrane (negatively charged) and specific transport mechanisms such as clathrin mediated endocytosis. Cell staining tends to be slower (12-48 h) than for small molecule probes and may not be possible for some cell types [243].

Useful examples of NPs include a probe referred to as NanO₂ involving nanoparticle formation by combining the cationic polymer Eudragit RL-100, (a polymer originally developed for biocompatible coatings and drug delivery systems) [249] and the hydrophobic phosphorescent dye Pt(II)-tetrakis(pentafluorophenyl)porphyrin (PtTFPP) [250]. The positive charge on the RL-100 increased the ability of the probe to interact with the cell membrane, increasing penetration ability into cells, finally localising to the endosomes and lysosomes. There are however issues with neural cell staining using these RL-100 based probes. It displays sensitivity to O₂ in the physiological range [251] with no issues with probe aggregation. It formed a smooth

spherical shape with a size of approximately 40nm, capable of efficient staining monolayer cells, with no significant cell leakage or toxicity effects. Efficient staining was also seen in other cell lines including HeLa, HepG2 and PC12 cell. Due to its small size and the high brightness it possesses the probe need only be added at low concentrations [250]. Over all it was observed that these probes based on PtTFPP in the Eudragit RL-100 polymer are easy to produce, have self-loading ability, high and stable phosphorescent signals. They allow for the accurate measurement of cellular O₂ in live cells, and by extension acts as an indicator of cellular responses to drugs, metabolic processes, cellular function and viability [250].

Further developments include the formation of anionic cell permeable phosphorescent nanoparticles. The probes are negatively charged poly(methyl methacrylate-co-methacrylic acid)-based nanoparticles impregnated with the phosphorescent dye PtTFPP dye, coupled with a reference dye PFO, known as PA2. Entering the cell via endocytosis it has been shown to effectively stain primary neurons, astrocytes, PC12 cells, multi cellular aggregates and the more complex rat brain slices [252]. These probes were produced via nanoprecipitation technique [251]. They showed similar spectral characteristics to the NanO₂ probe, with lifetimes of 31-70 μs in the 0-200 μM range of O₂ but improved staining in different neuronal cell lines. However, it showed less efficient staining of fibroblasts. They displayed good photo-stability, lower aggregation and non-specific adsorption [253]. Like cationic probes they localised to the endosomes and lysosomes, but also showed improved distribution across 3D models including tissue explants. Although these probes were useful in numerous cell based studies they had negative issues regarding low staining depths for imaging [243].

Conjugated polymer nanoparticles are now the next phase in improving results obtained using high resolution O₂ imaging, comprised of a conjugated polymer matrix, a light harvesting antenna, and a reference all copolymerised with the indicator O₂ sensitive dye. They are also grafted with charged groups capable of ensuring cell penetration and stability, allowing for the measurement of both phosphorescent lifetime and ratiometric intensity in the visible or near infra-red spectral ranges. These probes have improved performance, depth penetration, cell staining and brightness when compared to its predecessors [136]. The polymers are comprised of a polyfluorene/ poly(fluorene-alt-benzothiadiazole) backbone antenna, both a red as well as an infrared emitting reporter based on a Pt(II)-porphyrin and finally various charged groups. Variation in the charged groups defines whether the probe is, negative, positive or zwitterionic increasing their ability to efficiently stain more 2D and 3D models. The zwitterionic probes in particular display more, efficient intracellular staining and deeper penetration within samples [136]. As the calibration curves for the fluorescent molecular probes become more reliable in cells and tissues fluorescence lifetime imaging will become more prevalent and more widely used for the investigation of diverse cellular and pathological processes in the future.

1.5 Importance of O₂ imaging in cells and tissues

1.5.1 Effect of hypoxia on cells and tissues physiology

There is no universal O₂ concentration that can be labelled hypoxia, as tissues and specific cells experience differences in O₂. Thus, hypoxia, can be defined as a reduction in O₂ tension below that normally experienced by a tissue or a cell. The only cell type that experiences close to ambient O₂ is respiratory epithelia, while the O₂

levels in other cell types depends upon distance from the medium or capillary and the O₂ tension within the capillary where it connects to the cell. Cell responses depend upon O₂ concentrations and thus experiments carried out using *in vitro* cells should be carried out at physiologically relevant O₂ tensions [254]. This too may be left up to individual interpretation, for example colon tissues and tumours *in vivo* have a highly heterogeneous O₂ concentration ranging anywhere from 0-5 % [255, 256].

Many O₂ probes can be multiplexed with other biomarkers, measuring pH, temperature and Ca²⁺. The ability to ensure O₂ homeostasis is pivotal to the survival of both vertebrates and invertebrates. Cells in the human body can sense changes in O₂ availability and can adapt through cellular responses to such stimuli. Adaption usually involves alterations in gene expression in response to hypoxia, including stabilising of HIF-1 α , which in turn activates a great many genes including VEGF transcription a regulator of angiogenesis and endothelial cell migration to hypoxic areas, as well as GLUT1 and GLUT3 responsible for glucose uptake [257] and EPO [258] which is involved in controlling red blood cell production, to name a few. The hypoxia inducible factor (HIF) family members are transcription factors that mediate the intracellular hypoxic response, inducing gene transcription of genes involved in functions like glycolysis, cell proliferation and iron metabolism. HIF is a heterodimer, comprised of an O₂-regulated α subunit, further divided into HIF-1 α , HIF-2 α and HIF-3 α isoforms and a constitutively expressed β subunit. Dimerization between both of them is necessary for DNA binding [259]. HIF-3 α lacks the C-terminal activation domain needed for co-activator binding, thus it is unable to recruit co-transcriptional regulators and basal transcription machinery to gene targets [260]. Under normoxic conditions HIF-1 α binds Von Hippel-Lindau (VHL) protein, which recruits a ubiquitin ligase that ensures HIF-1 α is degraded in the proteasome. It is the role of prolyl

hydroxylases (PHDs), specifically PHD2 that mediate HIF-1 α hydroxylation, via VHL binding to the HIF-1 α proline residue using O₂ as a substrate. As a result its binding is inhibited in hypoxic conditions [261]. In hypoxia HIF-1 α and HIF-2 α hydroxylation is decreased, resulting in HIF- α stabilisation/accumulation and increasing transcriptional activity of genes involved in cell survival, proliferation and energy metabolism as well as apoptosis and autophagy. In acute hypoxia, HIF-1 α is associated with cell death, while in solid tumours it aids cell survival and proliferation. The switch from pro survival to pro-apoptotic pathways is not well understood but may be because of binding to proteins such as p53. There is also a feedback loop and induces the transcription of PHDs, ensuring that after prolonged hypoxia HIF returns to low undetectable levels [262]. These PHDs particularly PHD2 may have a major role in controlling HIF dynamics preventing cell death by increased HIF-1 α levels. It was noted that in HeLa cells lacking PHD2 expression, p53 was shown to sustain high levels, suggesting apoptosis was occurring [262].

There are also several HIF-independent pathways that are equally as important for a cells response to hypoxia, via some major signalling pathways. The mammalian target of rapamycin (mTOR) complex 1 pathway, which phosphorylates S6 kinase and 4E-BP is inhibited. This leads to the inhibition of ribosomal biogenesis and cap-dependent translation and by extension protein translation, saving energy under sever hypoxia. When cells are exposed to ER stress and unfolded proteins accumulate in the ER, cells activate the unfolded protein response (UPR) to maintain protein quality or induce cell death. UPR is activated in hypoxia by PERK, IREL and ATF6. PERK inhibits translation of proteins via eIF2 phosphorylation, while IRE1 increases apoptosis. The nuclear factor-kappa B (NF- κ B) pathway, is a key transcription factor in immune response but also plays a major role in hypoxia response. The NF- κ B pathway is

activated under hypoxia, inducing HIF-1 α mRNA, while also being induced by HIF-1 α aiding cell survival. When activated in tumours it aids in tumour angiogenesis. The downregulation of PHD2 increases NF- κ B activity and upregulates *IL-8* and *angiogenin* gene expression [263].

Hypoxia within tumours and disease tissue results from inadequate perfusion and reduced O₂ transport [264]. Hypoxia in tumours can cause resistance to radiotherapy, with a decrease in sensitivity noted when O₂ levels drop below 2.6 %. Furthermore it may lead to malignant progression, as tumour cells that can withstand hypoxic conditions increase the number of clonogens that increase tumour size and produce metastatic cells [265]. Cancers also have greater rates of cell proliferation and a lack of vasculature leading to areas of hypoxia. Increased HIF-1 α and HIF-2 α levels as a result of stabilisation are observed in biopsies and boost mortality rates in bladder, brain, breast and colon cancers while a loss of HIF-1 α expression can decrease tumour growth [266]. HIFs activate gene transcription involved in cell immortalization, epithelial-mesenchymal transition [261], vascularisation [267], pH regulation [268], invasion and metastasis [269], and radiation resistance [270]. As a result of hypoxic microenvironments in diseased tissue an increase in HIF-1 α has been observed, indicating it may be a possible therapeutic target [271]. Diseases involving the lung can often lead to hypoxia and by extension result in pulmonary hypertension. This exposure to hypoxia can lead to increased proliferation of smooth muscle in the pulmonary artery, with HIF-1 α playing a pivotal role in the development of this hypertension [272]. Hypoxia caused by sleep apnea leading to lower O₂ in the blood affects the pharyngeal soft tissue. Alternating between hypoxic and re-oxygenated states within the tissue causes increased ROS levels in the brain. Hypertension is caused as a result of increased plasma catecholamine levels [273]. Moreover, hypoxia

leads to impairment of mitochondrial respiration, inhibition the respiratory chain and increased proton leaking. To adapt to hypoxia cells and tissues must increase the efficiency of energy production pathways, primarily by increasing anaerobic glycolysis activity as well as decreasing energy-consumption processes [274]. This switch from oxidative metabolism to anaerobic glycolysis, increasing glucose uptake and utilisation is a phenomenon known as “the Warburg effect”. Only in anaerobic conditions will normal cells produce large amounts of lactate, however cancer cells produce large amounts of lactate regardless of oxygen concentration, due to its desire to produce energy via glycolysis, known as “aerobic glycolysis”. This form of energy production is sufficient for cell proliferation, however it is an inefficient method for adenosine 5'-triphosphate (ATP) generation, thus the reason for the switch occurring in cancer cells is unclear [275]. This increase in glucose uptake is seen in adipocytes and can lead to increased lactate production, hypoxia induced insulin resistance in fat cells and thus development of fibrosis in adipose tissue. Hypoxia is therefore linked to defects in the appropriate function, obesity and obesity related diseases [276].

This ability of cells to successfully adapt to hypoxia was observed in another unrelated study using glioblastoma (aggressive brain tumour) cells. Results showed that in O_2 levels of 1-8% there was no effect on cell cycle. Cell cycle arrest and minor cell death were only seen when cells were exposed to 0.1 % O_2 [277]. The large number of disease states associated with hypoxia and its links to malignancy, invasiveness and resistance to chemotherapeutic treatment make O_2 probes and accurate measuring of intracellular O_2 in 3D models of utmost importance.

1.6 Summary

While advancements have been made in 3D it is important to remember their relevance is only important should they be capable of accurately mimicking *in vivo* conditions. This is only possible by optimising the conditions and monitoring the gradients in molecules such as O₂, Ca²⁺ and NADPH as well as monitoring gradients in pH and temperature. By building up our knowledge of these conditions we can have a greater understanding of what is required and what must be altered to make these models more physiologically relevant. This work in model development will be aided through better knowledge of natural tissues using fluorescent probes and markers, which in turn can then be used in further studies. The complexity of both the models and the probes are always changing, always improving, ensuring great leaps in cellular pathway and gene expression studies as well as drug evaluation studies.

1.7 Thesis aims

The overall aim of this thesis was to develop new sensors, probes and protocols for oxygen imaging in 3D cell cultures. Specifically, we wished to develop a new improved O₂ sensitive solid state sensor, capable of non-invasively measuring pericellular and extracellular O₂. Furthermore, we wanted to evaluate new O₂ and Temperature based water soluble intracellular nanoparticle probes, all of which are covered in chapter 3. In chapter 4 we look at some of the possible applications of our new sensors and probes. We optimised the 3D spheroid model and incorporating the resulting *in vitro* tissues into our research. Interesting applications included our metabolic study, imaging simultaneously O₂ and T dynamics in 3D spheroids, drug toxicity studied using the chemotherapeutic drug tirapazamine and a mechanistic study investigating the role of SPCA2, the Ca²⁺/Mn²⁺ pump in hypoxia, in both monolayer

and 3D cultures. In summary, we wished to highlight the importance of measuring both O₂ and temperature in all areas of research, emphasising the effects these metabolic parameters have on cell viability, gene expression and drug efficacy.

Chapter 2. Materials and Methods

2.1 Materials

PtTFPP dye (Cat # PtT975) was from Frontier Scientific (Inochem Ltd, Lancashire, UK). ProLong Gold anti-fade reagent, Tethramethylrhodamine, methyl ester (TMRM), CellEvent Caspase-3/7 substrate, Cholera Toxin sub-unit B, MitoTracker Green and LysoTracker Red were from Invitrogen (Biosciences, Dublin Ireland). CellTox Green assay kit and CellTiter-Glo kit were from Promega (MyBio, Ireland). ROSstar 550 dye was from Li-Cor (USA). MitoImage-NanO₂ phosphorescent O₂ probe [278] and pH-Xtra™ [279] were from Luxcel Biosciences (Cork, Ireland). SII-0.2⁺ copolymer nanoparticles were prepared as described before [136]. Perylene bisimide-based pH probe NSP was prepared as described before [280]. Bis-Benzimide Hoechst 33342 and Calcein Green AM probe were from Sigma-Aldrich (Dublin, Ireland). Mouse monoclonal anti-BrdU 'BU-1' antibody (Cat # 05-633) and mouse monoclonal anti-SERCA2 antibody (Cat # MAB2636) were from Millipore (Cork, Ireland). Mouse monoclonal anti-HIF1 α antibody (Cat # MAB1536) was from R&D systems (Oxfordshire, UK). Rabbit polyclonal anti-Tyrosine Hydroxylase antibody (Cat # ab41528) was from Abcam (Cambridge UK). Mouse monoclonal anti- α -Tubulin antibody (Cat # T5168), HRP (horseradish peroxidase)-conjugated secondary mouse anti-rabbit (Cat # A1949) and goat anti-mouse (Cat # A9917) were from Sigma-Aldrich (Dublin, Ireland). Alexa Fluor-488 goat anti-rabbit (Cat # A11034), Alexa Fluor-488 goat anti-mouse (Cat # A10680) and Alexa Fluor-594 goat anti-mouse (Cat # A11032) conjugated secondary antibodies were from Invitrogen (Biosciences, Dublin Ireland). Epidermal growth factor (EGF) and fibroblast growth factor (FGF) were from Promega (MyBio, Ireland). B27 serum-free supplement was from

Invitrogen (Biosciences, Dublin Ireland). Cantharidin, FCCP, oligomycin, Tirapazamine, MnCl₂, BrdU, oligonucleotides and all the other chemicals (HPLC or spectrophotometric grade) were from Sigma-Aldrich (Dublin, Ireland). Polystyrene scaffold membranes Alvetex™ (12-well inserts) and Lipidure™ plates were from Amsbio (UK). Perfecta 3D Hanging drop plates were from 3D Biomatrix (UK). Ibidi μ-slide 8/12-well chambers were from Ibidi (Martinsried, Germany). TransIt-X2 reagent was from Mirus (MyBio, Dublin, Ireland). PCR master mix, Improm-II reverse transcriptase, ribonuclease inhibitor and ReliaPrep total RNA extraction kit were from Promega (MyBio, Ireland). qPCR reagent and Nucleo-spin II Total RNA extraction kit was from Macherey-Nagel (Thermo Fisher scientific, Dublin, Ireland). ECL Prime chemiluminescent substrate was from GE Healthcare (Cork, Ireland). The sterile plasticware (cell culture grade) was from Sarstedt (Wexford, Ireland). GPP130-GFP plasmid DNA was kindly provided by from Prof. A. Linstedt and Dr. S. Mukhopadhyay (Carnegie Mellon University, Pittsburgh, USA). Plasmid DNAs encoding hSPCA2 and hSERCA2b and anti-SPCA2 polyclonal rabbit antibody were provided by Prof. F. Wuytack and S. Smaardijk (Laboratory of Cellular transport systems, KU Leuven, Belgium). Plasmid DNAs for transfection were purified from *E.coli* using Genopure Plasmid Midi Kit (Roche). Rabbit polyclonal pan-SPCA antibody [281] was provided by Dr. N. Pestov (Shemyakin-Ovchinnikov Institute of Bioorganic Chemistry, Russia). Mouse colon RNA samples isolated from normal and hypoxia-preconditioned mice [282] were provided by Dr. I. Okkelman, Dr. A. Zhdanov and Prof. K. O'Halloran (University College Cork, Ireland).

2.2 Cell culture

Human colon carcinoma HCT116 cells and rat pheochromocytoma PC12 were obtained from ATCC (Manassas, VA, USA). Knock out HCT116 (*SCO2*^{-/-}) cells were provided by Prof. P. M. Hwang (NIH, Bethesda, MD, USA). Human colorectal carcinoma HCT116 cells *WT* (wild type) and *SCO2*^{-/-} were grown in McCoy 5A medium supplemented with (10 % v/v) fetal bovine serum (FBS, heat-inactivated), 10 mM HEPES, pH 7.2, 2 mM Glutamine and penicillin-streptomycin (1 % v/v) in cell⁺ flasks (cell plus, yellow capped, adhesion flasks). Prior to seeding in scaffolds PC12 cells were grown in RPMI-1640 media with (10 % v/v) horse serum (HS), (5 % v/v) fetal bovine serum (FBS, heat-inactivated), 10 mM HEPES and penicillin-streptomycin (1 % v/v).

For O₂ and T probe calibrations and immuno-staining cells were seeded on collagen IV: poly-D-lysine (0.07 mg/ml: 0.03 mg/ml) pre-coated 35 mm glass bottom dishes (MatTek) or multi-well micro-chambers (Ibidi). For analysis of effects on cell viability, HCT116 cells were seeded on 96-well flat bottom micro-plates, pre-coated with mixture of 0.1 mg/ml collagen IV and grown until forming a monolayer.

Staining with LysoTracker Red (100 nM), MitoTracker Green (50 nM), Calcein Green AM (1 μM), CellTox Green (0.1 % v/v), Cholera toxin (2.5 ng/ml), Hoechst 33342 (1 μM) and TMRM (20 nM) was performed by incubating with cells/spheroids for 30 min and one wash step. Prior to imaging, cells were equilibrated in Phenol Red-free DMEM medium supplemented with 10 mM glucose, 1 mM pyruvate, 2 mM glutamine, 10 mM HEPES, pH 7.2. Spheroids were allowed attach for (3-8 h) on collagen IV: poly-D-lysine (7: 3 ratio) pre-coated glassware.

2.3 Preparation of O₂-sensitive 3D scaffolds

PtTFPP dye was dissolved at 0.025-0.05 mg/ml in acetone: water (7: 3) mixture at room temperature, and 1 ml aliquots of this solution were added to the Alvetex™ scaffold membranes placed individually in wells of a standard 24-well polystyrene plate. The soaked membranes were incubated for 1 h at 60 °C, then washed sequentially (each time 5 min at 60 °C) with 1 ml of acetone: water (3.5:6.5), acetone: water (1.5: 8.5) and lastly with sterile water. The stained "O₂-scaffolds" were dried under sterile laminar air flow and stored at room temperature protected from light and contamination.

2.4 Growth and treatment of cells in the O₂ scaffolds

Prior to cell seeding, dried O₂ scaffolds were pre-soaked in small amount of 70% ethanol and then rinsed three times with 1 ml of sterile PBS. After seeding, cells were allowed grow inside the scaffold for 1-5 days.

Rat pheochromocytoma PC12 cells were cultured in Phenol Red free DMEM (Sigma D5030) supplemented with 10 mM glucose, 1 mM pyruvate, 2 mM l-glutamine, 10 mM HEPES, (1 % v/v) Penicillin-Streptomycin, (2 % v/v) B27, 20 ng/ml EGF, 10 ng/ml FGF and 100 ng/ml NGF to produce suspension cells and multi-cellular aggregates following 3 days culturing [283] and then seeded at a density of 60-100 aggregates per O₂ scaffold. Cell viability was assessed by analysing membrane integrity using the CellTox Green assay (0.1 % v/v, 30 min) and number of viable cells stained with TMRM (20 nM, 30 min) in comparison with control unstained scaffold.

In preparation for drug treatment O₂ scaffolds were seeded with 60-100 PC12 aggregates per scaffold in serum free media (SFM) and grown for 3 days. 1 mM TPZ

(or 1 % v/v, DMSO in controls) was added simultaneously with (0.1 % v/v) CellTox green and TMRM (20 nM) to the membranes and incubated for 40 minutes. The membranes were washed once with 1 ml of Phenol Red free DMEM media containing TMRM. The numbers of dead cells and corresponding phosphorescence lifetimes were then determined and compared to the control samples.

2.5 Measurement of PtTFPP dye leaching using micro-plate reader

Dye leaching experiments were carried out on a high-sensitivity time-resolved fluorescence (TR-F) reader Victor2 (PerkinElmer). Supernatants from samples with O₂ scaffolds were taken periodically and measured 5 times over 10 min in the wells of 96well micro-plate under the following settings: mode - time-resolved fluorescence; filters - D340 excitation and D642 emission, delay time – 30 µs, gate time – 100 µs, cycle time – 1000 µs. Mean signal values were then calculated.

2.6 DNA transfection and hypoxia treatment of adherent cell culture

HCT116 cells [284] were washed with PBS, trypsinised and split 1:10 every 2-3 days when not being seeded for experimentation [285]. Typically, cells were grown in McCoy 5A medium supplemented with (10 % v/v) fetal bovine serum (FBS, heat-inactivated), 10 mM HEPES, pH 7.2, 2 mM Glutamine, penicillin-streptomycin (1% v/v) in cell⁺ (cell plus, yellow capped, adhesion flasks) flasks. Control and hypoxia (continuously exposed at 3% O₂, in an airtight incubator with attached heating and O₂ controls for 7 days, including cell passaging and seeding) – treated cells were normally harvested at 50-70% of confluence unless indicated otherwise. DNA transfection of adherent cells was performed using TransIt-X2 reagent (Mirus), as per manufacturer's

instructions. Briefly, cells seeded at 70-75% confluence were transfected with GPP130-GFP, hSPCA2 and hSERCA2b-encoding plasmid DNAs in Opti-MEM I medium for 24-36 h and then analysed. For the treatment with MnCl₂, cells were first transfected for 18 h and then exposed to 0.5 mM MnCl₂ for 24 h. For immunofluorescence cells were pre-stained with BrdU (100 μM, 30 min).

2.7 RNA extraction and PCR analysis

2-4*10⁶ cells were washed with PBS and total RNA was immediately isolated using Nucleo-spin II RNA extraction kit (Macherey-Nagel), per manufacturer's instructions. For spheroid cultures, RNA was extracted from pooled spheroids (72 for 1,000 or 24 for 3,000 initially seeded cells) using the 'ReliaPrep' extraction kit (Promega, MyBio, Ireland) accordingly to manufacturer's instructions. 1-2 μg of total RNA annealed with 500 ng oligo-(dT)₁₅ (70 °C, 5 min, then 4 °C, 5 min), reverse transcribed using ImProm-II Reverse transcriptase (42 °C, 2 h), heat-inactivated (70 °C, 15 min) and stored at -18 °C. cDNA was used for semi-quantitative PCR analysis (25-35 cycles) or real-time PCR using qPCR reagent (Maxima SYBR green, Fisher Scientific), and the AB7300 Real-Time PCR machine, analysed using the 7300 system SDS software from Applied Bio-systems (Life technologies) (45 cycles). The sequences of oligonucleotides are presented in (Tab. 2.7).

Table 2.7 Sequences of oligonucleotide primers used in the study.

Name/ Gene ID, Acc. Number	Sequence (forward, reverse)
B-actin (Human), ACTB	F 5' CCACCATGTACCCTGGCATT R 5' CGGACTCGTCATACTCCTGC
B-actin (Mouse), ACTB	F 5' TGGCTCCTAGCACCATGAAG R 5' ACGCAGCTCAGTAACAGTCC
MIST1 (human), BHLHA15	F 5' CTCACGCTGGCCAAGAATA R 5' GTGGATCTGCGTGGAGTACC
PMCA1 (Human), ATP2B1, NM_001001323	F 5' GGATACTCGCTTCCCTGG R 5' AGGAGCATGCAAAGGAGCAT
PMCA2 (Human), ATP2B2, NM_001001331	F 5' GGCACAAATATCAACACGGC R 5' AGGGTATGCTTGTCCGTTGG
PMCA3 (human), ATP2B3, NM_001001344	F 5' CCGTGGTCCAGTCCTACCTA R 5' TTCAGGTCCAAGACGAAGCC
PMCA4 (human), ATP2B4, NM_001001396	F: 5' CCTGTGGCTGAGATTGTGGT R: 5' GGCCAGAACCTTCCATGACA
SERCA2ab (Human), ATP2A2, NM_170665	F 5' GGAGAGAACACCCCTTCAGC R 5' GACCTTCAGGAATGGCTGCT
SERCA3a (Human), ATP2A3, NM_005173	F 5' CTGGATGAACCCCTGGCTG R 5' ATGTGGTTCCGGGACAGGTA
SPCA1 (Human), ATP2C1, NM_001199179	F 5' AGATTCCAGCTGAGCACGAG R 5' CTTTCCAGTTGCGAGGAGGT
SPCA2 (Human), ATP2C2, AY791884	F 5' ACTTACACACTGGGCTGTCTG R 5' CTGACGGCGTCCTCATACTC
SPCA2 (Mouse), ATP2C2, NM_026922	F 5' CCAGAGTGCAACTGCCTGAG R 5' CCAGTGGGCTGTCTGTTTTG

2.8 Production and analysis of spheroids

Three different methods of spheroid production were used: (1) in "free floating" (FF) method cells were seeded at concentration 5×10^6 cells in 5 ml of Serum-free medium, SFM (Phenol Red-free DMEM, 10 mM Glucose, 1 mM sodium pyruvate, 2 mM Glutamine, 10 mM HEPES-Na, pH 7.2, (1% v/v) Penicillin-Streptomycin, 1x B27, 20 ng/ml EGF and 10 ng/ml FGF in 25 cm² low adhesion flask [286]. Spheroids were formed after 3 days of culture. (2) 'Hanging drop' method used seeding of cells at various concentrations in 40 μ l of McCoys 5A medium supplemented with (10% v/v) fetal bovine serum (FBS, heat-inactivated), 10 mM HEPES, 2 mM Glutamine, (1 % v/v) penicillin-streptomycin per well, followed by addition of PBS to the 96-well plate to prevent the excessive evaporation [287]. Lipidure® method used seeding of various

concentrations of cells in 200 μ l growth medium and 3-day incubation in 96-well round-bottom hydrophobic microplates (Lipidure-coat, Amsbio, UK), spheroids of approx. 400-650 μ m size were formed after the 3 days (3).

Spheroid staining with SII-0.2⁺ (5 μ g/ml), NanO2 (5 μ g/ml), pH (5 μ g/ml), ROSstar (5 μ M) and CellTox Green (0.2 % v/v) was performed by addition of the probe to growth media at the start of spheroid formation and incubation for 3 days i.e. "continuous staining" procedure. Staining with T probe (1 μ g/ml) was performed by adding to media 17h prior to imaging to already formed spheroids i.e. post formation staining procedure. Staining with TMRM (20 nM, 30 min) was achieved with pre-formed spheroids. To label proliferating cells, BrdU (200 μ M) was added to pre-formed spheroids 16-18 h before the fixation. For microscopy, spheroids were re-seeded and allowed to attach (3-8 h) on MatTek 35 mm glass-bottom dishes (MatTek) pre-coated with mixture of Collagen IV and poly-D-lysine (7:3 ratio respectively) [278]. Live spheroids were routinely, washed twice prior to imaging, which was then performed in phenol red-free DMEM supplemented with 10 mM glucose, 1 mM sodium pyruvate, 2 mM L-glutamine and 10 mM HEPES-Na, pH 7.2 at 37 °C and ambient O₂ (21 %).

2.9 Protein extraction and western blotting

2-4*10⁶ cells were washed with PBS and lysed in RIPA buffer (25 mM Tris-HCl pH 7.6, 150 mM NaCl, 1% v/v NP-40, 1 % sodium deoxycholate, 0.1 % w/v SDS) supplemented with PhosSTOP phosphatase inhibitors (Roche 4906837001) and protease inhibitor cocktail (Sigma P2714) for 10-15 min on ice with gentle rocking. Extracts were cleared by centrifugation (15,000 g, 15 min, 4 °C) and total protein was

quantified by the BCA protein assay kit (Pierce). Samples normalised for total protein were mixed with 5X Sample Laemmli Buffer (4 % w/v SDS, 20 % v/v glycerol, 10 % v/v 2-mercaptoethanol, 0.004 % w/v bromphenol blue and 0.125 M Tris HCl, pH 6.8), incubated for 10 min at room temperature (no boiling, preventing any protein degradation). Proteins were separated by 8 % polyacrylamide gel electrophoresis (GenScript, NJ) in 1X running buffer (Tris base 3.03g, glycine 24g, SDS 1g, dissolved in 1000ml deionised water). The gel was transferred (slide the gel manually) onto a 0.2 μ m ImmobilonTM-P PVDF membrane (Sigma). This was placed into a transfer chamber with the proteins passing from the gel into the PVDF membrane as the transfer buffer (Tris base 3.03g, glycine 14.4g, methanol 200ml, dissolved in 800ml deionised water) runs from the cathode (-) towards the anode (+). The membrane was then probed with antibodies. Incubations with antibodies were performed in (5% w/v) fat-free milk/TBST overnight at 4 °C (primary) and 1-2 h room temperature (secondary). Immunoblots were analysed using HRP-conjugated secondary antibodies (Sigma) and AmershamTM ECLTM Prime reagents with the LAS-3000 Imager (Fujifilm, Japan) and Image Reader LAS-3000 2.2 software.

2.10 ATP and ECAR measurements

Total cellular ATP was measured [288], using CellTiter-Glo reagent (Promega). Briefly, spheroids were allowed attach to the collagen-coated 96-well plates in Phenol Red-free DMEM for 3 h, at concentrations approx. 1 spheroid of 6,000 cells/ per well (Lipidure or "hanging drop" methods), approx. 12-18 spheroids/ per well ("free floating" method) or 30,000 cells per well for mono-layered cells. After attachment, equal amount of CellTiter-Glo reagent was added, lysates were mixed via intensive shaking and transferred to white 96-well plates (Greiner Bio One). The luminescence

was analysed on time-resolved fluorescence plate reader Victor2 (Perkin Elmer). (ECAR) was measured [289] with the pH-Xtra™ probe (Luxcel Biosciences). Briefly, cells grown on microplates were treated with various concentrations of T (0-2 µg/ml) and SII-0.2⁺ (0-20 µg/ml) for 16 h, washed and measured using Victor2 time-resolved fluorescence plate reader (Perkin Elmer). ECAR values were normalized by total protein content, measured using BCA method.

2.11 Immunofluorescence

For immunofluorescence, cells grown in O₂ scaffolds were fixed in paraformaldehyde (4 % w/v, 10 min, RT). Fixed cells in O₂ scaffolds were permeabilised with 0.25% v/v Triton X-100, then blocked with 5% v/v, bovine serum in TBST and immunostained with anti-tyrosine hydroxylase antibody (Abcam, ab112) in TBST (16 h, 4 °C). Washed with TBST (1 h, 5 times), incubated with appropriate Alexa Fluor-conjugated secondary antibodies 1:1000 dilution (2 h, RT), washed with TBST (1 h, 5 times). Spheroids were fixed in paraformaldehyde solution (4 % w/v, 40 min, RT), washed with PBS (0.5 h, 5 times), blocked in 10% fetal bovine serum (FBS) supplemented with 0.4 % v/v Triton X100 in PBS (2 h, room temperature), incubated with primary antibodies in 2.5 % v/v HS, 0.4 % v/v Triton X100 in PBS (48 h, 4 °C), washed with TBST (1 h, 5 times), incubated with appropriate Alexa Fluor-conjugated secondary antibodies 1:1000 dilution (18 h, 4 °C), washed with TBST (1 h, 5 times), counter-stained with DAPI (14 µM, 1 h). Samples were then mounted between coverslips in ProLong Gold antifade medium (Invitrogen) and subjected to fluorescence microscopy analysis.

Immunostaining with monolayer cells were performed as with the above O₂ scaffolds [73] using cells grown on 12 well μ -slide (Ibidi) and probed with rabbit antibodies against cleaved Caspase-3 (Cell Signalling), rabbit anti-SPCA2 (XIB, provided by Prof. F. Wuytack), mouse anti-SERCA2 (Millipore) or BU-1 (Millipore) antibodies, followed up by staining with Alexa Fluor 488 or 594-labeled secondary antibodies (Invitrogen) and staining of nuclei by DAPI (300 nM, 5 min). Samples were analysed by widefield fluorescence microscopy.

2.12 Widefield PLIM microscopy

The live cells, transfected with GPP130-GFP plasmid DNA [290] and counter-stained with LysoTracker Red (0.1 μ M, 30 min), as well as fixed and immunostained cells, O₂ calibrations and photobleaching experiments were performed on a wide-field inverted microscope Axiovert 200 (Carl Zeiss) equipped with an oil-immersion objective 40 \times /1.3 EC Plan Neofluar and 100 \times /1.4 Plan Apochromat, 470 and 590 nm LED excitation module, time-gated CCD camera and emission filters DAPI (Semrock 5060B-ZHE), FITC (472/30 nm ex., 535/55 nm em.) and TXRed (Semrock 4040B-ZHE) 390, 470 and 590 nm LED excitation module, ImSpector software (LaVision BioTec, Germany) and integrated CO₂/O₂ climate control chamber (PeCon) [278]. In PLIM mode the parameters were: snapshot mode, 50 ms exposure, devices delay T. For the intensity imaging the parameters were: exposure time - 2 ms, devices – none, DC mode – ON, no binning. Photobleaching experiments were performed in DC mode with the following settings: exposure time - 2 ms, devices - time-time, numbers of steps - 12, wait time - 10 s.

2.13 Confocal FLIM-PLIM microscopy

Analysis of cell staining, 3D O₂ scaffolds, spheroid culture, T calibrations and multi-parametric measurements were performed on an TCSPC one-photon laser-scanning upright Axio Examiner Z1 microscope (Carl Zeiss), equipped with 20×/1.0 W-Plan-Apochromat and 63×/1.0 W-Apochromat objectives, temperature control (external incubator and heated stage, 25 °C-42 °C) with motorized Z-axis control, DCS-120 time-correlated single photon counting confocal scanner (Becker & Hickl GmbH), R10467U-40 and R10467U-50 photon counting detectors (Hamamatsu Photonics K.K.) and dedicated TCSPC hardware (Becker & Hickl GmbH)[278, 289]. SI-0.2⁺ nanoparticles were excited using picosecond pulsed diode 405 nm laser BDL-SMC (Becker and Hickl GmbH) with emission collected at 635-675 nm (O₂ dye, PLIM mode). SII-0.2⁺ nanoparticles were excited using supercontinuum tunable laser SC400-4 (Fianium, UK) at 620 nm with emission collected at 750-810 nm (O₂ dye, PLIM mode). The fluorescent and phosphorescent probes were excited using tunable picosecond supercontinuum laser SC400-4 (Fianium, UK) at 488 nm (CellTox Green, Calcein Green, Alexa Fluor 488Cholera toxin, MitoTracker Green), 540 nm (T probe, LysoTracker Red, TMRM) and 620 nm (SII-0.2⁺). The following emission filters were used: 512-536 nm (for 488 nm), 565-605 nm (for 540 nm) and 760-810 nm (for 620 nm). NanO₂ and Hoechst 33342 were excited using BDL-SMC picosecond 405 nm laser (Becker & Hickl GmbH) with emission collected at 635-675 nm (NanO₂) and 438-458 nm (Hoechst 33342). Fluorescence lifetimes for T probe were analyzed using SPCM64 and SPCImage software (Becker & Hickl GmbH) using mono-exponential decay function (T₁=50, T₂=150, binning factor=4, threshold=10, shift=0, offset=0). For T-dependent calibration, cells were pre-incubated at different temperatures for 10 min, before measurements of fluorescence lifetimes. The following calibration was

produced: $T (^{\circ}\text{C}) = 105.6 - 0.0277 * \tau$, $r^2 = 0.99$ where τ is in ps. Phosphorescence lifetimes of O_2 probe (SII-0.2⁺) were fitted using mono-exponential decay function (T1=120, T2=225-240, binning factor=3, threshold=10, shift=0, offset=0). Processed decay times were exported and further combined in Excel, Origin 6.0, Fiji and Adobe Illustrator software. The phosphorescence of O_2 scaffolds was excited at 534 nm and collected with 635-675 nm bandpass filter, and lifetimes were calculated by mono-exponential fitting of decay curves in SPCImage software (Becker & Hickl GmbH) using the following settings: Shift: 0-10, Binning: 1-3, T1: 120-140, T2: 230-250. Drug treatments (FCCP, AntA, Tirapazamine) were performed using addition of 10x concentrated stocks in Phenol Red free DMEM at 1/10 of total volume with live samples. For scaffold 3D reconstruction samples were fixed with PFA, immunostained (see 2.11) and scanned in Z direction (20-25 optical sections, 2 μm thickness, 40-50 μm total depth). The fluorescent probes were excited with tunable picosecond supercontinuum laser SC400-4 (Fianium, UK) or BDL-SMC 405 nm pulsed diode laser (Becker & Hickl GmbH) for NanO₂. O_2 imaging with NanO₂ probe was performed using long pass excitation (>435 nm for laser 405 nm) and bandpass emission (655/40 nm for PtTFPP). Lifetimes were translated to O_2 values using the following calibration function: $[\text{O}_2, \mu\text{M}] = 9274.667 * \exp(-\tau/7.27143)$, where τ is in μs [278]. Alexa Fluor 488, CellEvent Caspase 3/7 and CellTox Green dyes were excited at 488 nm with emission collected at 512–536 nm. TMRM was imaged using 540 nm excitation, 565-605 nm emission; Alexa Fluor 594 was excited at 594 nm, with emission collected at 635-675 nm. Transmission light images were collected with a D5100 digital SLR camera (Nikon) attached to the microscope.

2.14 Data analysis and statistics

Fitting of phosphorescence decays was performed either in ImSpector software (widefield PLIM, La vision) or SPCImage software (Becker & Hickl) using single-exponential decay function and pixel binning as appropriate. The resulting 2D matrices with lifetime data were converted to ASCII format and processed in Microsoft Excel to produce O₂ concentration values using calibration function. 3D projections of O₂ scaffolds and 3D projections of spheroids were produced from intensity images representing individual optical sections using Volume Viewer plugin (Fiji software (<http://fiji.sc/Fiji>)), cells stained with CellTox Green and other dyes were counted using '3D objects counter' plugin in Fiji software. Localisation of GPP130 to the lysosomes was carried out using the co-localisation threshold plugin in Fiji software. Data are presented as average values with standard deviation shown as error bars.

Data are shown as average values with standard deviation as error bars. To ensure consistency of results, all the experiments were performed in triplicate. For statistical significance, data were evaluated using independent *t*-test, with confidence levels P=0.05 and P=0.005, indicated with asterisks in figures. Western blotting, qPCR data and localisation experiments were evaluated for statistical differences using *t*-test with confidence levels of P<0.05, 0.005 or 0.001 (marked by an asterisk) accepted as significant. Electrophoretic band intensities were quantified in Fiji software and then averaged between 3 independent experiments with standard deviations are shown as error bars. qPCR experiments were normalised to control β -actin signals and compared between 3 independent experiments.

Chapter 3. Evaluation of novel photoluminescence based O₂ and temperature probes

Abstract

Porous scaffolds are commonly used to produce 3D cell cultures and tissue models. The modification of these materials can significantly increase their uses as well as operational performance. Here we introduce a novel hybrid microporous polystyrene-based scaffold impregnated with PtTFPP, a phosphorescent dye sensitive to O₂ concentrations. Our scaffold falls into the category of solid state oxygen sensors. The scaffolds are compatible with live cell fluorescence microscopy, possess high brightness and stable responses to O₂ in phosphorescence intensity and lifetime imaging modes. They allow for the better control of conditions in 3D tissue cultures, as well as being useful in a broad range of biomaterial and physiological studies. We moved on to evaluate our water soluble, intracellular probes, first looking at a novel intracellular nanoparticle probe capable of measuring O₂. The probe was developed specifically for high resolution imaging of O₂, consisting of a substituted conjugated polymer (poly(fluorene-alt-benzothiadiazole)) which acts as a FRET antenna and a fluorescent reference with covalently bound phosphorescent metalloporphyrin (PtTPTBPF). These nanoparticles displayed efficient high stability, brightness and compatibility with lifetime based imaging modes as well as low toxicity for cells. The positive charge on the nanoparticles ensured high cell staining efficiency, proving to be a versatile tool for quantitative O₂ imaging in HCT116 cells. Finally, we evaluate a new cell-permeable temperature sensitive fluorescence lifetime-based nanoprobe based on lipophilic sulforhodamine. We looked at the probes toxicity when introduced to cells as well as its spectral characteristics. The probe showed cytoplasmic

localisation and has a robust response to T, allowing for quantitative analysis of temperature inside single cells.

3.1 Constructing O₂-sensing scaffold structures for 3D tissue models

Scaffold materials are specifically designed to be porous to allow efficient penetration of gas and nutrients. They must possess the mechanical strength and structures that ensure proper cell growth, adhesion, proliferation, differentiation and migration [291]. A prime example is commercially available Alvetex™, composed of a highly porous polystyrene membrane, about 200 μm in thickness and pore size of approximately 36-40 μm. Alvetex™ scaffolds have prior use in drug screening and toxicity studies [292, 293], as well as brain and spinal cord tissue explants culturing [294]. They ensure structural stability for cell growth, control drug release, allow for measurement of mechanical stress and the quantitative measurement of analytes, including the pH effect on the metabolic function of chondrocytes [295] and growth factor release on cardio spheres [296].

Molecular O₂ is a key metabolite affecting cell function and viability and must be carefully controlled within 3D models [297]. O₂ measurements can be achieved by coupling the phosphorescent quenching method with solid state sensors or probe [227]. Tissue scaffolds potentially allow for the controlled deposition of O₂ sensitive dye, to produce structures with high brightness and sensitivity to pericellular O₂ levels. Using a similar approach O₂ gradients were measured in engineered tissue using planar solid-state phosphorescent O₂ sensors [231]. Scaffolds made from electro-spun PLGA fibres with unevenly distributed nanosensors were also proposed for O₂ and pH detection [298]. Fibre optical micro-sensors have been used to investigate O₂ tension

in human dermal fibroblasts and human bone marrow derived stromal cells grown on collagen type 1 scaffolds [299]. Optical sensors are not invasive nor as unstable as electrode systems [234], but the fibre optic probes, needle type micro-sensors [300], and planar sensors only allow spot measurement of O₂. Fabrication of O₂-sensitive materials from micro-porous polymeric substrates and their studies by phosphorescence lifetime imaging microscopy (PLIM) were recently demonstrated [301, 302]. The same approach can be applied to tissue scaffolds based polymers such as polystyrene which have moderate O₂ permeability [303]. Here we optimised staining of a AlvetexTM polystyrene based scaffold with O₂-sensitive phosphorescent dye PtTFPP, evaluated their O₂ sensitivity, compatibility and general uses with different cell types and tissue models.

3.1.1 Preparation of O₂ scaffolds and their sensing properties

AlvetexTM is made of polystyrene, which is a popular material for O₂ sensor production since it provides moderate quenching of embedded phosphorescent Pt(II)porphyrins by O₂ [303]. The vast network of pores and thin walls facilitated even and complete impregnation of dye using the swelling method [304]. This method uses the low polarity solvent acetone to ensure dye molecules diffuse into the swollen polystyrene [235] (Fig 3.1). The subsequent transfer of the scaffold in the high polarity solvent (water) traps the dye molecules in the polystyrene matrix and provides them with the required sensitivity to O₂. PtTFPP has been shown to have high photostability, brightness and hydro-phobicity. The scaffolds were stained with the optimum dye concentration required for fast uniform staining with minimal damage to the integrity of the membrane structures. A 70:30 ratio of acetone to water ensured the PtTFPP dye dissolved and impregnated the scaffold at 60 °C for 1 h. Other solvents

including tetrahydrofuran, acetonitrile and ethanol, were ruled out due to the damages in the polystyrene and their inability to completely dissolve the PtTFPP. Washing steps ensured excess dye was removed further encouraging uniform staining.

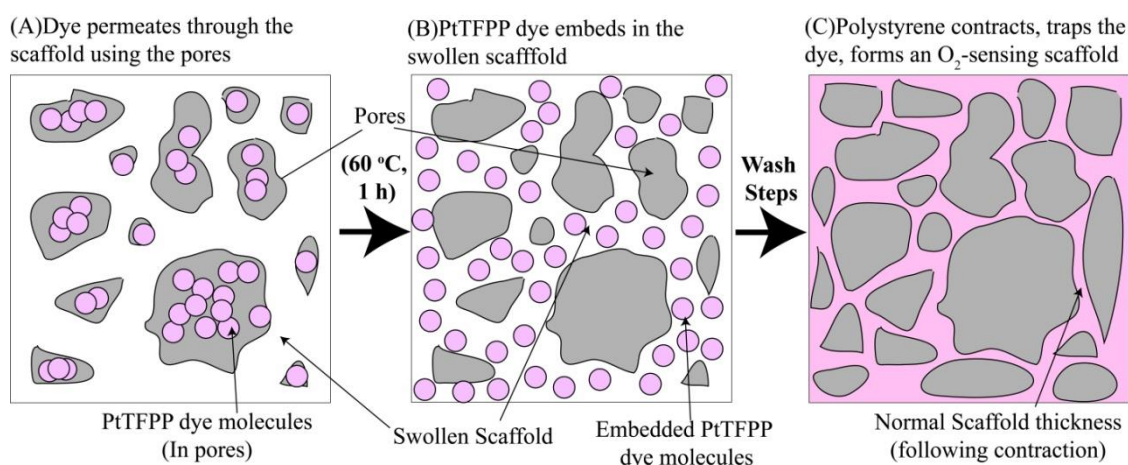


Figure 3.1 Dye (Phosphorescent dye PtTFPP) impregnation of AlvetexTM by the swelling method.

In such conditions, dye impregnation had no effect on the scaffold structure, with the pores remaining the same shape, size and roughness (Fig. 3.2 A) with dye evenly distributed throughout the membrane (Fig. 3.2 B). Scaffolds displayed a useful sensitivity to O₂ across the physiological range 0 %-21 % O₂ i.e. 0-209 μM O₂. The O₂ calibration had a hyperbolic dependence of both intensity and lifetime, displaying a two-fold reduction at 209 μM compared to zero O₂ and curved Stern-Volmer intensity and lifetime plots (Fig. 3.2 C, D). The curve indicated non-ideal dye distribution, which can be explained by the uneven polystyrene surface and pores which when imaged on a wide-field microscope can lead to mild interference of lifetime values. The following equation, obtained according to the two-site model [305], allowed us to convert lifetime values to O₂ concentrations: $O_2 = (0.71108 / (-$

$1+0.71108+\tau/56.5)-1)/0.06414$ ($R^2=0.987$). The bright signals allow the scaffold to be excited at the 500-535nm, green light spectrum, less harmful to cells when compared to the alternative 405 laser.

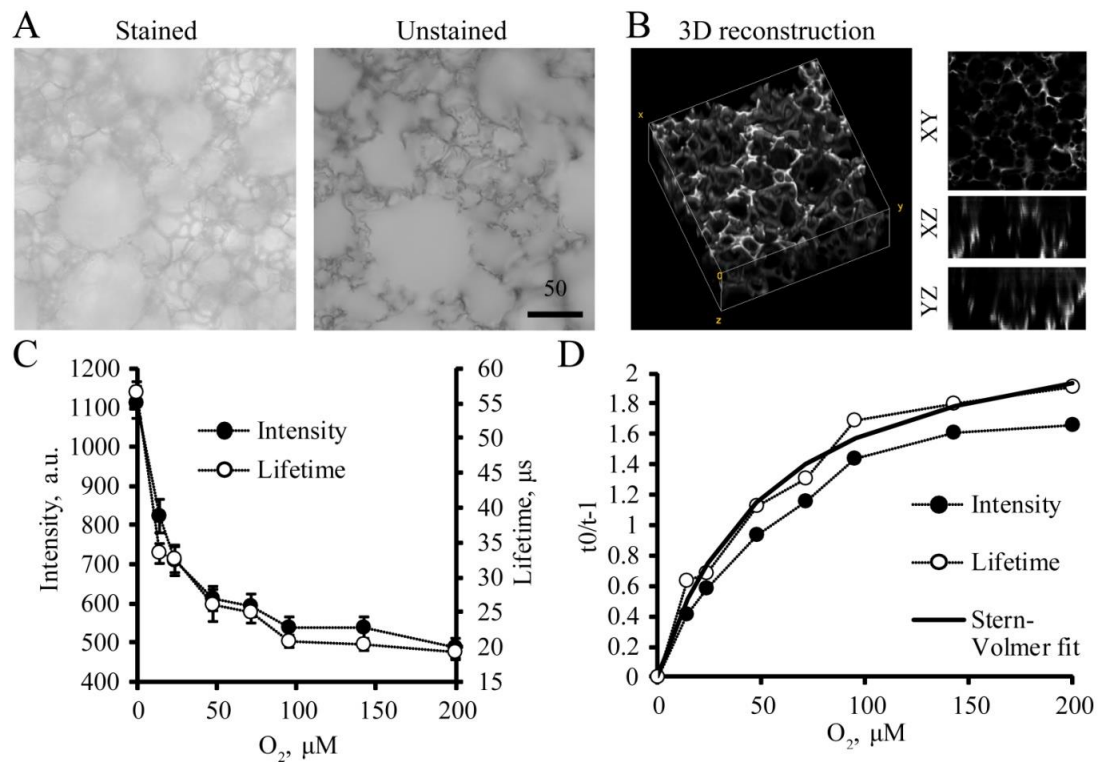


Figure 3.2 O₂ scaffolds optical properties (A) Transmission light images of unstained and PtTFPP-stained scaffolds. Scale bar unit is in μm. (B) Confocal PLIM image of O₂ scaffold dye staining, highlighting 3D (left) and 2D projections (right). 3D image was produced using 25 optical Z sections of 2μm step width (50 μm). (C) O₂ calibration carried out on wide-field PLIM microscope in intensity and lifetime modes. (D) Stern-Volmer plots of O₂ calibration and lifetime calibration fitting using the two-site model (fitting for phosphorescence lifetime is shown). "taken with modification from [73]". N=3.

3.1.2 Cell growth and viability in O₂-sensitive tissue scaffolds

We successfully achieved invasion of multicellular aggregates of PC12 cells in 3D scaffold, providing a structure on which to attach and ensuring the aggregates were surrounded by the O₂ sensitive material (Fig. 3.3 A). We observed similar viability and

morphology of HCT116 cells in unstained and O₂ scaffolds, highlighted with fluorescent dyes Calcein green (cytoplasm) and TMRM (polarised mitochondria), both on the surface and deeper within the membrane (Fig. 3.3 B, D). Comparable numbers of dead cells were also observed in both HCT116 (Fig. 3.3 B [Top]) and PC12 cells (Fig. 3.3 B [Bottom]), when stained with CellTox green dye (Fig. 3.3 C). Furthermore, PC12 cells retaining viability when cultured for at least 5 days (Fig. 3.3 B). These results indicate the scaffold staining with PtTFPP dye has no adverse toxicity effects on cells, promoting cell growth in the same way as unstained scaffold controls.

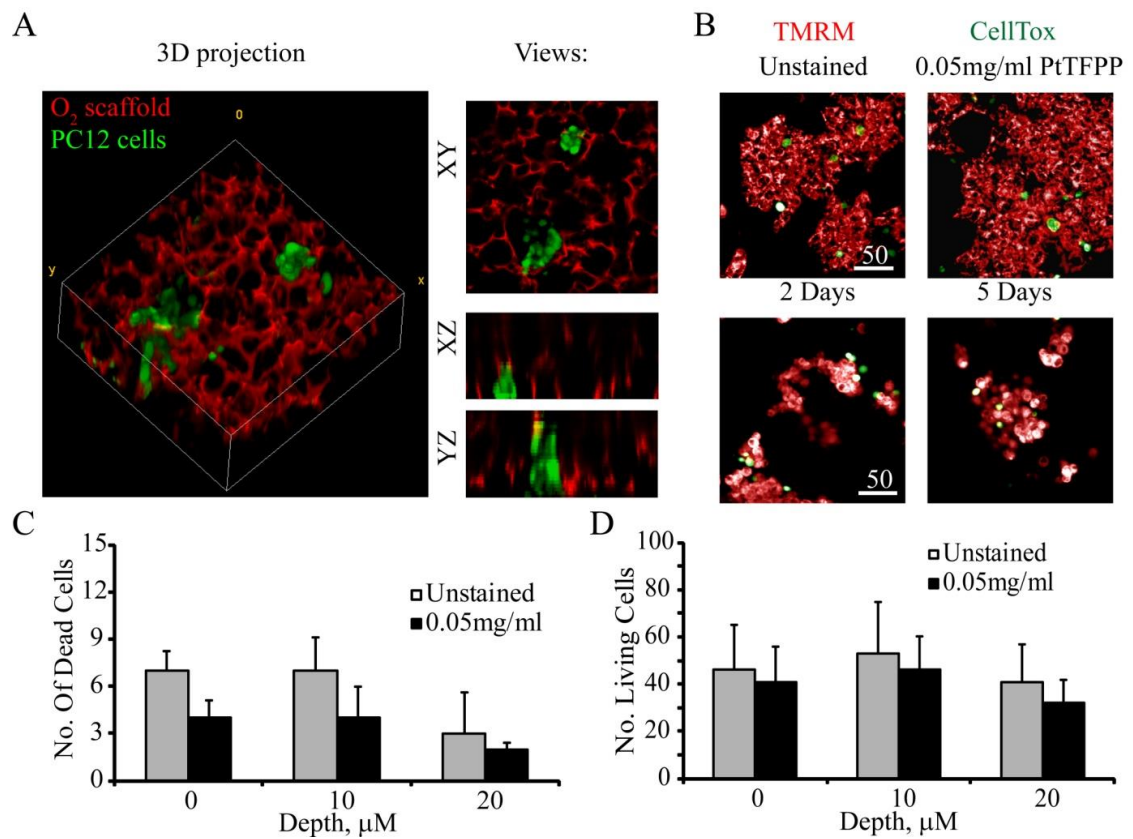


Figure 3.3 Cell viability and growth in O_2 scaffolds. (A) 3D reconstruction of PC12 cells invading the O_2 scaffold (B) HCT116 cells in unstained and O_2 scaffolds with TMRM (20nM, red) and CellTox green (green) [Top], PC12 cells at different times in culture (2, 5 days) stained with viable (TMRM) and dead (CellTox green). (C) Number of dead cells (CellTox green) and (D) Number of living cells (Calcein) at different depths in unstained vs O_2 scaffolds (HCT116 WT cells). N=3.

3.1.3 Monitoring oxygenation of different cell types in O_2 scaffolds

The O_2 scaffolds were seeded with both individual cells forming a monolayer, naturally localising in the top section (5-10 μm depth) of the scaffold and multicellular aggregates that invaded the scaffold to a depth of approximately (50-100 μm). When cells were absent the scaffolds displayed phosphorescence lifetimes of around 21.5-23 μs with very little gradients, maximum 1 μs ($\sim 5 \mu M O_2$) across a 20 μm depth. Following HCT116 WT cell seeding (60,000-100,000 density) a monolayer formed on the scaffolds surface increasing lifetimes by 2-8 μs ($\sim 11-43 \mu M O_2$), significant

changes when compared to the un-seeded controls (Fig. 3.4 A). No in-depth gradients were observed with monolayer cells. PC12 aggregates comprising 10-50 respiring cells were seeded on the scaffolds in serum free media supplemented with nerve growth factor (NGF), ensuring scaffold invasion. Cell aggregates displayed greater lifetime increases compared to the seeding of individual HCT116 monolayer culture. Furthermore, there was greater variation at different depths within the scaffold. Lifetimes ranged from about 26 μ s on the surface (easier access to ambient O₂) near the cells with significant changes deeper into the scaffold were lifetimes reached as high as 36 μ s. Using the calibration function, we found that these lifetimes correspond to O₂ concentrations at around 49-16 μ M respectively. Lowest O₂ concentrations were observed at depths of 10-20 μ m, with the highest levels observed on the surface and at 40 μ m, i.e. the regions usually interacting with the top and bottom portion of the aggregates (Fig. 3.4 B). These gradients can be because of increased cell density and respiration activity in the core of the aggregate as well as due to limitations in glucose and O₂ diffusion.

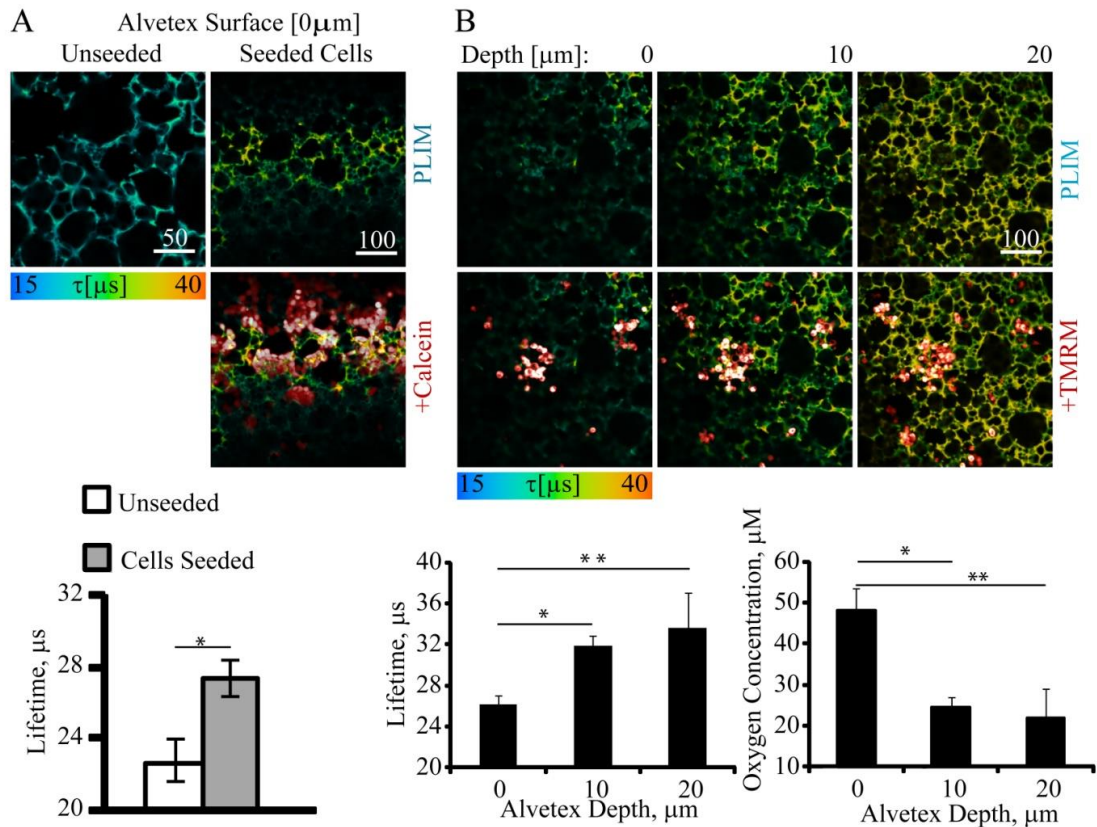


Figure 3.4 Changes in oxygenation of HCT116 and PC12 cells across the depth of O_2 scaffolds, measured by PLIM. (A) Lifetime distributions in un-seeded and HCT116 cell-populated seeded scaffolds. Images of false-colour PLIM superimposed with Calcein-stained cells. (B) Combined PLIM (O_2) and intensity (TMRM, viable cells) images of PC12 cells. Calculated lifetime and O_2 concentrations near cell aggregates at different depths. Three ROIs were taken in regions near cells, for comparison of O_2 at different depths. Scale bar is in μm . Asterisks indicate significant levels of difference with $P=0.05$ (*) and $P=0.005$ (**). $N=3$.

3.1.4 Monitoring gene expression changes in scaffolds because of depth-dependent deoxygenation

Decreases in O_2 availability can lead to PC12 cell differentiation *in vitro* [306]. In hypoxic conditions PC12 cells were seen to increase transcription of tyrosine hydroxylase (TH) gene and stabilise its mRNA [307]. We decided to see if the growth of cells inside the scaffolds experiencing hypoxia affected the cell differentiation. To test this, we seeded 60-100 cell aggregates for 3 days. Following seeding and

incubation with the PC12 aggregates in the scaffolds we first monitored the O₂ concentrations at various depths prior to fixation and immunostaining with anti-TH antibody. As previously observed the lowest O₂ concentrations were at 10-20 μ m depth, which following immunostaining corresponded to highest intensity staining of the TH antibody (Fig. 3.5 A, B). Results show that greater cell differentiation occurs in more hypoxic regions, a process which can be imaged using these O₂ scaffolds.

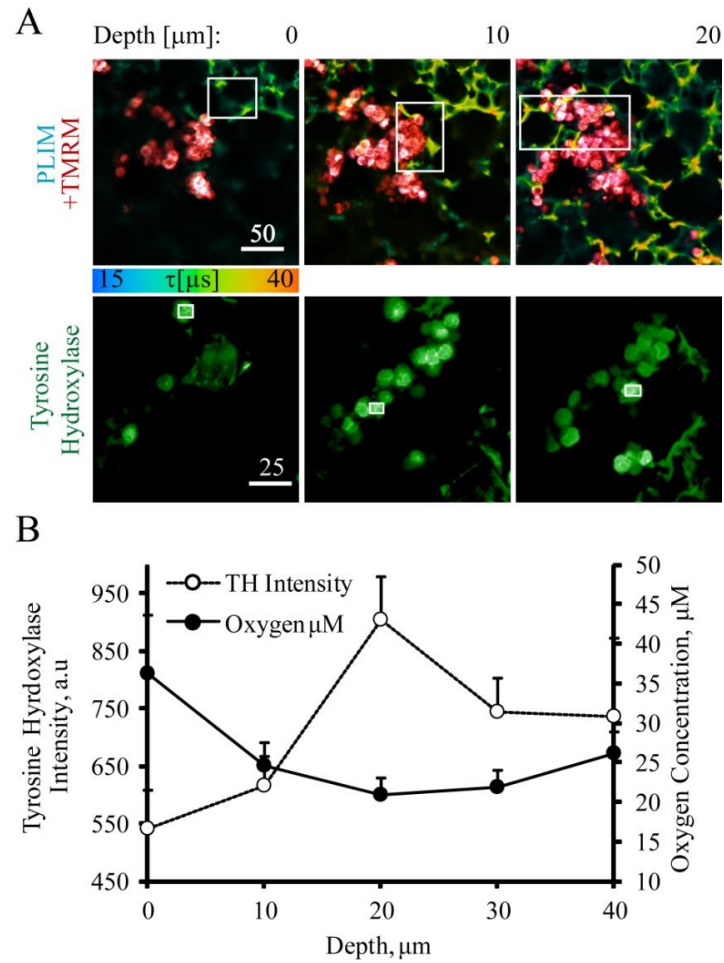


Figure 3.5 Effect of hypoxia on differentiation of PC12 cells. PC12 cells were grown in O₂ scaffolds, analysed by PLIM and immunostained with anti-TH antibody. (A) Superimposed PLIM images (false colour) and TMRM staining (red) (top panel) and distribution of TH-positive cells (bottom) measured at various depths. Scale bar is in μm . (B) Correlation of TH-positive cell staining and O₂ concentration in O₂ scaffold at different depths. Multiple ROIs were taken for regions near or at cells, at each depth for three separate experiments, with examples of chosen regions shown above. N=3.

3.1.5 Metabolic cell stimulation in O₂ scaffolds

To analyse rapid changes in metabolic activity we stimulated the PC12 aggregates with FCCP (an un-coupler that activates respiration) followed by Antimycin A, (mitochondrial inhibitor of complex III). Addition of each drug led to significant changes in phosphorescence lifetimes, measured in the same regions of interest. FCCP

increased the lifetime values by approximately 2-4 μ s, reflecting the increase in respiration activity. These lifetimes returned to resting levels and in some cases decreased following Ant-A addition (Fig. 3.6 A). Lifetime values also varied depending on cell proximity to the scaffold, with lifetimes decreasing in regions of the scaffold far from actively respiring cells (Fig. 3.6 B). The larger aggregates and those that invaded completely showed more profound lifetime changes than those on the surface or smaller groups of cells. This can be explained by the increased distances from atmospheric O₂ deeper in the scaffold and the higher mitochondrial activity in larger PC12 aggregates.

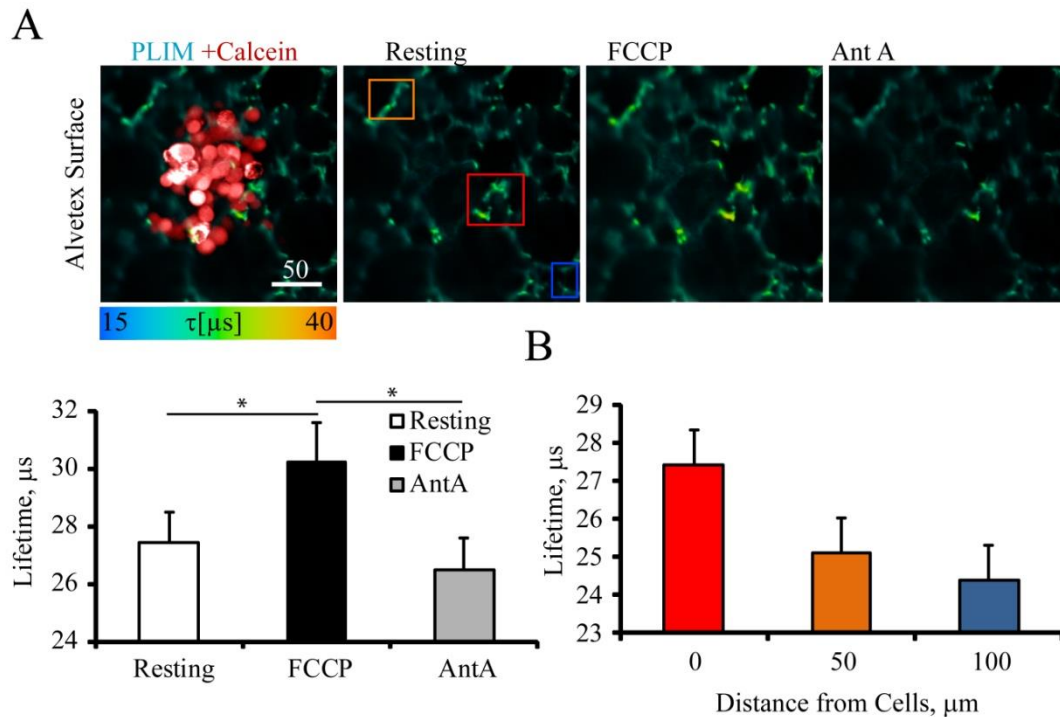


Figure 3.6 Stimulation of cells with drugs affecting cellular respiration in O₂ scaffolds. (A) Effect of FCCP and Antimycin A. Lifetime changes close to cell aggregates (red square). (B) Changes of lifetime with increased distance from the cells, corresponding to the orange, red and blue squares in (A) PLIM image. The very same region (red box in this case), was chosen to compare, resting, FCCP and AntA treated cells. Scale bar is in μm. Asterisks indicate significant levels of difference with P=0.05 (*) and P=0.005(**). N=3.

Here we introduced a non-conventional method for measuring cell oxygenation using a phosphorescent polystyrene scaffold (AlvetexTM). We assessed the toxicity and sensitivity of the PtTFPP O₂ sensitive indicator dye. Furthermore, we monitored cell oxygenation following seeding with various cell types. Using TCSPC PLIM multiplexed with fluorescent markers and immunostaining we correlated lifetime values with toxicity, drug stimulation and gene expression. This technique provides an efficient, non-invasive method of measuring cell oxygenation within 3D constructs via live cell imaging.

3.2 Evaluation of conjugated polymer, nanoparticle-based O₂ probe

Nanosensor probes are of great interest due to their small size ensuring they can easily enter cells and even sub-cellular compartments, and report on intracellular O₂. They respond to changes in O₂ in real time while the indicator dye is shielded with a polymeric shell from possible environmental influences, resulting in stable calibration [136]. Their compatibility with confocal, one- and two-photon microscopy is advantageous [308]. The SII-0.2⁺ probe consists of a conjugated polymer functioning as a matrix which acts as a light harvesting antenna, a reference (O₂-insensitive) fluorescent signal, and a backbone to which an O₂ sensitive dye is covalently bound. The co-polymer is then grafted with charged groups ensuring better cell and tissue penetration abilities as well as increased stability. SII-0.2⁺ has the advantage of being capable of both ratiometric intensity as well as phosphorescence lifetime based O₂ measurements, in the visible (one-photon excitation) or near-infrared (two-photon excitation) spectral ranges [136].

3.2.1 Probe characteristics and optical sensor properties

The measured spectra identified the two peaks, the O₂-insensitive reference dye (520-580 nm) and the O₂ sensitive peak (760 nm). Both were measured in ambient O₂ and following chemical deoxygenation (addition of sulphite). The O₂-sensitive peak showed a 1.5-fold increase while the reference remained unchanged (Fig. 3.7 A). The probe showed efficient staining of monolayer HCT116 cells. Multiplexing with other cell compartment markers revealed that the O₂ probe was located primarily in the lysosomes, displaying strong co-localisation with LysoTracker Red, and absent from the cells mitochondria (TMRM) (Fig. 3.7 B).

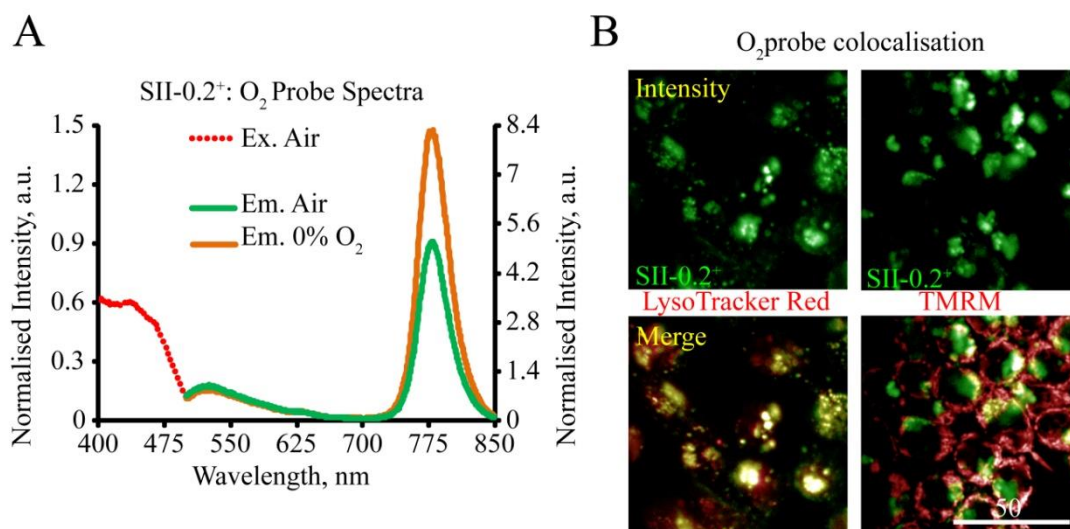


Figure 3.7 Spectral properties of O₂ probe. (A) Normalised fluorescence excitation and emission spectra in water for different O₂ concentrations. (B) Confocal fluorescence microscopy of HCT116 cells, stained with O₂ probe (5 μg/ml, 16 h) and counterstained with LysoTracker Red (Lysosomes, red), TMRM (mitochondria, red). Scale bar is in μm.

It is known that the Pt-benzoporphyrins i.e. the O₂ sensitive dye in the probe shows sensitivity to temperature changes in phosphorescence mode. For this reason, the calibration of the probe was carried out at both 37 and 40 °C. We observed that within these temperatures, most likely to be the normal range in cells and tissues there was practically no significant differences in the calibration equation (Fig. 3.8 A), fitted using the two site Stern-Volmer model and the obtained equation: $O_2 = (0.63485 / (1 + 0.63485 + \tau / 37.7) - 1) / 0.02486$ [242] (Fig. 3.8 B). The lack of significant changes in the calibration curve is most likely because of the narrow ranges in which the calibration is being carried out. In order to ensure that the O₂ probe had no adverse effects on cell viability we conducted cell bioenergetics tests, assessing the effect on total cellular ATP (Fig. 3.9 A) and extracellular acidification rate (glycolytic flux and

Krebs cycle) (Fig. 3.9 B, C) under resting and stressed conditions [309]. Minor toxicity was seen for the O₂ probe at concentrations greater than 20 μg/ml (Fig. 3.9). For this reason, working concentrations between 1-5 μg/ml was chosen, which showed minimal to no toxicity.

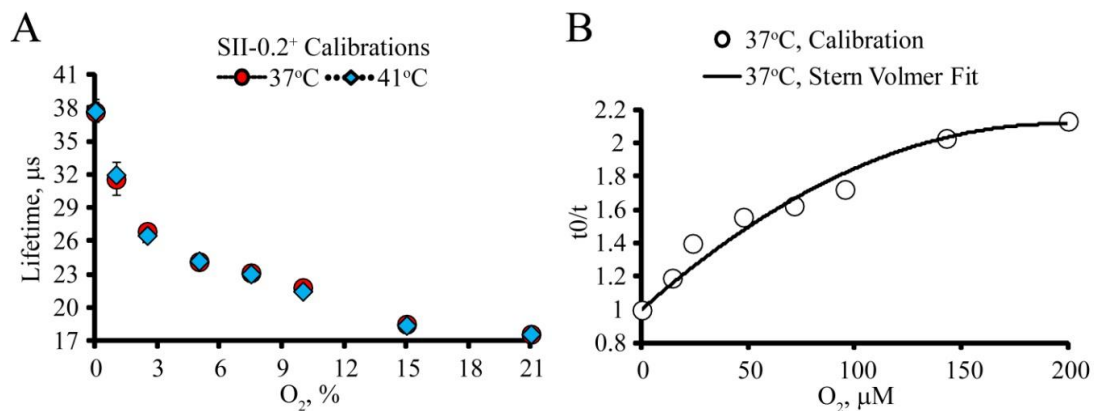


Figure 3.8 Calibration and Temperature dependency of O₂ probe (SII-0.2⁺ nanoparticles). (A) Intracellular O₂ probe calibration produced at 37 °C and 41 °C. (B) Stern-Volmer plot for the O₂ probe.

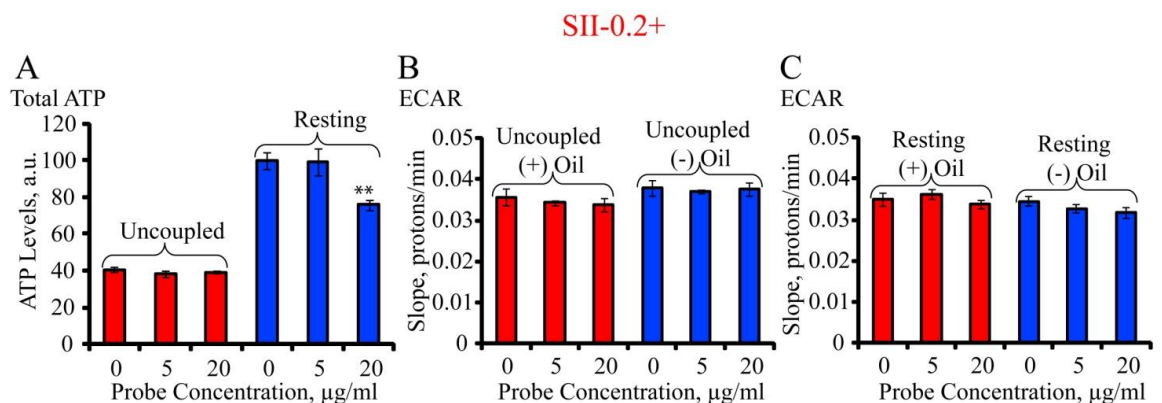


Figure 3.9 Evaluation of dose-dependent toxicity for O₂ probes in HCT116 cells. Cells were stained with the probe at indicated concentration for 17 h and subjected to analysis of total cellular ATP and extra-cellular acidification rate (ECAR) under sealed (total acidification) and unsealed (lactate-related - glycolytic flux) conditions. N=3. Asterisks indicate significance levels of difference with P=0.005 (**).

3.3 Sulforhodamine-based temperature-sensitive nanoparticle probe (T probe)

Temperature is an important factor to be considered in cellular activity as it affects a multitude of processes including a cells physical and chemical processes, energy production, diffusion of bio-molecules and drugs, acid-base reactions, thus must be maintained within definite physiological limits [310-312]. Successful diagnostics and disease therapy including cancer treatment are depend upon controlling and imaging temperature [313, 314]. Detection of temperature via optical methods such as fluorescence allows for live real time imaging of temperature distribution and gradients. Attempts have been made to design FLIM-based nanoparticles and small molecule fluorescent probes capable of imaging temperatures in the cytosol, endoplasmic reticulum and mitochondria [192, 202, 203, 315]. These probes have their limitations, including self-aggregation, cross-sensitivity to biological ions and molecules leading to miscalculations in T-gradients within cells and tissues [316]. For these reasons, it is important to design new cell-permeable T-probes and look at possible interferences, as well as its ability to enter the cell, temperature sensitivity in FLIM mode and toxicity effects. We turned our attention to the hydrophobic sulforhodamine derivative impregnated in cationic nanoparticles via the precipitation method (designed by Prof. S. Borisov, Graz University of Technology, Austria). By modifying the sulforhodamine with aliphatic hydrocarbon tails the hydrophobicity was improved, minimising dye leakage from the nanoparticles as well as preventing cross-sensitivity.

3.3.1 Evaluating the cell staining properties and probe toxicity

The T probe spectra showed that following excitation at around 560 nm it has an emission peak at 570-580 nm (Fig. 3.10 A). Results also showed that efficient staining

occurred in the HCT116 cells used. The T probe showed prominent diffused staining in the cytoplasm with little co-localisation with the endosomal (Cholera Toxin) and mitochondrial (Mito-Tracker Green) probes. There was co-localisation with the lysosomes (SII-0.2⁺ and NanO2), with these regions displaying higher staining intensities and higher lifetime values compared to the cytoplasm (Fig. 3.10 B). Efficient staining was observed with concentrations of 1-2 $\mu\text{g/ml}$ for 16-24 h.

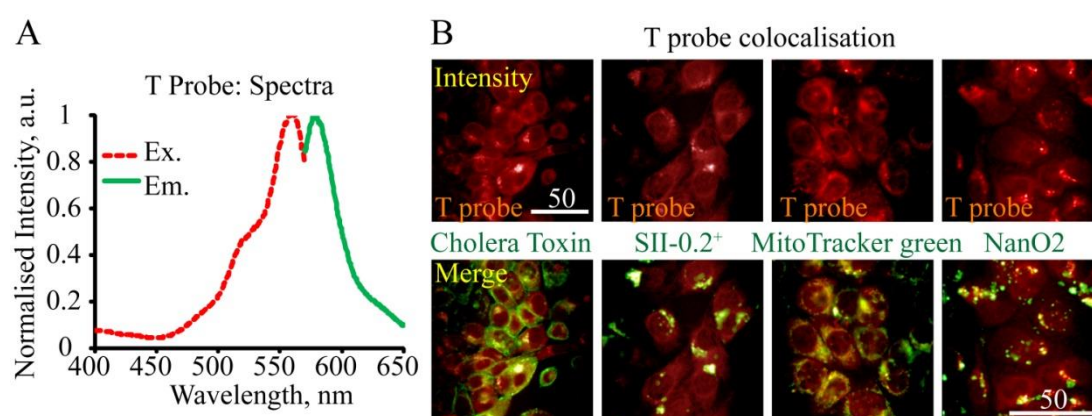


Figure 3.10 Spectral properties of T probe and intracellular localisation. (A) Normalised fluorescence excitation and emission spectra for T-sensitive nanoparticles (25 °C). (B) Confocal fluorescence microscopy of HCT116 cells, stained with T probe (1 $\mu\text{g/ml}$, 16 h red) and counterstained with Cholera toxin (endosomes), O₂ probe (Lysosomes), Mito-Tracker Green (mitochondria) and NanO2 (another nanoparticle probe) (all shown in green). Scale bar is in μm .

Staining of cell monolayer displayed uniform distribution of fluorescence lifetime and temperature values (Fig. 3.11), a decay that could be fitted with a mono-exponential fit, over the range 2.2-2.8 ns (25-42 °C). A fraction of higher lifetimes indicating lower temperatures were found in the lysosomal compartments (Fig. 3.12 A). However Lysosomes have a higher acidity compared to the rest of the cell, (pH 4.5-5) and as such may be adversely affecting the probe and its lifetime values [280]. For this

reason, the lifetimes found in the lysosomes were not used for analysis, taking away only a small fraction available for use in each cell (Fig. 3.11). As a control, we used free dye (without encapsulation into nanoparticles), which showed similar intracellular accumulation. However free dye displayed concentration dependence of lifetime values, had a narrower calibration than the nanoparticles indicating decreased sensitivity to temperature (Fig 3.12 A, B, D). The T probe i.e. nanoparticles, showed a linear calibration in cells very like that measured with the probe in water when compared to free dye (Fig 3.12 B, C).

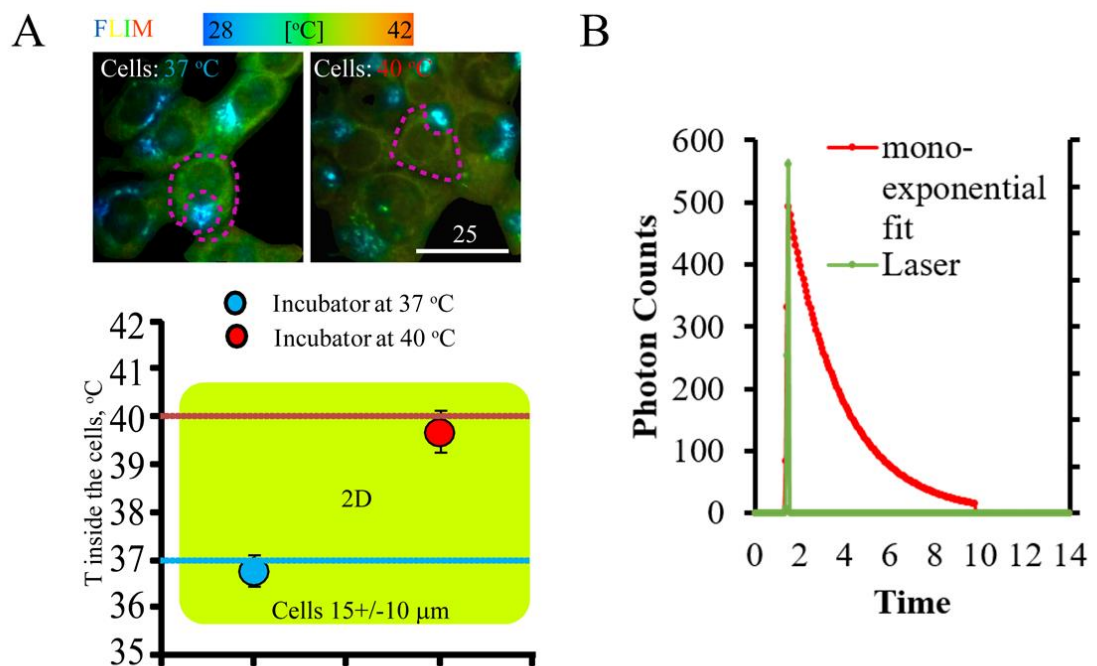


Figure 3.11 Evaluation of temperature distribution in adherent (2D). (A) Cells were exposed to 37 and 40 °C and measured by FLIM for internal temperature in regions indicated by pink dashed lines. (B) Example of a mono-exponential fitting of decay, for cells imaged at 40 °C. Scale bar is in the μ m.

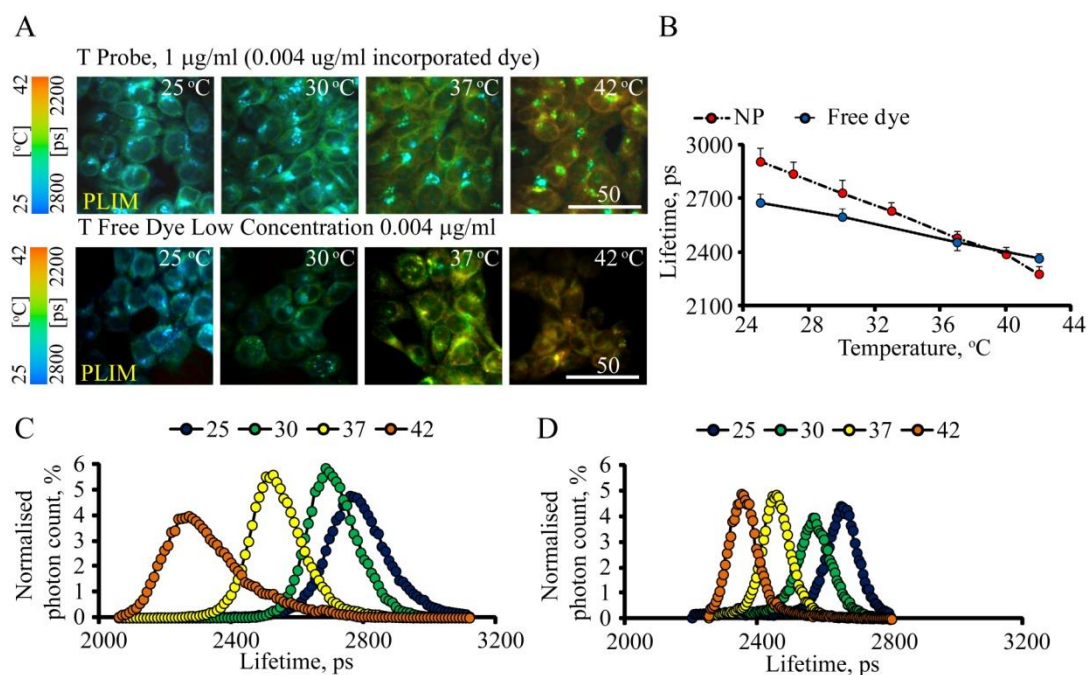


Figure 3.12 The comparison of in cell temperature calibrations for sulforhodamine encapsulated in RL100 nanoparticles and in free dye form. (A) FLIM images of adherent cells stained with dye or nanoparticles for 16 h at indicated concentrations and measured by FLIM microscopy at different temperature. (B) Comparison of in cell calibration for sulforhodamine in nanoparticles and in free dye. (C) Fluorescence lifetime distribution histogram for nanoparticles. (D) Fluorescence lifetime distribution histogram for sulforhodamine dye in free form. Scale bar is in μm .

The T probe was subjected to the same toxicity tests as the O_2 probe chapter 3.2. We again assessed the effect of nanoparticles on total cellular ATP (Figure 3.13 A), extracellular acidification rate (glycolytic flux and Krebs cycle) (Figure 3.13 B, C), under resting and metabolic stimulation conditions. The T probe showed no significant toxicity for concentrations 1-2 $\mu\text{g/ml}$ following 16-24 h staining in monolayer cells.

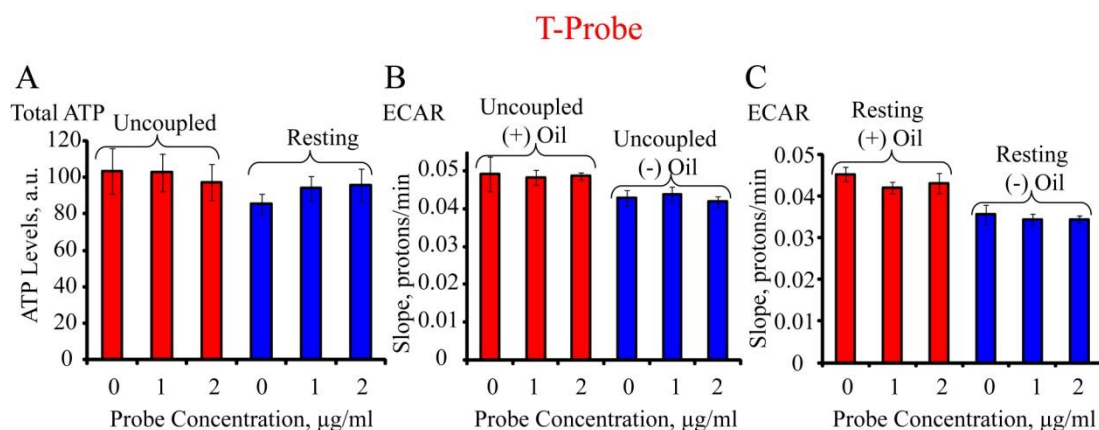


Figure 3.13 Evaluation of dose-dependent toxicity for T probes for HCT116 cells. Cells were stained with the probe at indicated concentration for 17 h and subjected to analysis of total cellular ATP and extracellular acidification rate (ECAR) under sealed (total acidification) and unsealed (glycolytic flux) conditions. N=3. Asterisks indicate significance levels of difference with P=0.005 (**).

The newly developed O₂-sensitive porous polystyrene scaffolds and nanoparticle probes measuring either O₂ or temperature have shown positive results. The O₂ scaffolds provide an excellent platform for 3D culture formation, with a stable O₂ calibration capable of monitoring pericellular O₂. They were shown to be non-toxic ensuring, cells retain viability, functioning normally when grown on the PtTFPP stained membranes. Scaffolds have shown uses in monitoring gene expression via immunostaining as well as monitoring oxygenation following metabolic stimulation.

The intracellular nanoparticle probes allow for live real time intracellular imaging of O₂ and temperature, monitoring their dynamic changes within cells. They display stable calibrations and are immune to adverse effects by external stimuli in the physiological ranges of O₂ and temperature measured.

Over all the described sensors and probes provide an excellent option for monitoring O₂ and temperature gradients and distribution in the cell and small tissues. They will

aid research involving the study of the effects of O₂ and temperature on gene expression, disease progression and morphological studies.

Chapter 4. Physiological imaging studies with 3D tissue models and new probes

Abstract

In this chapter, we first compare three different spheroid methods, looking at size, uniformity and viability, determining the best method for a physiologically relevant *in vivo* like model. We were then able to combine our chosen method with our novel O₂ and T probes in several interesting studies. We conducted a drug toxicity study, looking at the effect of the anti-cancer drug in both a scaffold based system and scaffold free spheroid model. We monitored the toxicity effects of chemotherapeutic drug tirpazamine, measuring O₂ changes using either our new O₂ sensitive scaffolds or intracellular O₂ nanoparticles. We carried out a metabolic study evaluating T and O₂ gradients in 3D spheroids using the fluorescent lifetime imaging microscopy (FLIM) technique. We found heterogeneous gradients of T and O₂ in our spheroid model absent in the 2D monolayer. Gradients were enhanced by treatment with mitochondrial uncouplers or dissipated by drug induced disaggregation (cantharidin led to the destruction of the spheroids tight spherical structure). Finally, we looked to elucidate the function of SPCA2, in colon cancer HCT116 cells. We discovered SPCA2 was upregulated in hypoxia (3 % O₂) in both 2D adherent cells and 3D spheroids. Using our intracellular O₂ probes we observed O₂ concentrations as low as 30-50μM in our spheroids, measured by phosphorescent lifetime imaging. We also noted that cells exposed to hypoxia showed an overall increase in S phase-positive cells, hypothesising that SPCA2 upregulation in hypoxia is linked to Mn²⁺ dependent cell cycle arrest. Our results point at an important role for SPCA2 in regulating cell cycle progression in cancer cells.

4.1 Optimisation of spheroid models

4.1.1 Spheroid formation methods

Spheroids are the clusters of cells that self-assemble excreting their own extracellular matrix. Tumour spheroids are characterised by gradients in bio-molecules, nutrients, temperature and O₂ while maintaining similar cyto-architecture to cells *in vivo* [317]. There are numerous methods for spheroid production with the "free floating" culture method as one of the most widespread [54]. It relies on culturing cells in serum-free media with additional growth factors, FGF and EGF (Fig 4.1 A). This method ensures cells do not attach to the cell culture flask, as well as simultaneously encouraging cells aggregation. Another method is the use of hydrophobic round bottom wells such as Lipidure™ plates. These plates have a coating comprised of 2-methacryloyloxyethyl phosphorylcholine (MPC), the same structure as polar phospholipids, having a hydrophilic nature with minimal toxicity. The phospholipid layer preventing attachment to the plate (Fig. 4.1 B). "Hanging drop" uses gravity force and specially designed plates to form spheroids within the meniscus of medium. Cells are suspended in a droplet of media ensuring that they have no other option than to aggregate (Fig. 4.1, C). This method is more expensive and labour intensive compared to "free floating" [318, 319]. All the described methods help forming multi-cellular tumour spheroids, however we deemed it necessary to further investigate whether there were significant differences in the quality of spheroids produced by the different methods regarding size, uniformity, metabolic activity and viability [320].

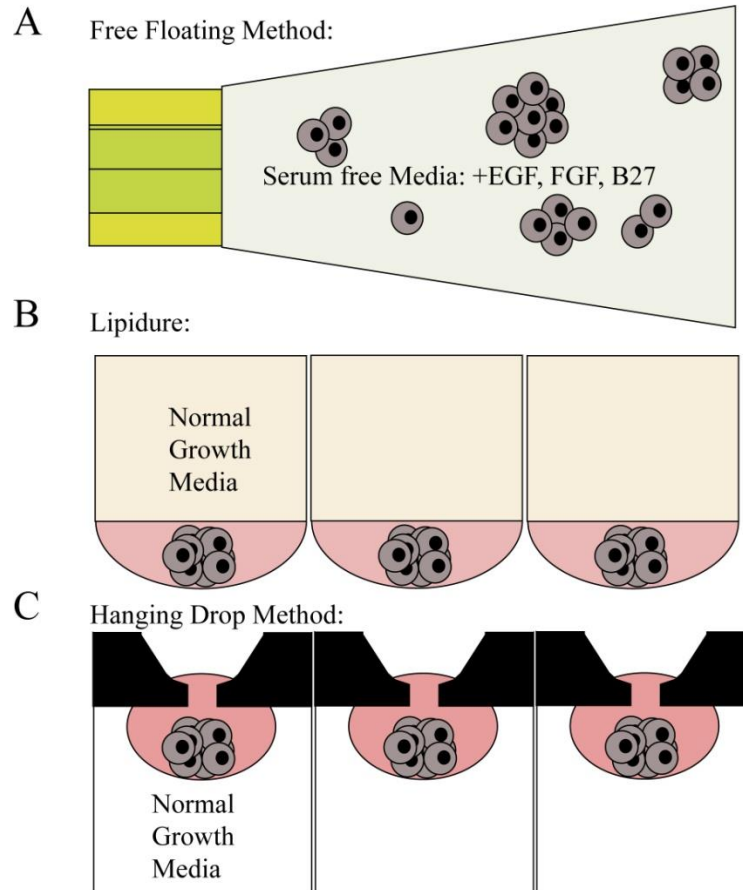


Figure 4.1 Schematic showing the different spheroid formation methods. A. "Free floating". (B) LipidureTM. (C) "Hanging drop".

4.1.2 Optimisation of the size and shape of 3D spheroid model using three different methods of production

We compared three different spheroid production methods using HCT116 colon cancer cells: "free floating" culture, LipidureTM and "hanging drop", looking for the method capable of creating uniform sized spheroids combined with ease of handling. The "free floating" culture had the greatest variation in shape and size with little possibility for controlling either. Both the LipidureTM and "hanging drop" method produced spheroids of more uniform size and spherical shape with excellent reproducibility and control (Fig.4.2 A, B).

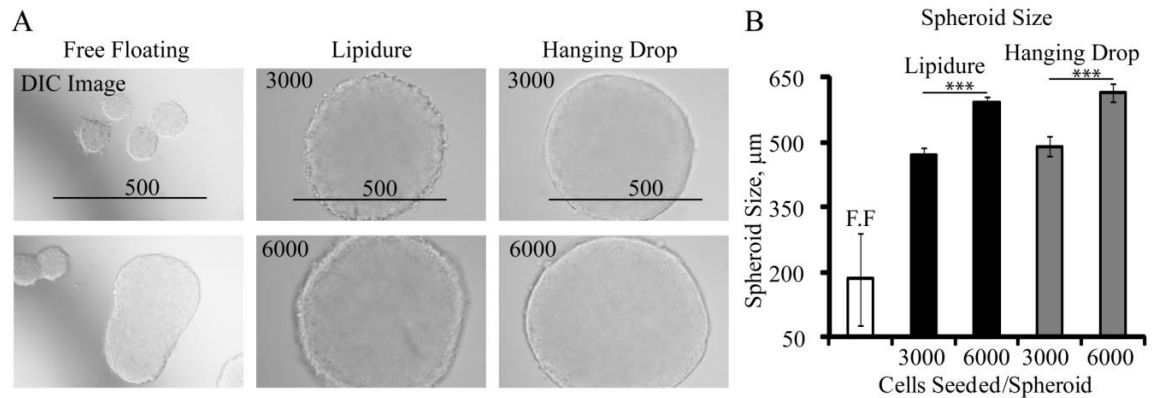


Figure 4.2 Comparison of spheroid sizes for three different formation methods, "free-floating" formation (FF), LipidureTM and "hanging drop". All spheroids were three days old. (A) Transmission light images of spheroids produced by different methods. (B) the variation in sizes of produced spheroids. Scale bar is in μm. ***Asterisks indicate confidence levels (significant difference) $P < 0.001$. $N = 3$.

4.1.3 Cell viability and proliferation capacity

We analysed cell death in spheroids formed by different methods using live cell viability stains. The CellTox Green stains cells with impaired membrane integrity, revealing performance of the production methods (Fig. 4.3 A). The lowest number of dead cells were seen in LipidureTM spheroids produced by seeding 3000 cells per well, while the cell death was significantly higher for similar sized spheroids produced using "hanging drop" (Fig. 4.3 B). Interestingly the number of dead cells increased with size of spheroids, thus while cell death results are low for "free floating" culture this may be because of the relatively small spheroids formed by this method when compared to the other two. Also, since "free floating" method does not allow to control size, the cell death variability was high (Fig. 4.3). CellTox informs on cell death caused primarily by necrosis. We also compared cell death caused by apoptosis using CellEventTM caspase 3/7 substrate. Unlike the CellTox staining there were no significant differences because of high variation in apoptotic cell death between

methods, but it did follow a similar trend as necrotic cell death, with Lipidure™ plates showing the highest viability (Fig. 4.4).

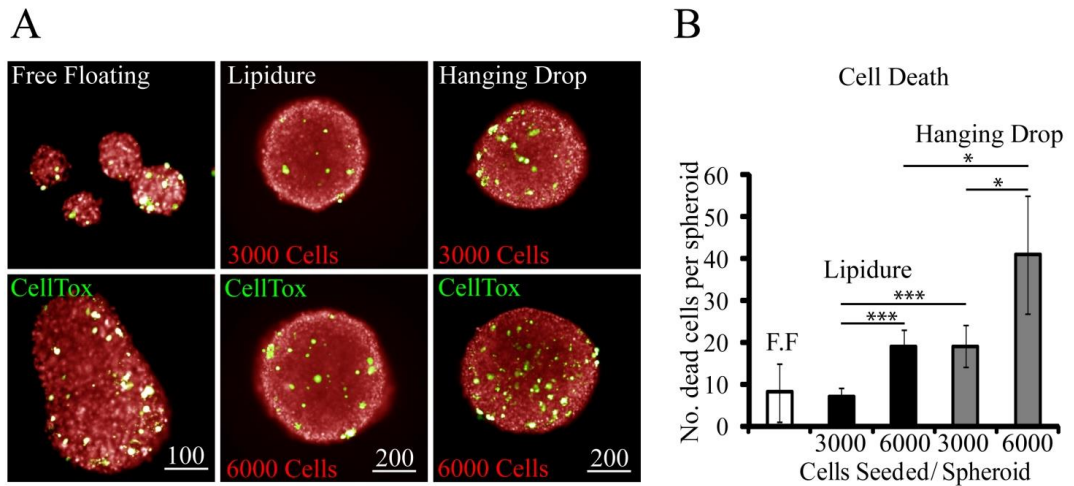


Figure 4.3 Comparison of cell viability in three different production methods. (A) fluorescent intensity of spheroids stained with marker of membrane integrity (CellTox Green, 0.2 % v/v, 3 days) and O₂ probe (NanO₂, 5 µg/ml, 3 days, intensity image). Spheroids were 3 days old. (B) the average number of dead cells per typical spheroid of 100-500 µm size. Scale bar is in µm. *Asterisks indicate confidence levels (significant difference) P<0.05, ***P<0.001. N=3.

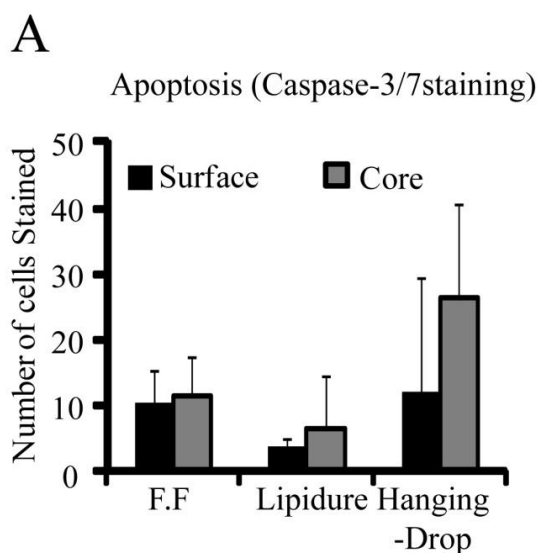


Figure 4.4 Comparison of apoptotic cell death using three different production methods. (A) number of apoptotic cells visualised using CellEventTM caspase 3/7 (2 μ M, 3 days) per typical spheroid of 100-500 μ M size. N=3.

We chose the stain TMRM (marker of polarised mitochondria) to label metabolically active cells in spheroid culture. Only the periphery showed TMRM staining in pre-formed spheroids, showing poor penetration of the marker into the core. Highest intensity TMRM staining, indicating more active mitochondria, was observed in LipidureTM and "hanging drop" spheroids, compared to the "free floating" method (Fig. 4.5 A, B). Another indicator of cell vitality is the ability to divide and replicate, which can be monitored by incorporation of BrdU (a marker of cell proliferation) [321]. Again, the higher number of proliferating cells were seen in the spheroids produced by LipidureTM and "hanging drop" methods. The replicating cells were located primarily on the periphery of the spheroids with little to no staining in the core (Fig. 4.6 A, B). This may explain why the smaller "free floating" spheroids had significantly smaller numbers of proliferating cells, due to their much smaller size. The final test of cell viability was the analysis of cellular ATP, which showed high

viability using the Lipidure™ and "hanging drop" methods (Fig. 4.7). Using Lipidure™ and "hanging drop" it was possible to measure the ATP produced by one single spheroid (easily transferred to a single well in the 96-well plate), with the small standard deviations indicating uniformity in cellular viability per spheroid, using these formation methods. The ATP measurements using the "free floating" method were difficult as the number of spheroids added to each well varied from 12-18. This made it impossible to account for the cellular viability of a single "free floating" spheroid, highlighting the methods' incompatibility with this measurement technique and problems regarding ease of use. These tests served to highlight the importance of controlling spheroid size, regarding proliferation and cell viability, an impossible task using the "free floating" method, putting it at a great disadvantage to the other two methods.

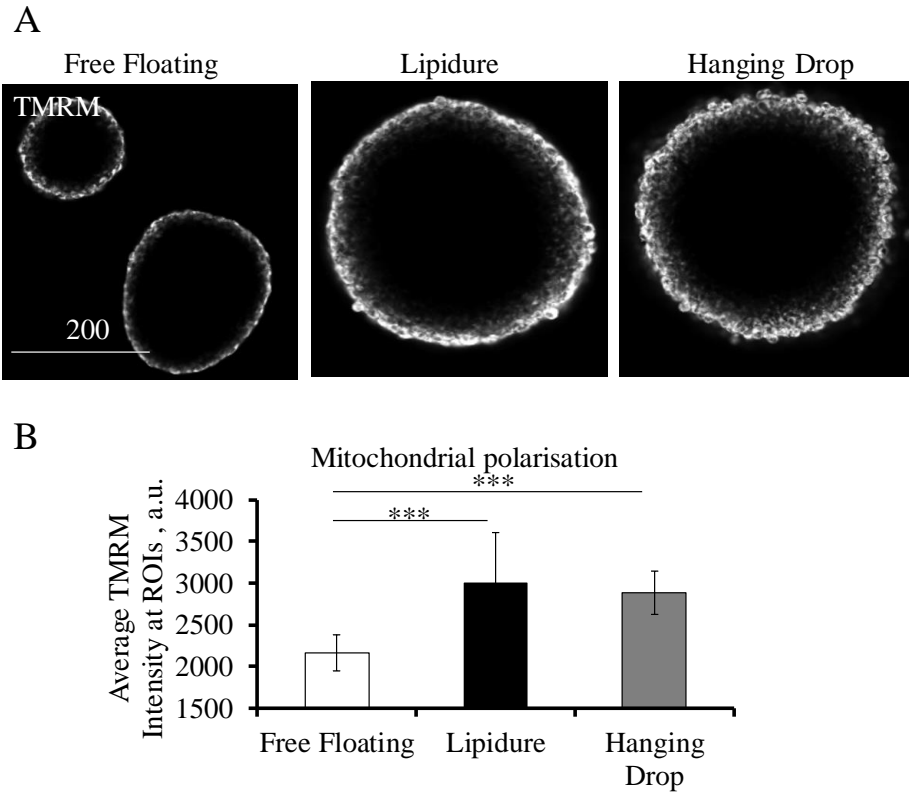


Figure 4.5 Assessment of mitochondrial membrane potential in spheroids. (A) Representative intensity images of spheroids with live cell staining with TMRM (20 nM, 30 min) (B) graph showing the average intensity staining values for TMRM. Scale bar is in μm . TMRM intensity values were taken from 3 stained regions (ROIs) of the spheroids periphery, following imaging at the widest point of the spheroid (What we considered to be the centre). This was carried out for 3 separate spheroids per each method, combining average staining values. ***Asterisks indicate confidence levels (significant difference) $P < 0.001$. $N = 3$.

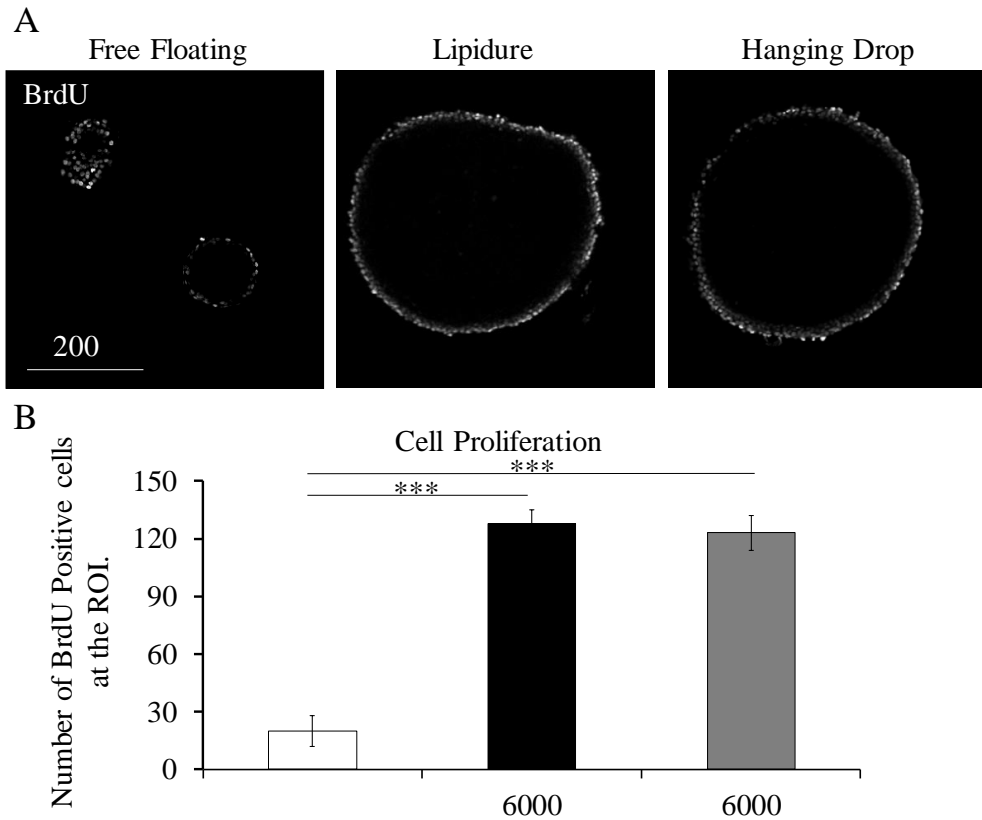


Figure 4.6 Assessment of cell proliferation in spheroids. (A) Representative images of spheroids labelled with BrdU (blue). (B) graph showing the average number of BrdU stained cells per spheroid. BrdU cells were counting using fiji software at the widest point spheroid, what we refer to as our ROI (This Z plane what we considered to be the centre of the spheroid). This was carried out for 3 separate spheroids per each method, combining average number of BrdU positive cells). On the X axis, 6000 is the number of cells seeded per spheroid (For free floating the number of seeded cells per spheroid is unknown). Scale bar is in μm . ***Asterisks indicate confidence levels (significant difference) $P < 0.001$. $N = 3$

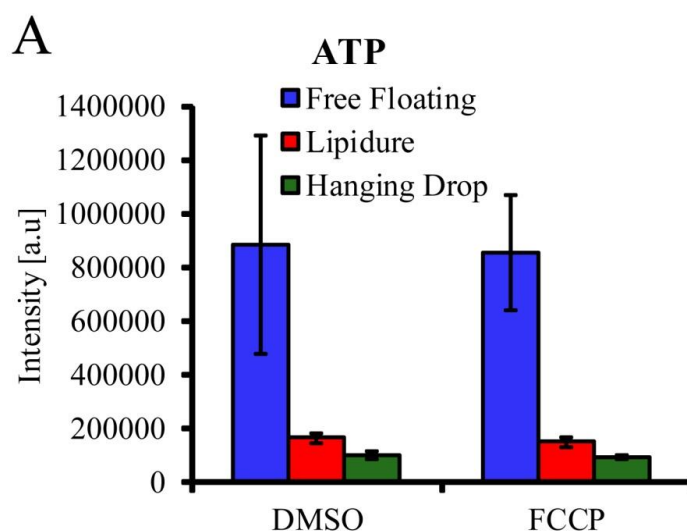


Figure 4.7 Comparison of total cellular ATP (CellTitre-Glo assay) by three different methods. Luminescent signals of the CellTitre-Glo reagent (Promega) were measured on a time-resolved fluorescence plate reader Victor2 (Perkin Elmer) in 96-well plates.

4.1.4 Further evaluation of the Lipidure™ method

The above initial testing showed that Lipidure™ was the favourable method in terms of viability, ease of handling and uniformity. Thus, we chose this method to carry out further experiments. DAPI staining of cell nuclei revealed that cells seeded at a density of 1,000 for 3 days had between 2,500 and 3,500 cells per spheroid (counted using DAPI staining and “3D objects counter” plugin in Fiji software) and a diameter of spheroids in the range of 400-450 μm (Fig. 4.8 A). This provided a calibration relating cells seeded and the size of spheroids formed following a set period of time (Fig. 4.8 B), which is useful when you aim to produce spheroids of a specific size.

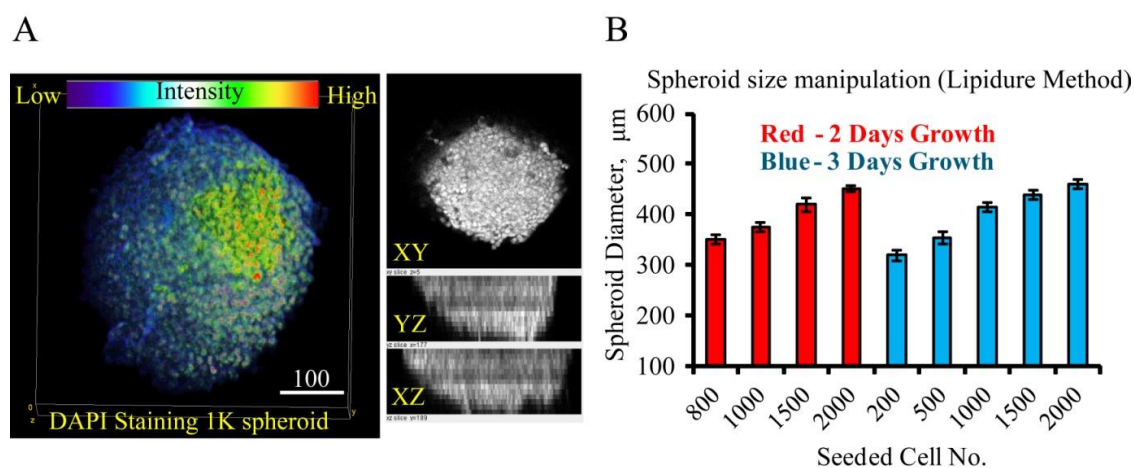


Figure 4.8 Controlling spheroid size using the LipidureTM method. (A) 3D reconstruction of spheroid with DAPI-stained nuclei. (B) Spheroid size dependence on the number of seeded cells with LipidureTM method. Scale bar is in μm .

4.1.5 Staining of spheroids with nanoparticle probes and imaging of O_2 and T gradients

In chapter 3 we chose O_2 and temperature sensitive nanoparticle probes, allowing intracellular staining of monolayer culture upon 16-24 h incubation. However, staining efficiency often decreases when the 3D tissue model is used instead of monolayer cultures [278]. Nanoparticle probes often lack the ability to penetrate the core of the structure of 3D cell models and instead stain only a fraction of the periphery (see e.g. Figs 4.5, 4.6). When we applied SII-0.2⁺ nanoparticles to the formed spheroids only a small cross-section of the spheroid was stained efficiently, mainly the surface (Fig. 4.9 B). However, this problem was negated by adding the probe at the very beginning of the culturing process, at the cell seeding phase. This method of continuous staining ensured excellent staining through-out and uniform distribution (Fig. 4.9 A). In contrast, the T probe did not require continuous staining but instead showed deep penetration following addition to the media 17h prior to imaging when the spheroids were fully formed (Fig. 4.9 C).

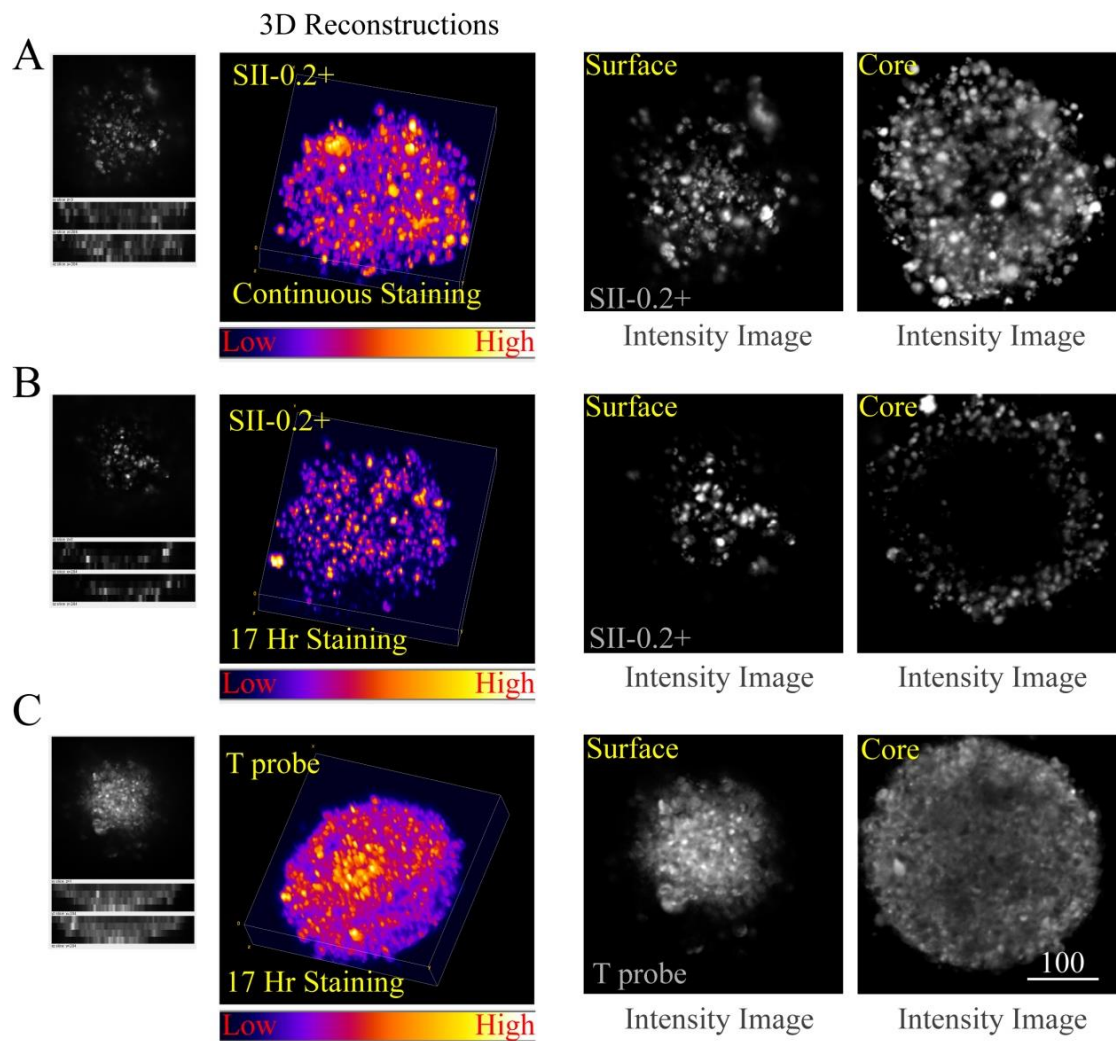


Figure 4.9 Optimising probe staining in multi-cellular tumour spheroids. (A) Post formation staining with O₂ probe (5 μg/ml, 17 h). (B) Continuous staining with O₂ probe (5 μg/ml, 3 days). (C) Post formation staining with T probe (1 μg/ml, 17 h).

The aim of 3D tissue models such as spheroids is to mimic *in vivo* conditions for the cells. One aspect of these models is the presence of prominent gradients, which are because of different O₂ diffusion patterns and uneven distribution of nutrients. Following staining optimisation it was possible to image using either PLIM (O₂ probe) and/or FLIM (T probe) the distribution of the respective analyte. Results showed that gradients in both O₂ and temperature existed in the Lipidure™ spheroid model: the

lowest O₂ values indicated by higher phosphorescence lifetimes were observed in the core of the spheroid, with higher O₂ concentrations located at the periphery where there is less of a barrier to the ambient O₂, and lower density of actively respiring cells (Fig. 4.10 A). Similarly, the highest temperatures were measured in the core, corresponding to the lower lifetime values of the FLIM probe. The difference in temperature between the periphery and core was approximately 2-3°C (Fig. 4.10 B). We think that such gradients also occur *in vivo* [322], and that our Lipidure™ spheroid model can be used for mimicking natural tumour tissue.

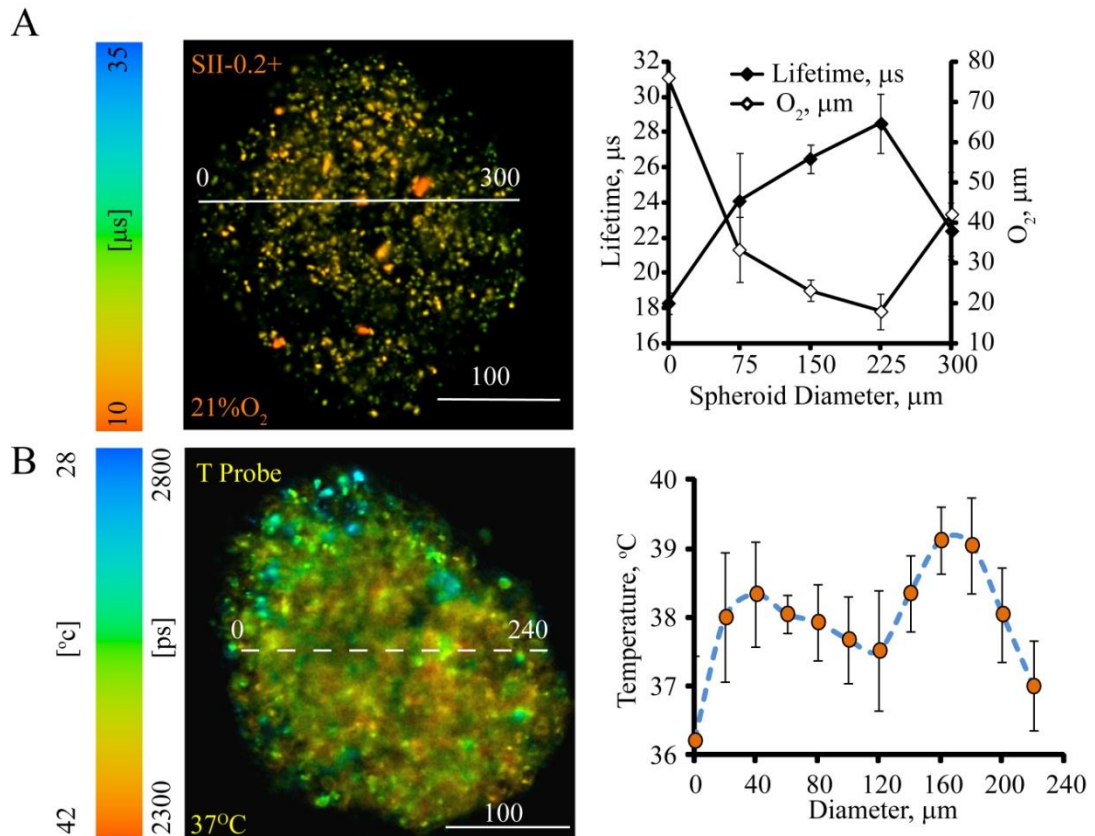


Figure 4.10 O₂ and Temperature gradients in LipidureTM spheroids. (A) False colour PLIM image of the core of a spheroid (Left) and the corresponding O₂ profile across the diameter of the spheroid, for the white line, region of interest (Right). (B) FLIM false colour image of the cross section of HCT116 spheroid stained with T probe and the corresponding graph showing the temperature profile across the spheroid. Scale bar in μm .

Although on the surface spheroids tend to look uniform and similar regardless of the method of production we found that they display some intrinsic differences. Using fluorescent stains that are capable of monitoring cell death, cell viability, as well as shape and size we could select a method of formation which we deemed better for physiological studies than the other two options. Furthermore, using this method, we could identify further advantages for our tumour model including the ability to predict size based on seeding and formation of natural O₂ and temperature gradient at resting

conditions. The probes were also capable of in-depth efficient staining of our 3D tumour model.

4.2 Measuring O₂ changes following drug stimulation in two different 3D models

4.2.1 PC12 cell aggregates seeded in O₂ sensitive scaffolds

Hypoxia is a characteristic feature of tumours, thus some new anti-cancer drugs are being developed that are effective under low O₂ [323]. One promising approach is the design of prodrugs that are activated in hypoxic regions. Following accumulation they are reduced by reductases and produce free radicals [324]. An example is tirapazamine (TPZ) which blocks DNA repair in hypoxic cells [325]. We wondered if TPZ action can be studied in PC12 cells grown in O₂ scaffolds, with monitored O₂ near cells (chapter 3.6). To assess cell survival and death, we also employed live cell imaging dyes CellTox Green (membrane integrity) and TMRM (mitochondrial tracer) and correlating it with cell oxygenation (Fig. 4.11 A, B). The addition of 1 mM TPZ led to a significant increase in cell death compared to the control after only 40 minutes. The most severely affected regions were at depths of (10-20 μm), with an almost 4-fold increase in cell death when compared to the DMSO-treated controls (Fig. 4.11 C). The highest cell death correlated with regions previously measured as significantly more hypoxic (20-30 μM, O₂), while the lowest was seen at the surface where cells have greater accessibility to O₂ (Fig 3.4B, Fig 4.11 C). The TPZ was indeed more active in hypoxic regions (Fig. 4.11 D), thus the more physiological environment in the scaffold ensured TPZ effects are quicker when compared to reported data on A459 cells (48 h-long treatment) in a micro-fluidic system [326]. Thus, hybrid O₂ sensitive scaffolds provide a platform on which to measure the effects of hypoxia and drug treatment on a mini tumour tissue model.

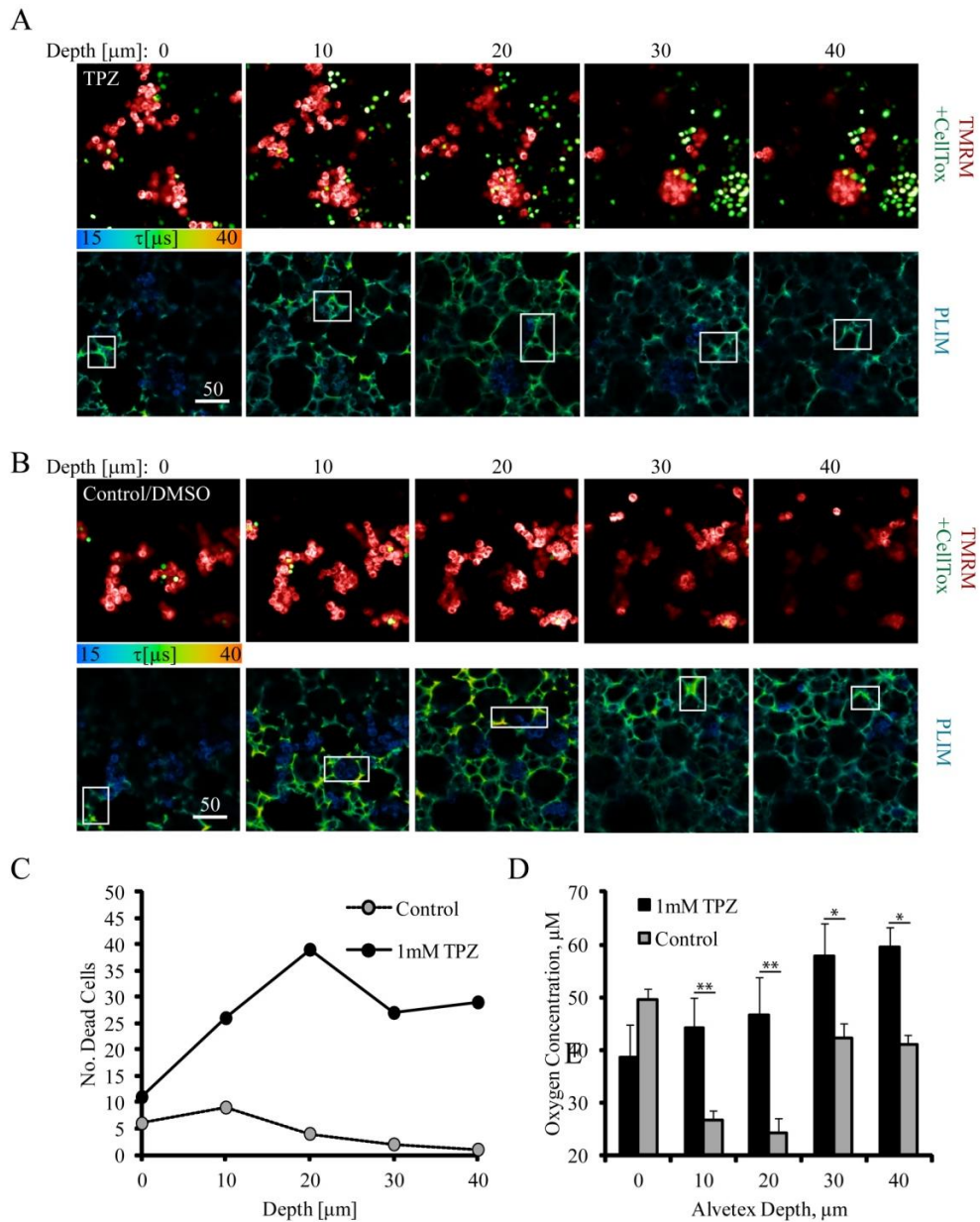


Figure 4.11 Cell death in PC12 aggregates treated with TPZ correlated with in-depth O_2 gradients. (A) TMRM (red) and CellTox staining of cells treated with 1mM TPZ (Top) and corresponding PLIM images (false color). (B) Similar images for control (1% DMSO-treated) samples. Scale bar is in μm . (C) Correlation of the number of dead cells and (D) O_2 concentration at different depths for TPZ-treated and control cells. ROIs were chosen near living (TMRM stained) cells for all samples. ROIs were chosen near living (TMRM stained) cell aggregates, for control and drug treated samples. Asterisks indicate significant levels of difference with $P=0.05$ (*) and $P=0.005$ (**). $N=3$.

4.2.2 TPZ treatment of HCT116 tumour spheroids

Measuring the core region of tumour spheroids using the O₂ nanoparticle probe, we noticed very low O₂ levels, while in cells closer to the periphery concentrations were significantly higher due to the proximity to ambient O₂ (Fig. 4.10 D). Again, we aimed to see whether TPZ had a different effective across the spheroid, like results in our O₂ scaffolds. First the treatment time and concentration of the TPZ were optimised. Effects became apparent after 16 h incubation at a concentration of 0.5 mM. Incubation times are much longer than with the O₂ scaffolds, perhaps due to the increase in the size of the spheroids compared to the PC12 aggregates, the different cell line, the more compact structure and the lack of pores facilitating drug transport.

Imaging both TMRM and O₂ using SII-0.2⁺ showed a decrease in the viability of cells near the core of the spheroid correlating with lower lifetime values in TPZ treated samples (Fig. 4.12 A, B). Decreased viability was indicated by lower TMRM (mitochondrial membrane potential) staining (Fig. 4.12 C), higher numbers of dead cells and an increase in O₂ concentration (Fig. 4.12 D, E). Higher O₂ levels were caused by the decrease of viable respiring cells as the drug took effect.

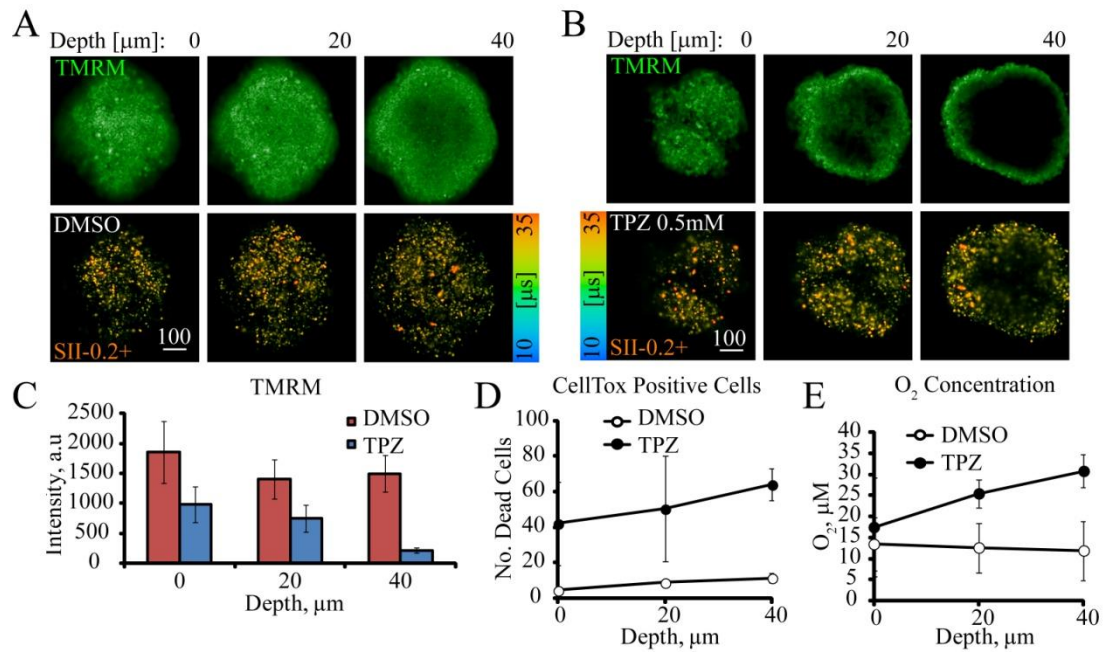


Figure 4.12 Monitoring of TPZ action in SII-0.2⁺ stained HCT116 spheroids. (A, B) PLIM images (false color scale) of spheroids treated with DMSO (mock) and TPZ (0.5 mM) respectively for 16 h. Spheroids were also stained with TMRM (mitochondrial membrane potential, green). (C) TMRM staining for DMSO samples vs TPZ samples. (D, E) Measured cell death using CellTox (0.2 %, 3 days) and oxygenation via PLIM imaging (SII-0.2⁺, 5 $\mu\text{g}/\text{ml}$, 3 days) respectively for both DMSO and TPZ-treated samples. ROIs were chosen at similar regions for control and drug treated samples, avoiding the centre of spheroids, where no measurements were possible for drug treated samples, most likely because of dead cells. Scale bar is in μm . N=3.

Two different 3D systems one scaffold based (AlvetexTM), the other non-scaffold based (spheroids), displayed similar gradients in O₂, with lower concentrations measured in the core. Both systems proved to be useful in monitoring drug effects on a more physiologically relevant model, informing on changes associated with cell respiration rate and viability. The anti-cancer drug tirapazamine, effective in hypoxia, led to significant increases in cell death in the core of both the scaffold and spheroid. Furthermore, increases in O₂ were observed as the viability of the cells decreased.

4.3 Simultaneous monitoring of Temperature and O₂ gradients in tumour spheroid

4.3.1 Measuring dynamic changes in O₂ and temperature distribution

Numerous studies have shown the presence of O₂ gradients and other nutrients in 3D tissue models. O₂ gradients exist in 3D cell aggregates with a diameter greater than 50 μm [54, 327]. This suggests that gradients in temperature may exist in similar sized models. To test this, we multiplexed both the O₂ probe and the T probe, measuring in real time the O₂ and temperature within metabolically active HCT116 spheroids, exposed to temperatures of 37 and 40 °C in an incubator. Gradients in the spheroid core were observed for both temperature and O₂, with higher temperature (2-3 °C) and lower O₂ (10-15 μM decrease) levels, when compared to the periphery (Fig. 4.13). Our data also showed that the O₂ levels were affected by changing temperatures. When the external temperature was increased to 40 °C the spheroid core additionally heated up to about 41 °C, but it became significantly more oxygenated (Fig. 4.13 D). The reason for this decrease in O₂ may be due to the changing balance of energy production pathways, switching from oxidative phosphorylation to glycolysis, faster diffusion of O₂ inside spheroids or decreased cell viability as the temperatures rose to critical levels.

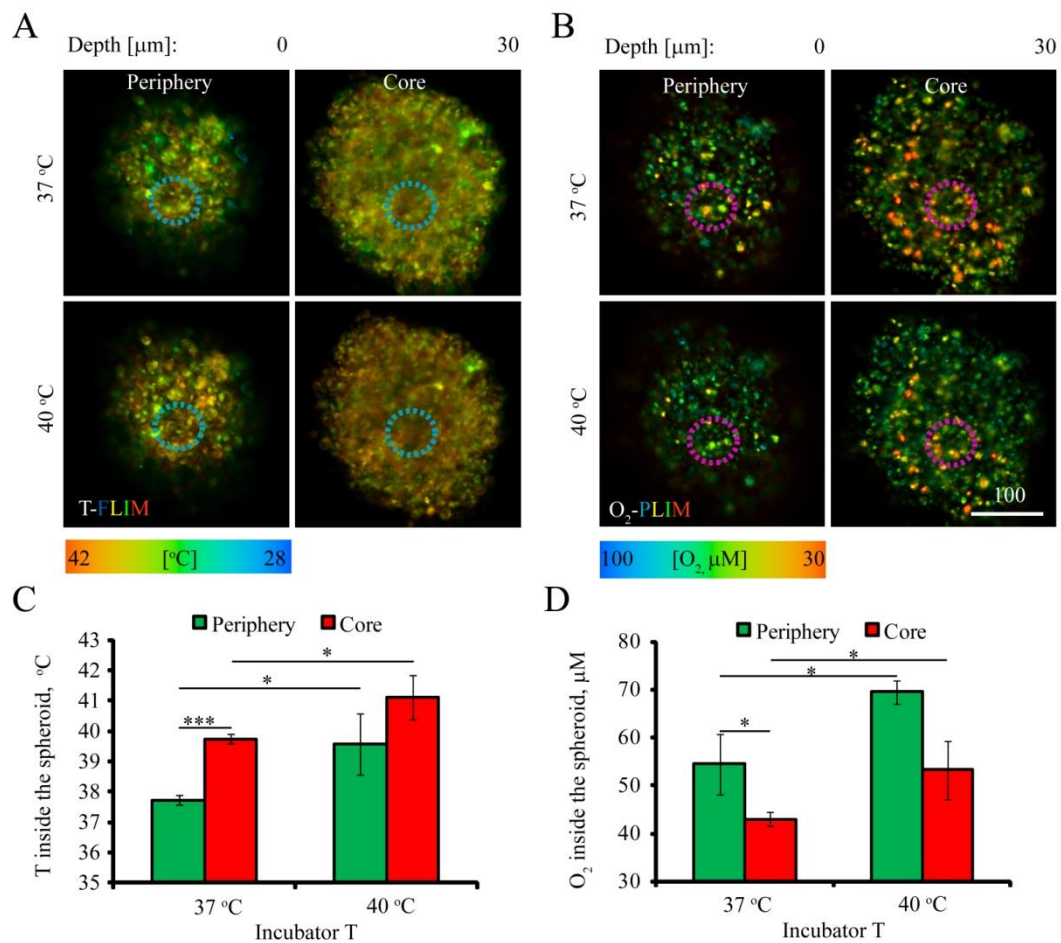


Figure 4.13 Comparison of T and O₂ gradients in resting HCT116 spheroids. Spheroids were stained with O₂ and T probes, exposed to different temperatures and measured by FLIM-PLIM microscopy at 0 and 30 μm depths. (A, B) Examples of FLIM images of T probe (Left) and PLIM imaging of the same spheroids for O₂ probe (right). (C, D) Measured temperatures at the core and periphery of the spheroid at 37 and 40 °C (left), and measured O₂ concentrations for the same regions of the same spheroid (right). Three ROIs with values averaged were taken for the periphery (Top, surface portion of the spheroid) and the core (30 μm depth at the centre of the spheroid) for comparison, per spheroid. The very same regions were taken again following changing of the incubator temperature. Scale bar is in μm Asterisks indicate significance levels of difference with P=0.05 (*), P=0.001(***)). N=3.

4.3.2 Destabilising the 3D structure of spheroids using HSP70 inhibitor cantharidin

To confirm that the spheroid cell density and compact structure contribute to the formation of these T and O₂ gradients, we attacked its structural integrity, using the

drug cantharidin. When the HCT116 spheroids were treated with HSP70 pathway inhibitor cantharidin (CAN) they lose the ability to remain as aggregates as well as their compact, spherical shape (Fig. 4.14 A, B, C). Using our probes, we compared temperature and O₂ before and after CAN treatment and spheroid disaggregation. Indeed, the loosely bound drug-treated spheroids showed increased O₂ levels and temperatures, approaching ambient levels, more like monolayer culture (Fig. 4.14 D, E, G, H). Spheroid disaggregation was confirmed by transmission light microscopy and TMRM staining, highlighting mitochondrial membrane potential. The control spheroids show higher intensity TMRM staining, indicating high viability in spheroid culture, while CAN led to significantly decreased staining (Fig. 4.14 C, F). As the spheroids lost their structural stability the gradients in temperature and O₂ began to disappear.

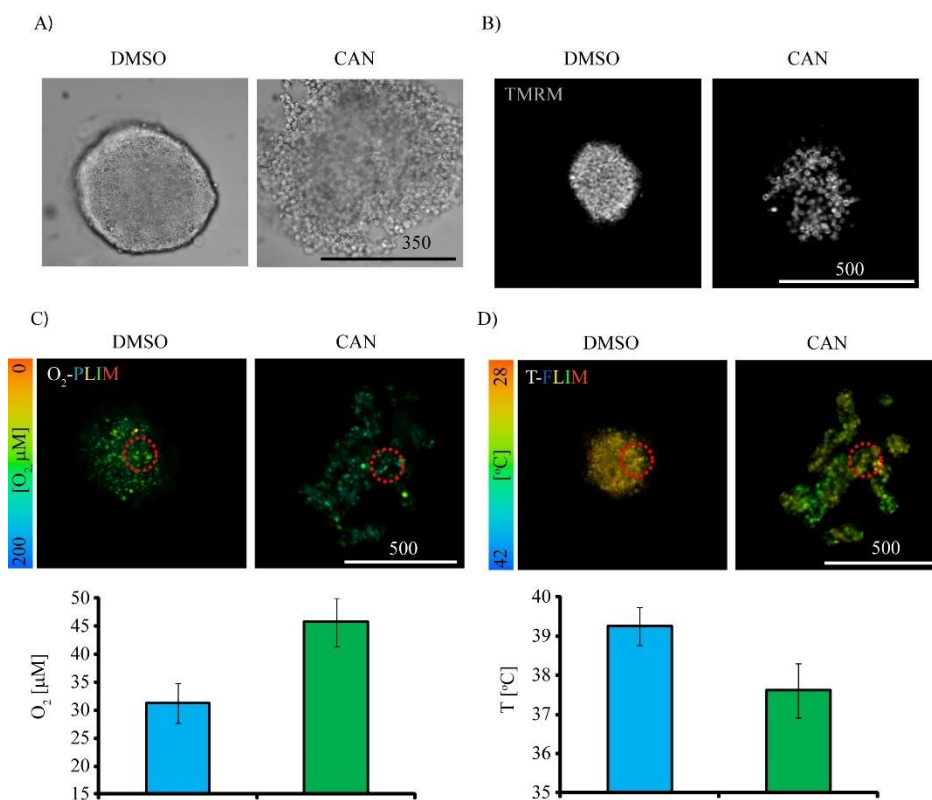


Figure 4.14. Disaggregation of spheroids diminishes the T and O₂ gradients. HCT116 cell spheroids treated with cantharidin (CAN, 5 μM, 3h) at 37 °C, were analysed. DMSO was used as control. A: Transmission light microscopy. B: Staining with mitochondrial membrane potential probe, TMRM (20 nM). C: O₂ Representative PLIM images (top) and calculated mean O₂ values (bottom). D: Representative FLIM images (top) and average T values (bottom). ROIs were chosen from the periphery for comparison i.e. Surface of the spheroid (not in-depth, 0 μm), areas near the outer edges of both formed spheroids and disintegrated spheroids, due to there being no inner areas for those treated with cantharidin. Scale bar is in μm. N=3.

4.3.3 Effect of metabolic stimulation on gradients of temperature and O₂

HCT116 spheroids were treated with the mitochondrial un-coupler FCCP in conjunction with oligomycin (complex V inhibitor), achieving maximal uncoupling [223] and increasing respiration. Treatment led to de-oxygenation of spheroids as a result of increased O₂ consumption following uncoupling, similar to previously described reports [283, 328]. The O₂ decrease correlated with an increase in temperature throughout, with the core showing approximately 2 °C difference

following stimulation, in spheroids of 200-250 μm size (Fig. 4.15 A, B). In contrast, spheroids produced from non-respiring *SCO2*^{-/-} cells revealed drastic difference in response to uncoupling: no changes in T and O₂ were detected. *SCO2*^{-/-}-spheroids also displayed core temperature nearly equal to ambient, and higher overall oxygenation, compared to wild-type cells (Fig. 4.15 C, D). These results indicate that T gradient in HCT116 spheroids is largely dependent upon oxidative phosphorylation and mitochondrial membrane potential.

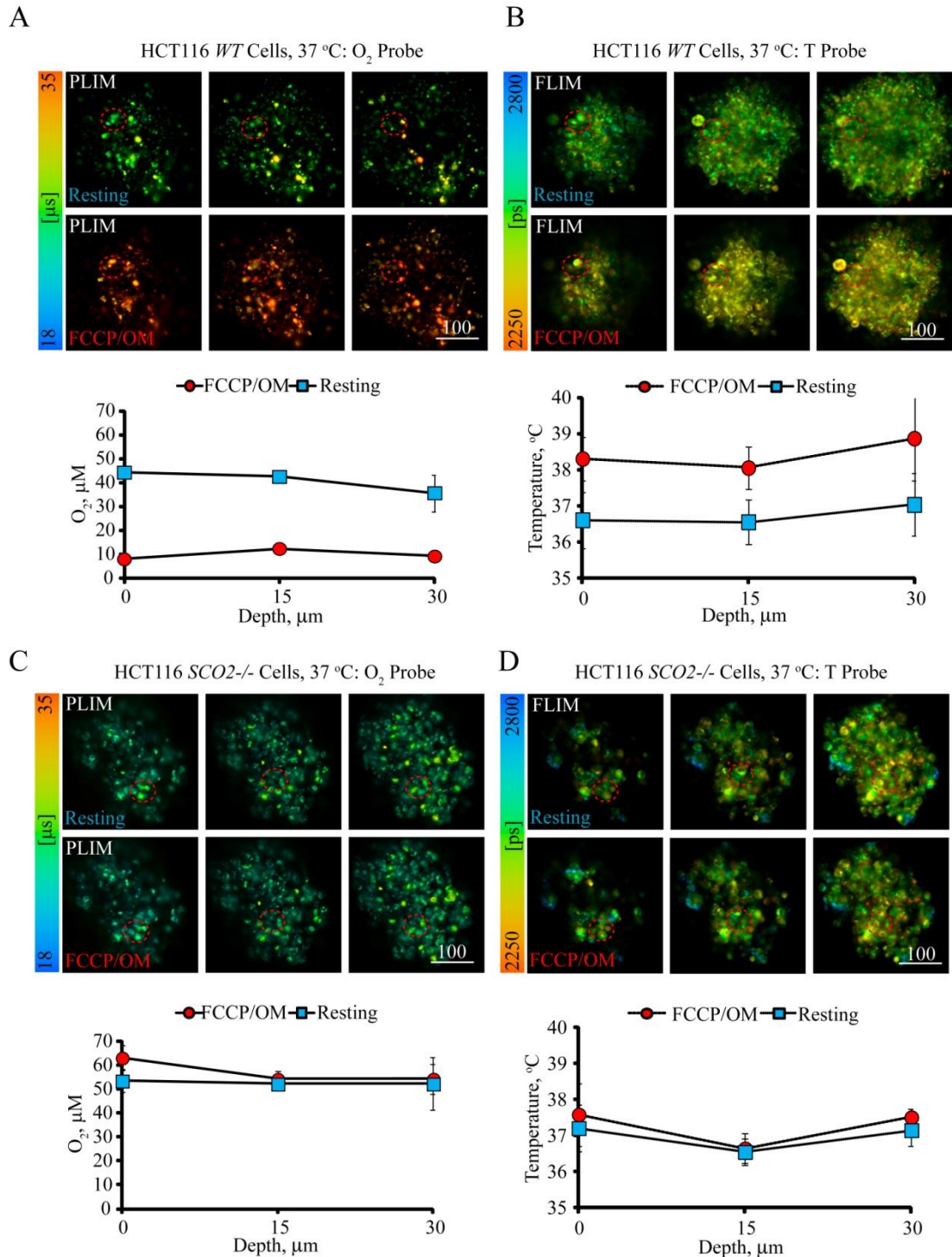


Figure 4.15 The gradients of T and O₂ upon metabolic stimulation in spheroids. Spheroids were produced from respiring wild-type HCT116 *WT* (A, B) and OXPHOS deficient HCT116 *SCO2*^{-/-} (C, D) cells stained with T and O₂ probes and measured by FLIM-PLIM microscopy before and after stimulation (4 μM FCCP, 10 μM oligomycin, 10 min). As they are the same spheroid the very same ROIs were chosen for resting and following FCCP treated. Scale bar is in μm. N=3.

Our results demonstrate that regarding the regulation of both temperature and O₂, 3D tissue models prove to be a much more physiological compared to conventional 2D culturing. This will be of great importance in helping us understand tumour biology, aiding in anticancer drug development, as well as improving therapies and interpretation of T and O₂ effects on metabolism. Our combined imaging of temperature and O₂ using the FLIM/PLIM method has great potential for applications when combined with other tissue models in cancer biology and regenerative medicine.

4.4 Ca²⁺/Mn²⁺-ATPase, SPCA2 is regulated by O₂ availability and affects Mn²⁺ dependent cell cycle progression in colon cancer cells

SPCA2 is an important Ca²⁺/Mn²⁺ ion transporter located in the membranes of the secretory pathway, more specifically the Golgi compartment and endosomes [329, 330]. It is highly expressed in tissues including the lungs, gastrointestinal tract, mammary gland during lactation as well as in some cancer cell lines [281, 329, 331-333]. SPCA2 has an affinity to Ca²⁺ comparable to SERCA2, one of the main Ca²⁺ transporting systems while also having the ability to transport and regulate cytosolic concentrations of Mn²⁺ [334]. Several transporter systems including SERCAs, Na⁺/Ca²⁺ exchangers and PMCAs ensure the regulation of Ca²⁺ in eukaryotic cells [335, 336] maintaining a resting level of 100 nM in the cytosol. Mn²⁺ transport is controlled by manganese homeostasis proteins [337], however to date only a few of these transporters have been identified and the understanding of mechanisms of manganese homeostasis are not well characterised. Acting as a cofactor to metallo-enzymes including oxidases, kinases and DNA/RNA polymerases [337, 338], Mn²⁺ has the ability to scavenge free radicals and regulate ROS formed in hypoxia [339]. Increases in the Mn²⁺ dependant manganese-containing superoxide dismutases (MnSOD) are observed in hyperoxia or in regions with high ROS levels [340]. In addition Mn²⁺ itself can act directly as an antioxidant, capable of removing superoxide radicals [341]. The transport of Mn²⁺ is important, considering increased levels of Mn²⁺ are neuro-toxic and are implicated in Parkinson's disease like symptoms [342, 343], high levels are also linked to a decrease in GABA concentration in brain through decreasing glutamic acid decarboxylase, an enzyme that controls GABA synthesis [344]. Exposure of cells to 10-800 μM Mn²⁺ in medium leads to cell toxicity [336]. Recent studies have even

linked cell cycle progression, with MnCl_2 exposure causing arrest of cells in G_0/G_1 phase in A549 cells [345], while MnSOD has the capability to induce cell arrest [346].

4.4.1 SPCA2 is the only Ca^{2+} transporting ATPase significantly affected by hypoxia and cell density

SPCA2 is up-regulated in some cancer cell lines, including colon and mammary tumours displaying hypoxic regions [347]. To study the expression of SPCA2 we chose human colorectal carcinoma HCT116 cells: wild type (*WT*), with strong OXPHOS activity and *SCO2*^{-/-} knock-out HCT116 cells [284], deficient in OXPHOS, experiencing strong oxidative stress under normal conditions. Using semi-quantitative reverse transcription polymerase chain reaction (RT-PCR), we analysed expression of various Ca^{2+} -ATPase isoforms in these cells. PMCA and SERCA isoforms showed no changes in expression in HCT116 *WT* or *SCO2*^{-/-} cells when exposed to hypoxic conditions (Fig. 4.16). In contrast, we seen an increase in SPCA2 expression, confirmed by real time q-PCR in *WT* cells exposed to hypoxic conditions, while *SCO2*^{-/-} cells had decreased levels of SPCA2 under similar conditions (Fig. 4.17 A, B). This is most likely linked to these cells experiencing strong oxidative stress in the ambient atmospheric O_2 and may be used for Mn^{2+} transport and scavenging of ROS [284] while under 3% O_2 the *SCO2*^{-/-} cells would experience less ROS production and thus need less SPCA2 activity. In the *WT* cells active OXPHOS in hypoxia can decrease ROS [348, 349], while the increase may be required for the removal of Mn^{2+} no longer required as an antioxidant and for its more efficient intracellular sequestering. Changes in cell density also affected SPCA2, with a threefold increase in SPCA2 expression observed when cells are grown at 100 % density compared to 50 % in wild type cells (Fig. 4.17 C). Thus, density is a separate factor affecting

SPCA2 expression. To see if hypoxia driven up-regulation of SPCA2 can be replicated *in vivo* we analysed colon tissue samples from mice exposed to continuous hypoxia (10 % O₂) [282]. Results showed a two-fold up regulation of SPCA2 when compared to control mice maintained at normal atmospheric O₂ (Fig. 4.17 D). Results conclude that SPCA2 is affected by both environmental O₂, *in vivo* and *in vitro*, and cell density.

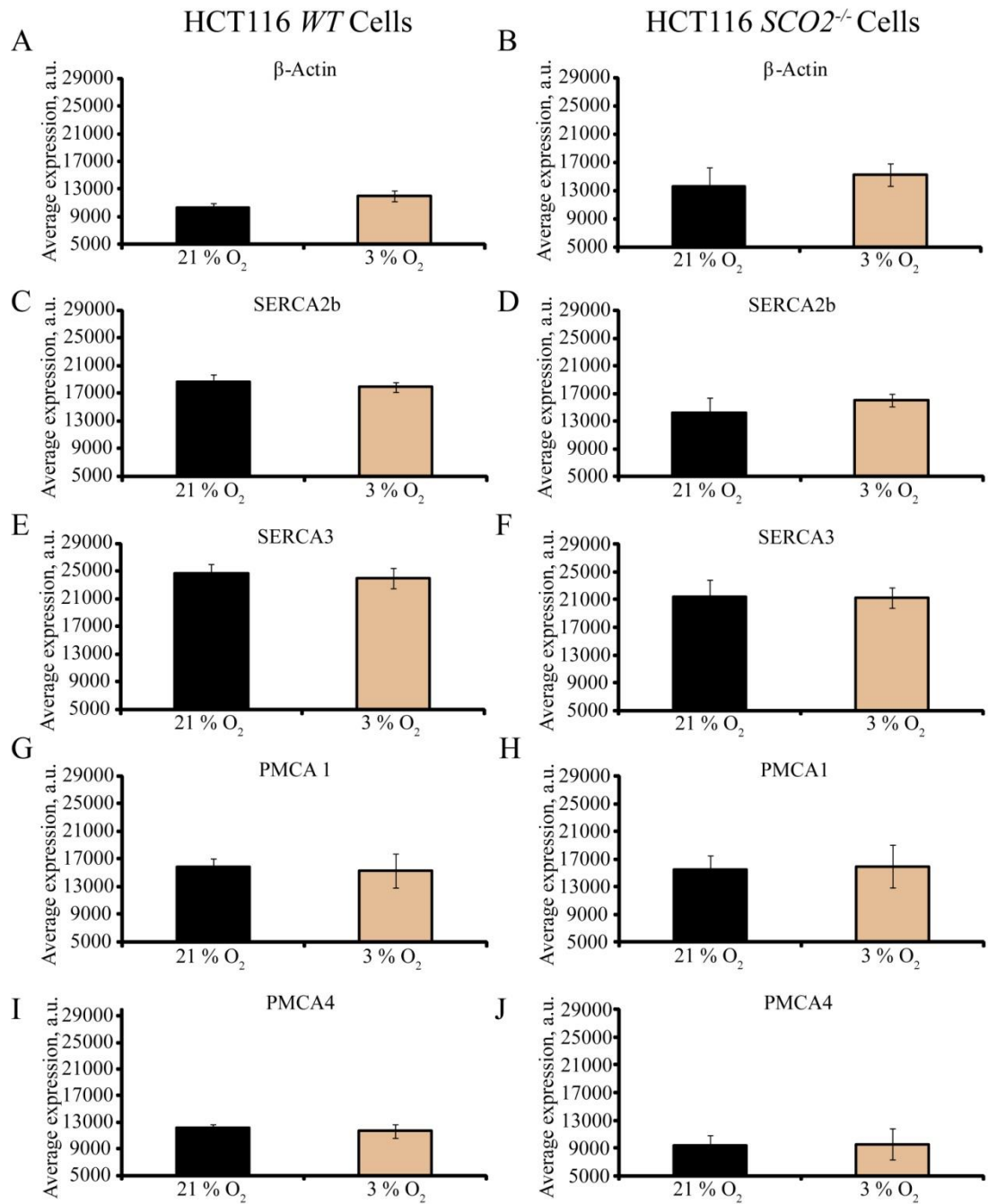


Figure 4.16: Expression of genes encoding β -Actin, SERCA and PMCA isoforms in adherent HCT116 cells (*WT* and *SCO2*^{-/-}) grown under normoxic and hypoxic conditions and analysed using semi-quantitative RT-PCR using 28 (β -Actin and SERCA2b) or 30 cycles (SERCA3, PMCA1 and PMCA4). N=2.

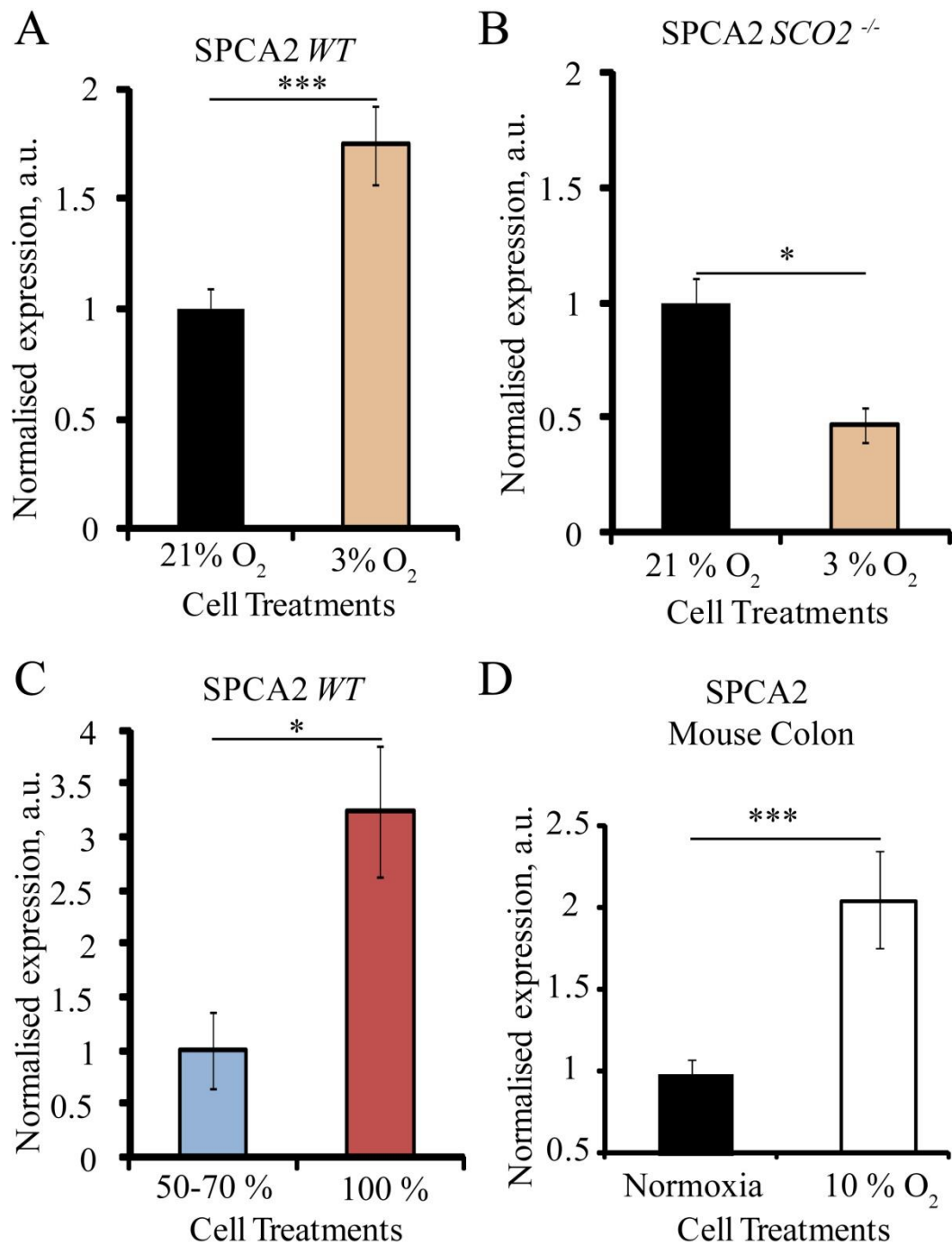


Figure 4.17 Expression of genes encoding SPCA2 in adherent HCT116 cells (Wild-Type, and *SCO2*^{-/-}) grown under different oxygenation conditions and cell density. The average amounts measured via qPCR and normalised to β -actin expression. *Asterisks indicate confidence levels (significant difference) of $P < 0.05$, ** $P < 0.05$. *** $P < 0.001$. N=3.

4.4.2 SPCA2 expression in 3D tumour spheroids

We wished to observe whether our results regarding the effect of O₂ and cell density on SPCA2 expression concurred with monolayer results in a more physiologically relevant cell model. Using the PLIM method [278] we analysed O₂ gradients in spheroids produced using HCT116 *WT* cells. Significant gradients were observed between the periphery and the core. Using the NanO₂ O₂ probe deeper hypoxia was seen when the spheroid size was increased through elevated cell seeding in Lipidure™ plates (Fig. 4.18 A, B). We hypothesised that the O₂ gradients as well as the 3D architecture of the cells in HCT116 spheroids would influence SPCA2 expression. We verified this by using two different sized spheroids with hypoxic cores, followed by extraction of total RNA and analysis by real-time PCR. Interestingly a two-fold up-regulation of SPCA2 expression was seen compared to monolayer cells grown in normoxia (Figure 4.18 C). We noticed that the deeper de-oxygenation and cell-cell interactions affected expression of SPCA2 in the 3D spheroid model.

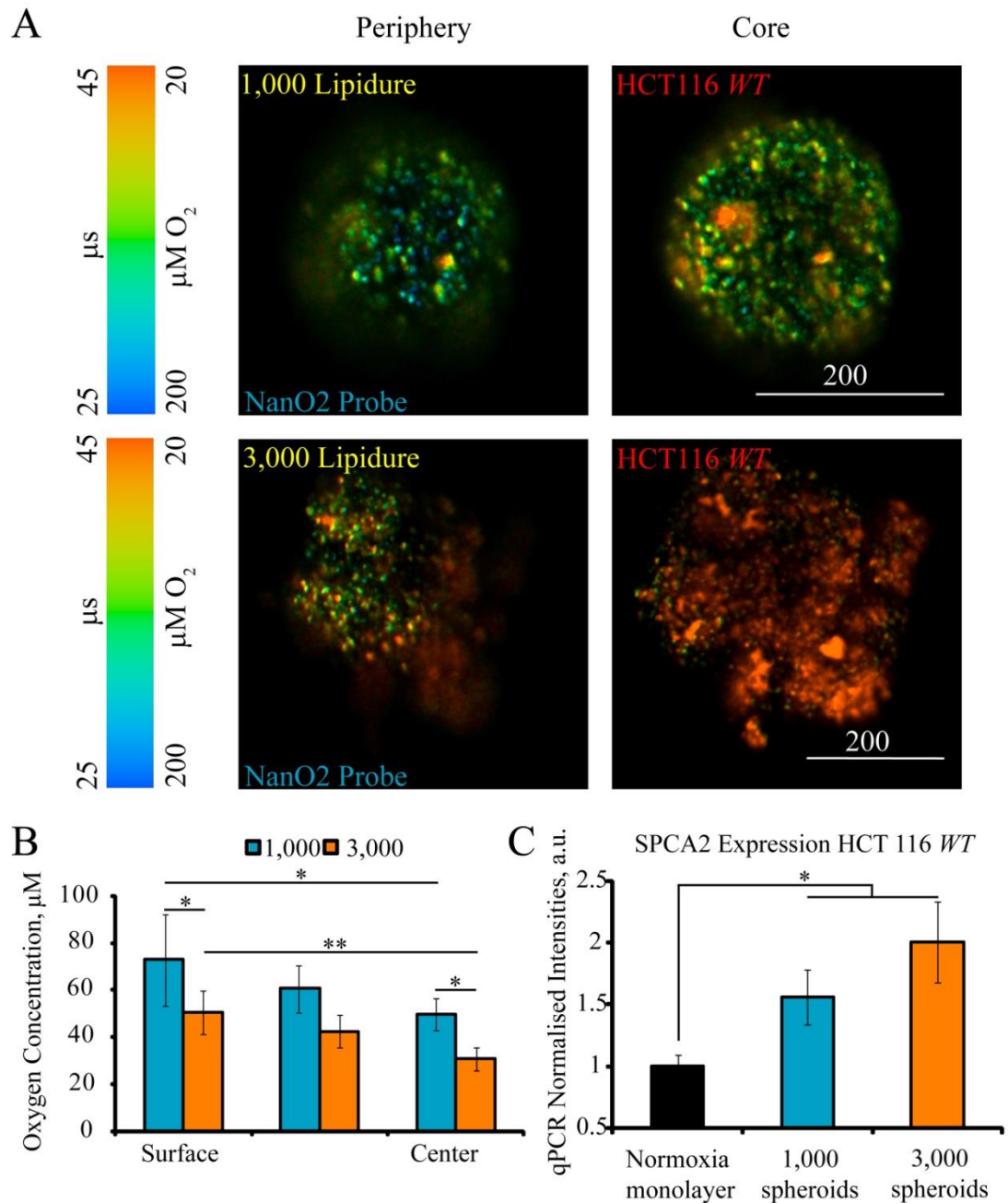


Figure 4.18 Characterisation of HCT116 spheroids produced by LipidureTM. (A) False colour PLIM images of spheroids seeded at 1,000 and 3,000 cells stained with O₂ probe. (B) Mean O₂ concentrations at the spheroid surface and in the core (Depth at which the spheroids diameter is widest, with the core being the area at centre of the spheroid at this depth). (C) Expression of SPCA2 gene in spheroids, seeded at 1,000 and 3,000 in comparison with normoxic adherent cell culture (50-70 % confluence). qPCR data were normalised to β -actin expression. *Asterisks indicate $P < 0.05$, ** $P < 0.005$. Scale bar is in μm . $N = 3$.

4.4.3 SPCA2 expression correlates with MIST1 and is dependent on HIF-1 α

The regulation of SPCA2-encoding gene *ATP2C2* have not been well studied. We wished to look at how hypoxia affects the transcription factor MIST1, previously shown to regulate SPCA2 expression, more specifically a ~20 kDa C-terminal fragment in the salivary gland and pancreatic acinar cells [350, 351]. It functions by forming a homodimer complex activating gene expression, and is located in the nucleus [352]. MIST1 expression was seen to overlap with SPCA2 expression in salivary glands, secreting cells of the stomach, prostate and seminal vesicles. MIST1 expression in HCT116 *WT* cells and *SCO2*^{-/-} cells had similar patterns (Fig. 4.19 A, B). Interestingly, expression of MIST1 increased with cell density, and in the spheroids model (Fig. 4.19 C). The increase of SPCA2 and MIST1 in hypoxia also indicated that the hypoxia-inducible factor (HIF) pathway may regulate it. Following exposure of cells to CoCl_2 (an inhibitor of HIF1 α degradation) and DMOG (prolyl-4-hydroxylase inhibitor/ upregulator of HIF) we seen a 1.5-2 fold increase in both SPCA2 and MIST1 expression (Fig. 4.19 E, F, G, H, I). This indicates that their expression is most likely regulated via HIF-1 α pathway and these genes are its novel downstream targets.

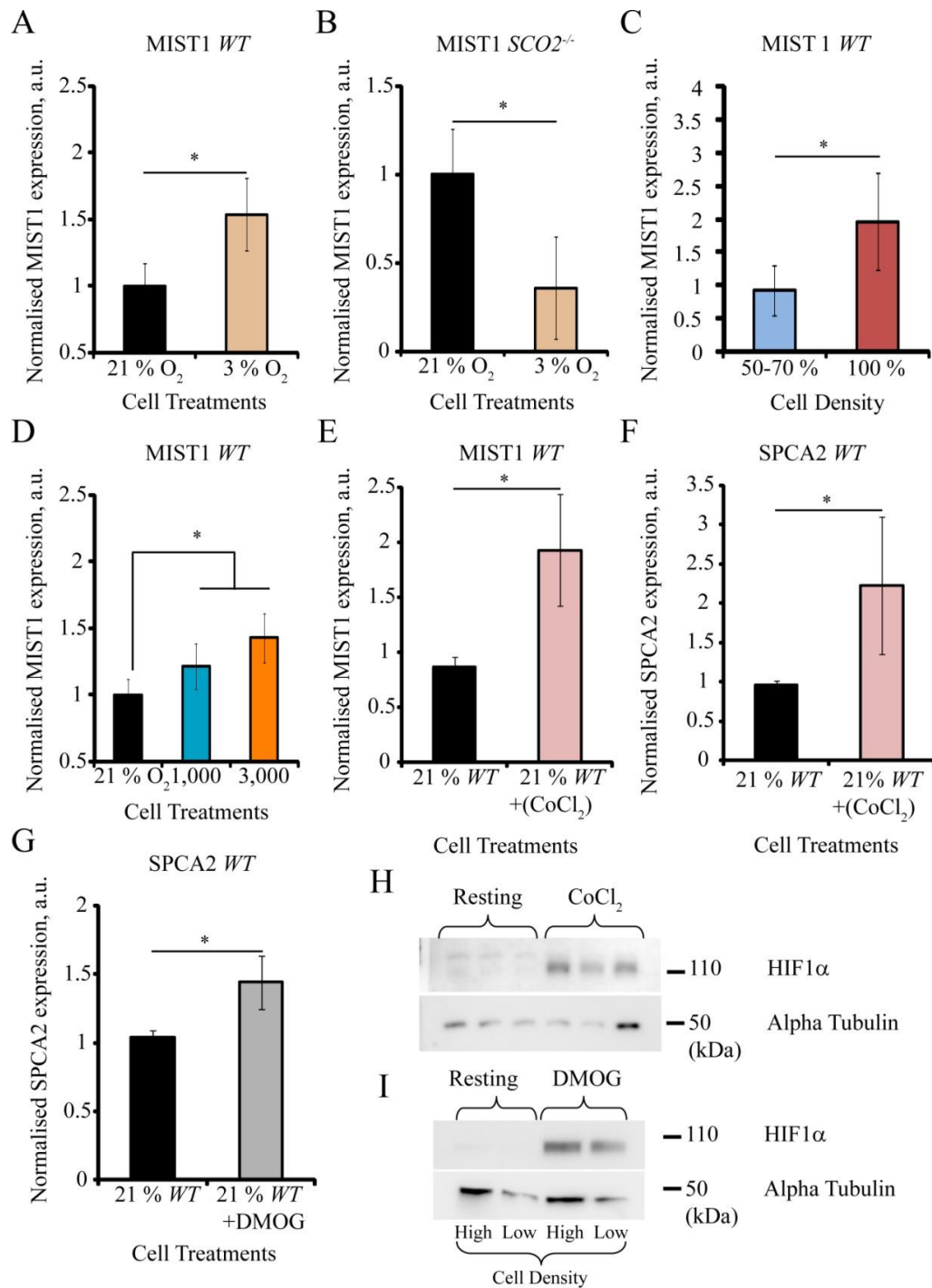


Figure 4.19 Expression of gene encoding MIST1 in monolayer HCT116 (*WT* and *SCO2*^{-/-}) cultures grown under normoxic and hypoxic conditions (A, B), at different cell densities (C) and in spheroids seeded at 1,000 and 3,000 cells (D). MIST1 and SPCA2 gene expression in untreated and CoCl₂ treated HCT116 *WT* cells (E, F). The average qPCR values were normalised to β-actin expression. (G) SPCA2 gene expression in DMOG treated HCT116 *WT* cells. (H, I) HIF1α stabilisation in untreated, CoCl₂ (100 μM, 7 days) and DMOG (1 mM, 2 h) treated HCT116 *WT* cells. *Asterisks indicate P<0.05. N=3.

4.4.4 SPCA2 is involved in regulation of cytosolic Mn²⁺

Both Ca²⁺ and Mn²⁺ transport is linked through their shared use of secretory pathway Ca(2+)-ATPases (SPCA) transporters [353, 354]. Thus, we had a look at the correlation between both Ca²⁺ and Mn²⁺ with O₂. Ca²⁺ is an important second messenger, involved in the signal transduction process required for cell growth, differentiation, proliferation and apoptosis. Prolonged exposure to elevated Ca²⁺ can lead to proliferation and tumour growth [355]. Using the Oregon green BAPTA-1 (OGB) probe it was possible to produce a calibration of Ca²⁺ concentrations versus lifetime values of the probe in FLIM mode.

Applying the OGB probe and multiplexing it with the NanO₂ phosphorescent probe it was possible to correlate O₂ and Ca²⁺ concentrations. Results showed that as O₂ increased Ca²⁺ levels decreased (Fig. 4.20). In the core of the spheroids previously seen to be more hypoxic than the periphery there was an increase in Ca²⁺ concentration (Fig. 4.20 B). A possible explanation for this based on previously shown data is that in hypoxia both extracellular and intracellular pH decreases leading to an influx of Ca²⁺ [356]. The increase in SPCA2 may be as a result of the need for increased Ca²⁺ within the core of the spheroids which has a more acidic pH than the periphery [357]. When comparing HCT116 *SCO2*^{-/-} and *WT* spheroids we see no significant changes in Ca²⁺ concentrations in regions of similar O₂ levels (Fig. 4.20 C, D, E, F). In contrast to *WT* spheroids there are no Ca²⁺ gradients in the HCT *SCO2*^{-/-} spheroids between the periphery and the core (Fig. 4.20 B). However similarly there were no O₂ gradients seen when measuring similar sized *SCO2*^{-/-}-spheroids using the NanO₂ probe, a stark contrast to gradients seen in HCT116 *WT* (Fig. 4.18 A, B). From the above results we show there is little or no difference in Ca²⁺ concentration between *WT* and *SCO2*^{-/-} spheroids. However, there are significant differences in SPCA2 expression between

the two cell lines. This would indicate that the increased SPCA2 a $\text{Ca}^{2+}/\text{Mn}^{2+}$ transporter in *WT* cells in hypoxia is having little effect on Ca^{2+} transport but is as previously hypothesised involves primarily in the transport of Mn^{2+} .

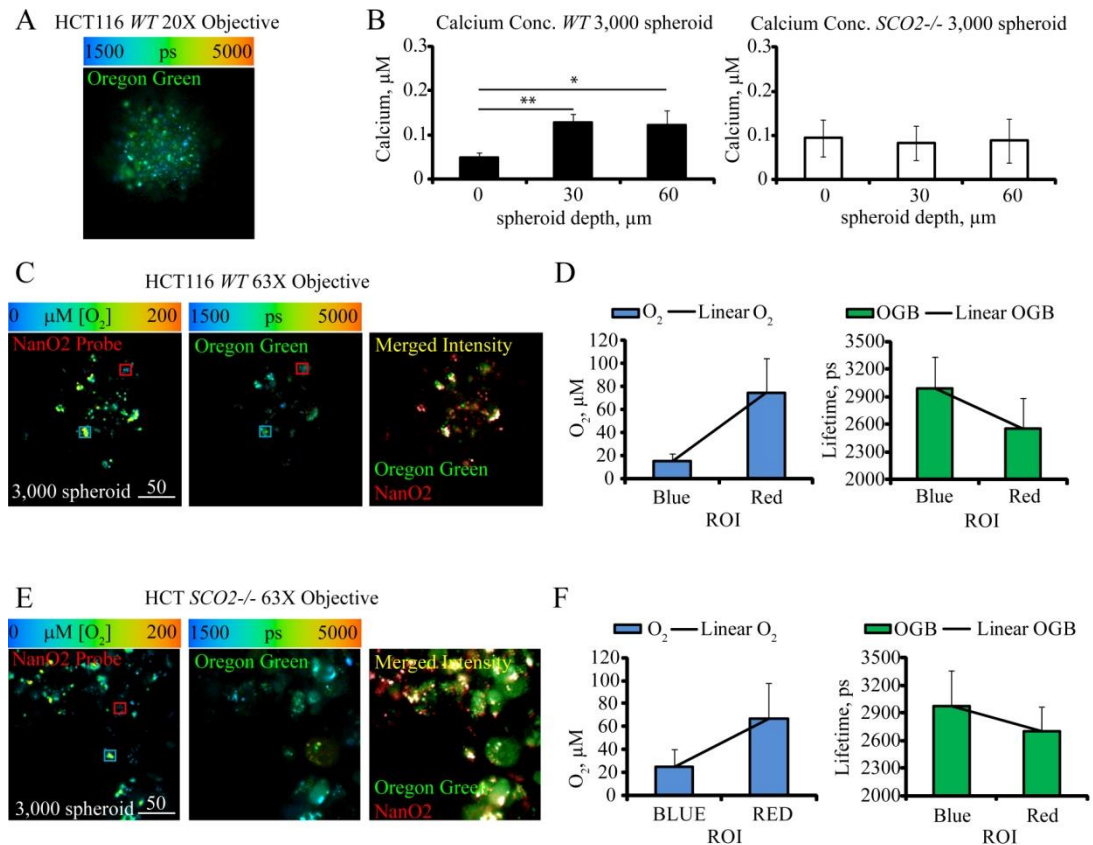


Figure 4.20: Measuring intracellular Ca^{2+} levels in HCT cells. (A) Spheroid stained with Oregon green BAPTA-1 (OGB), 20X objective. (B) Ca^{2+} concentration in HCT116 *WT* and *SCO2*^{-/-} spheroids. (C, D) OGB staining in HCT116 *WT* spheroid, 63X objective, with corresponding graphs showing O_2 and Ca^{2+} concentration for the blue and red ROI. (E, F) OGB staining in HCT116 *SCO2*^{-/-} spheroid, 63X objective, with corresponding graphs showing O_2 and Ca^{2+} concentration for the blue and red ROI. N=3.

Since SPCA2 showed the most dramatic change, and as a result of its role in the regulation of intracellular Mn^{2+} [337] it was necessary to look at the effect of cells

over expressing SPCA2 on Mn^{2+} . Mn^{2+} -dependent activity of SPCA2 was demonstrated before, however we wanted to confirm if it regulated Mn^{2+} in cultured HCT116 cells. To do this we used the fluorescent biosensor constructs based on the GPP130 protein, allowing detection of increase of cytosolic Mn^{2+} in live cells [290]. Increased Mn^{2+} leads to translocation of GPP130-GFP to lysosomes for degradation (Figure 4.21).

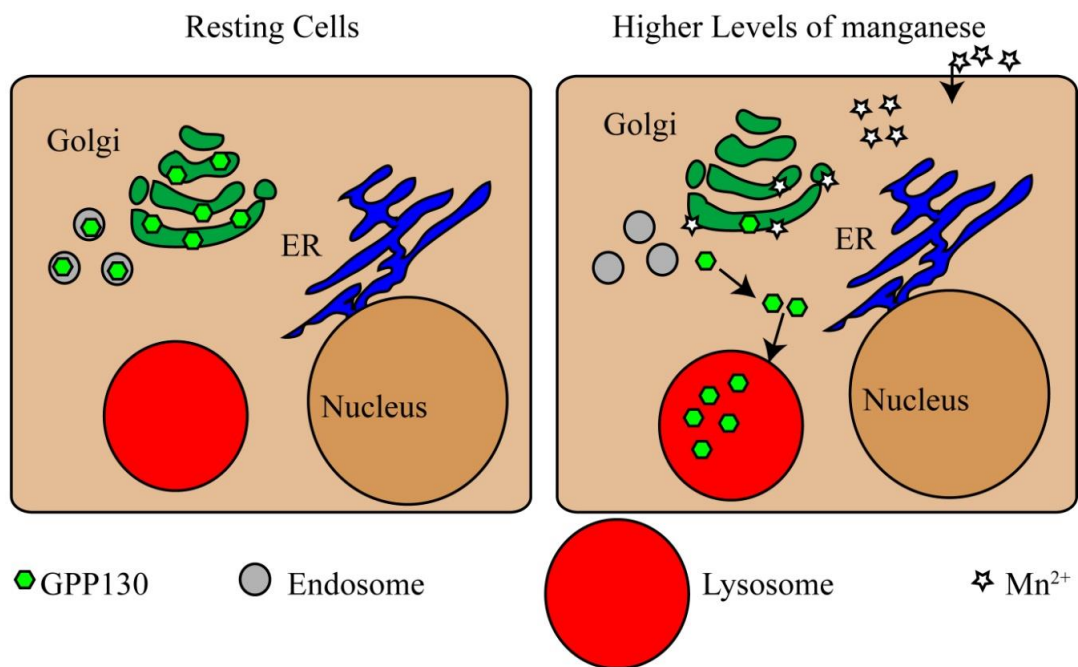


Figure 4.21 Schematic displaying the method of action of the GPP130 probe.

We transfected cells with plasmid DNA expressing full-length SPCA2 and SERCA2b (Fig. 4.22) both with and without the addition of external Mn^{2+} , and quantifying regions of interest for GPP130-GFP co-localised with lysosome marker LysoTracker Red (Figure 4.23). The addition of Mn^{2+} alone did not lead to statistically significant change in lysosomal translocation of GPP130, whereas overexpression of SPCA2

showed its decrease. By combining SPCA2/ Mn^{2+} , a decrease in lysosomal translocation occurred.

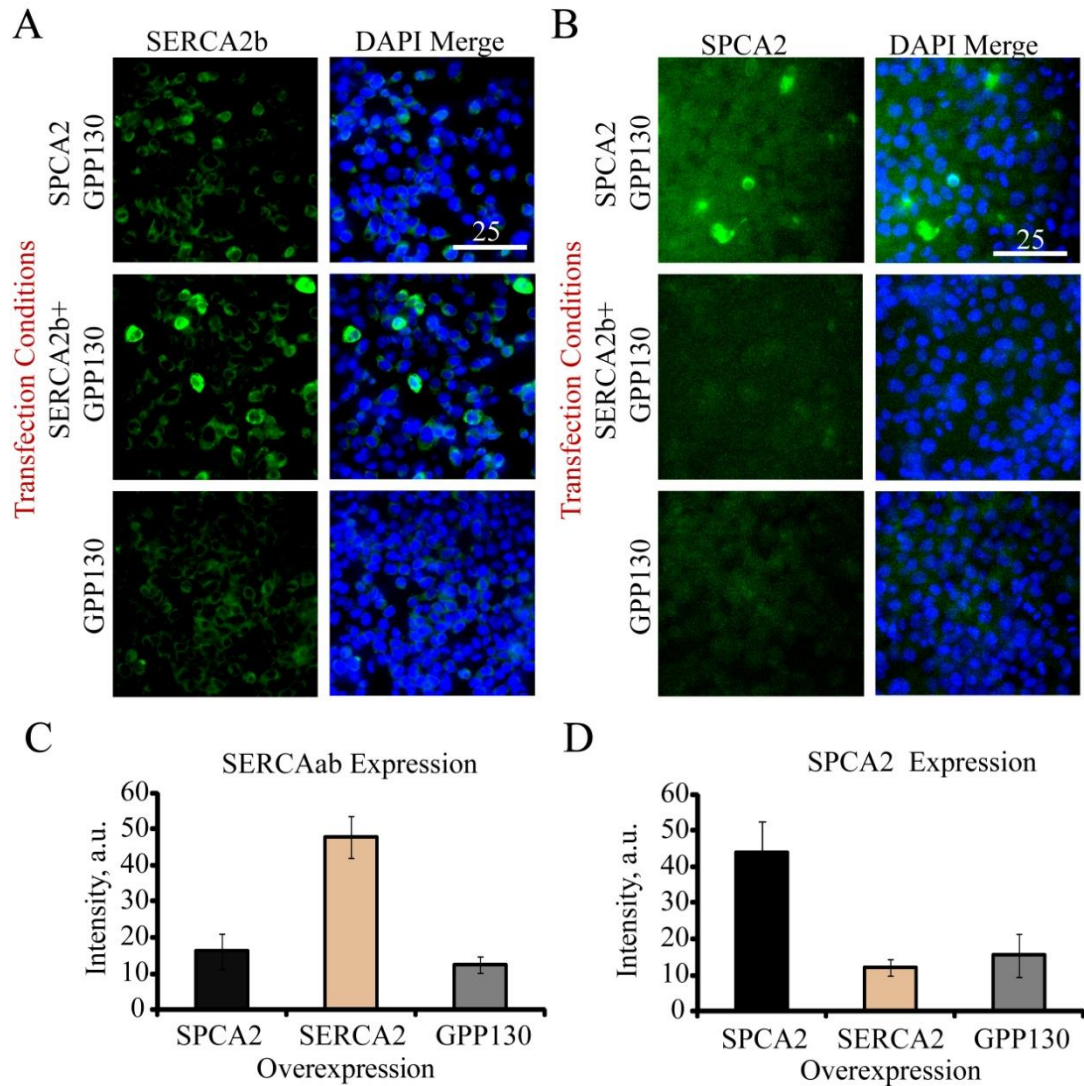


Figure 4.22: Confirmation of over-expression of SPCA2 and SERCA2b in cultured HCT116 cells. Transfected cells were fixed and immunostained with the antibodies. Alexa Fluor-594 conjugated secondary antibodies were used to ensure no signal overlap with the GFP-fluorescent GPP130 protein. Antibody staining is shown in green, nuclei are shown in blue. Scale bar is in μm .

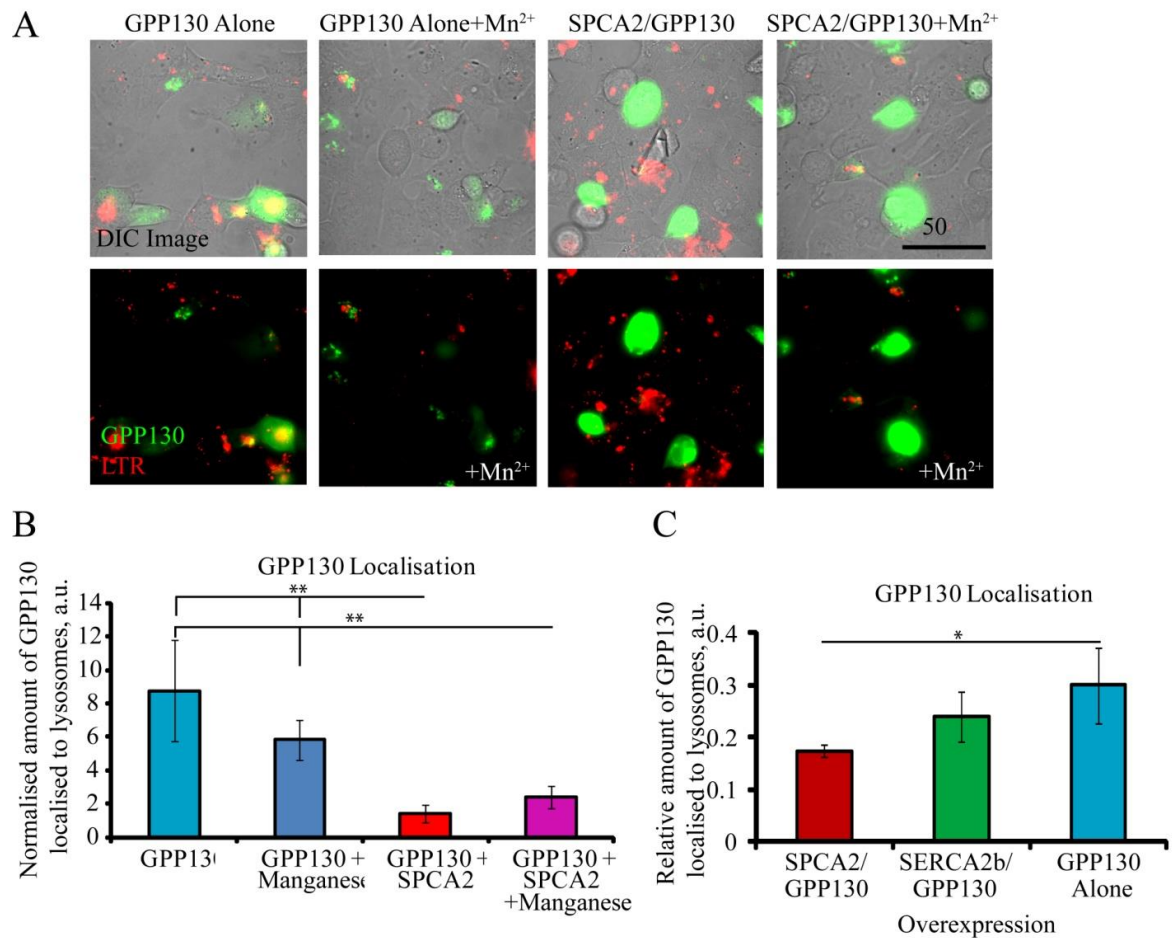


Figure 4.23 SPCA2 overexpression decreases cytosolic Mn^{2+} and increases ROS production. (A) Transmission light and fluorescent image showing HCT116 WT cells transfected as indicated and co-stained with LysoTracker Red. Co-localisation of GPP130 (Green) with lysosomes (Red) positively correlates with Mn^{2+} levels. (B, C) Results of quantification of translocation of GPP130-GFP in lysosomes, under different conditions shown above. *Asterisks indicate confidence levels (significant difference) of $P < 0.05$, ** $P < 0.005$. Scale bar is in μm . $N = 5$.

4.4.5 SPCA2 is involved in the regulation of Mn^{2+} -dependent cell cycle progression

The increase of SPCA2 with cell density hinted at the link between its function and progression of cell cycle. To test this, we looked at the differences in proliferation in cell cultures exposed to hypoxia (3% O_2). BrdU staining showed twice the number of cells entering S phase during hypoxia when compared to normoxic conditions (Fig.

4.24 A, B). This data correlates with increased SPCA2 in hypoxia and its involvement in Mn^{2+} transport. It was previously shown that Mn^{2+} can arrest the cell cycle in G0/G1 and S phase [345]. We confirmed this using transfected cells with SPCA2 and SERCA2b (control), treated with high $MnCl_2$ in the media, comparing number of cells in S phase (Fig. 4.24 C). There was significantly lower cell proliferation in non-transfected cells, however an increase in the SPCA2-transfected cells (both treated and non-treated samples) (Fig. 4.24 C, D). This data confirms that transport of cytosolic Mn^{2+} by SPCA2 prevents cell cycle arrest by this ion. The exact mechanism for SPCA2-mediated transport is unclear but should involve sequestering the Mn^{2+} from cytoplasm to Golgi or other compartments and thus decreasing its inhibitory effect on cell proliferation. However, such an effect highlights a role in SPCA2 for colon cancer cells in their adaptation to hypoxia, preventing cell death, increasing proliferation and promoting tumour growth.

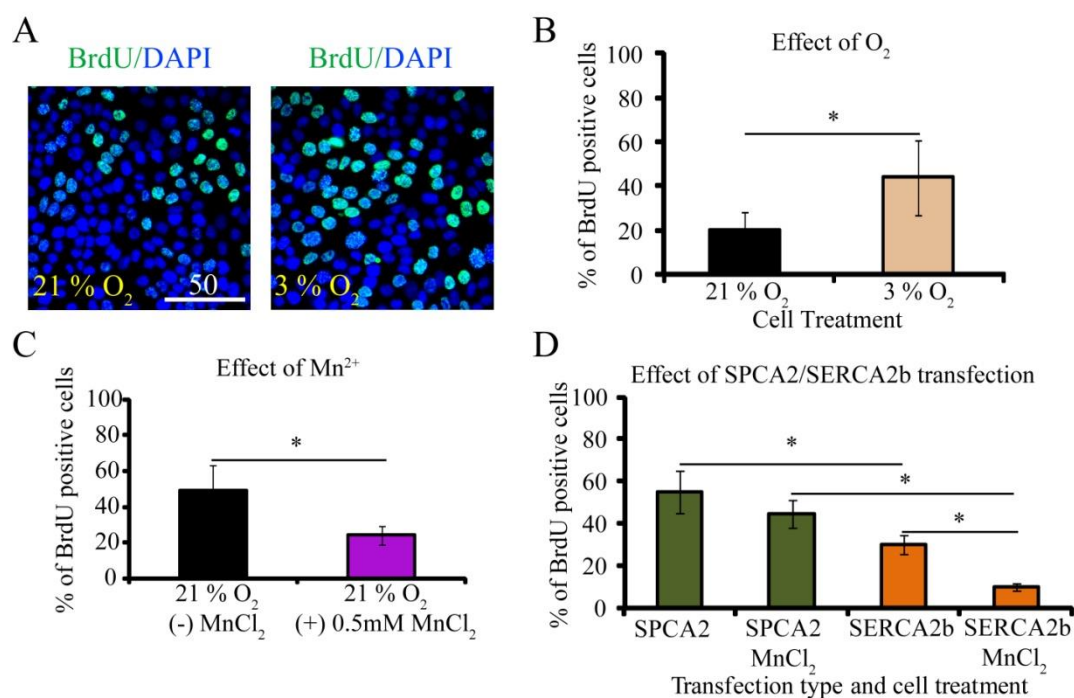


Figure 4.24 SPCA2 restores cell cycle arrest induced by Mn²⁺. (A, B) Effect of hypoxia on percentage of S-phase-positive cells, revealed with BrdU immunofluorescence staining. Cells were exposed to hypoxia, pulsed with BrdU (100 μ M, 30 min), and immunostained with anti-BrdU antibody (green). DAPI staining (blue) shows nuclei. Scale bar is in μ m. (C) Effect of Mn²⁺ treated and untreated HCT116 WT cells on S phase positive cells at 21 % O₂. D: Effect of exposure to Mn²⁺ (0.5 mM, 24 h) on the number of S phase-positive cells in non-transfected and SPCA2/SERCA2b- transfected HCT116 cells at ambient (21 %) O₂. "taken with modifications from [317]". N=3.

In this study, we made several novel discoveries, including the fact SPCA2 expression in HCT116 WT cells is dependent upon cell density and de-oxygenation. We were further able to correlate SPCA2 up-regulation with the expression of the transcription factor MIST1 and with HIF1 α . Evidence indicates that SPCA2 is crucial for Mn²⁺ transport from the cytosol. This is of interest when we consider that SPCA2 plays a direct role in the proliferation capacity of HCT116 WT cells, possibly through minimising the exposure of the cells to high cytosolic Mn²⁺.

5. General Discussion

We first introduced a novel approach for measuring changes in extracellular O₂ in 3D cell and tissue cultures, using phosphorescent O₂-sensitive scaffolds coupled with confocal microscopy. These hybrid scaffolds proved to be non-invasive, easy to manufacture, could retain the cell culturing abilities of the original material, don't require the addition of foreign substances into the cells and produce high fluorescent signals. Most importantly for our studies they showed the required sensitivity for O₂ in the physiological range (0-21 % atmospheric O₂ or 0-200 μM dissolved O₂). This protocol can act as a template for future developments, as the success of our particular scaffold could be reproduced, using scaffolds made from other materials, containing other O₂ indicators, including metalloporphyrins [120], providing high sensitivity in lower O₂ values, infra-red shifted or two-photon excitable using this method. Much like planar O₂ sensitive coatings [358] our hybrid scaffolds allowed for the monitoring of local O₂ levels, displaying similar results to previous work, were local micro gradients formed because of the highly respiring cells [359]. Using PC12 aggregates with approximately 10-50 respiring cells, the gradients in O₂ that we observed were expected [283]. To analyse rapid (1-5 minute) changes in metabolic activity, we stimulated PC12 aggregates with protonophore FCCP (uncoupler that activates respiration) and AntA (mitochondrial inhibitor) [297]. Strongest effects of cell respiration on O₂ measured by the scaffold were near metabolically active cells. It is known that low levels of O₂ lead to PC12 cell differentiation *in vitro*. Showing similar results to previous work carried out in PC12 cells, our scaffolds were used to monitor the increase in transcription of the tyrosine hydroxylase gene and stability of TH mRNA in hypoxia [307]. However in contrast to work completed by (O'Driscoll *et al*, 2005) [306] no neuritis was seen in the PC12 cells in any regions of the scaffold

regardless of O₂, explained by different cell morphology in 3D culture, with our scaffolds proving to be a useful tool in studying this process via imaging. Hypoxia is a common characteristic in tumours, as such drugs are being developed that act specifically under such conditions [323]. One mechanism of action involving these pro-drugs not active in normoxia, is their accumulation in hypoxia where they are reduced by cellular reductases producing toxic free radicals [324]. Tirapazamine functions by preventing DNA repair in hypoxic conditions [325] and was previously used to study its effects in A549 cells under hypoxic conditions [326]. We studied TPZ action at different oxygen levels, as a result of the naturally forming gradients in both our scaffolds and in 3D spheroids. In both models, results confirmed that TPZ was more active in regions of greater hypoxia within our cancer cells, displaying significantly higher cell death, while our O₂ scaffolds and intracellular probe could inform on changes in O₂ associated with cell respiration rate and viability. These scaffolds carry out a similar role to fibre optic probes and planar O₂ sensors [227]. However, the microporous scaffold we produced had its advantages including, compatibility with confocal microscopy allowing for high resolution 3D mapping of O₂ distribution, rather than simply point or 2D measurements. This method also allows for O₂ detection to be easily multiplexed with other fluorescent probes and markers of cellular function widely used in live cell imaging and immunostaining.

In contrast to our oxygen sensitive scaffolds our novel O₂ sensitive conjugated polymer nanoparticles can measure intracellular O₂, entering cells via endocytosis. They have a size of approximately 50 nm, similar to previous O₂ nanoparticles produced [250]. Furthermore these probes are compatible with one- and two-photon excitation as well as both ratiometric (intensity) and lifetime based imaging modes [136]. Measuring our probes spectra showed that it has a green residual emission from

poly(fluorene-alt-benzothiadiazole) and NIR emission from Pt(II)-benzoporphyrin. The use of probes emitting longer red and infra-red-shifted aids in deeper light penetration and as a result the ability to measure larger cell based 3D models in excess of 150-200 μm [135]. Our nanoparticle efficiently stained monolayer HCT116 cells after incubating in the media for 16 h, localising to the endosomes and lysosomes, similar to previously described probes like MM2 and PA2 [360, 361]. It showed sufficient sensitivity to O_2 , capable of measuring across the physiological range (0-200 μM O_2). The toxicity of nanoparticles was evaluated by loading of our HCT116 cells with nanoparticles for 17 h at different concentrations, analysing total cellular ATP and extracellular acidification [309]. Only minor toxicity was observed when concentrations of greater than 20 $\mu\text{g}/\text{ml}$ were used, ensuring that at our working concentration of 1-5 $\mu\text{g}/\text{ml}$ was compatible with live cell imaging. Compared to previous probes our new conjugated nanoparticle showed higher brightness, improved ratiometric responses and an ability to be easily modified as a result of their chemical makeup.

We also characterised a newly designed T probe, produced using a sulforhodamine dye in a cationic RL100 nanoparticle, and show how it is useful in the quantitative T imaging in cell and tissue models using FLIM. Rhodamine derived dyes have high brightness with fluorescence in the orange-red spectral range (550-700 nm) and robust sensitivity to temperature in both intensity and lifetime imaging modes [362, 363]. Comparable to previous dyes embedded in polymeric or silica nanoparticles, which prevented dye interference from external species [191], the encapsulation of the dye inside the polymer ensured that environmental stimuli like pH, serum proteins or ionic strength had little to no effect on the probe, while retaining its sensitivity to temperature in fluorescent lifetime. Furthermore it showed a decrease in fluorescent

lifetime of ~0.6ns between 25-40 °C, a range which can be reliably resolved on modern TCSPC-FLIM microscopes [116, 173]. The probe ensured efficient staining of HCT116 cells in both monolayer culture and in 3D following addition to growth media. The staining and intracellular localisation was comparable to another RL100-based O₂-sensitive NanO₂ probe [364], but with greater diffused cytoplasmic staining, possible due to the smaller size of the probe (~10nm). This diffused staining was a benefit when monitoring temperatures in single cells. The chemical structure of the sulforhodamine is very like that of SR101 [365], indicating that the T probe is compatible with two-photon FLIM. Using 2D monolayer cell culturing with our T probe we seen that there was an almost homogenous distribution of temperature across the cytoplasm. Previous work has shown that gradients in temperatures between the nucleus and cytoplasm may exist [192], in contrast to our results in monolayer cells. However these gradients between the cytoplasm, nucleus have been disputed, due to the cells inability to generate such amounts of heat as well as taking into account heat dissipation rates [189, 316]. When the probe was added to 3D spheroid cultures heterogenous temperatures were measured, with gradients changing depending on size and metabolic activity. The spectral and decay characteristics allowed for it to be multiplexed with our phosphorescent, intracellular, O₂ sensitive nanoparticles. Similar heterogeneity was seen with O₂ levels. O₂ gradients while negligible in individual cells, are observed in aggregates and spheroids which reach sizes of greater than 50µm [327, 366]. While O₂ gradients have been described in relation to spheroids previously [278, 283] this was the first time temperature gradients were demonstrated. Previous work investigated whether gradients existed in spheroids formed using HeLa cells [367], however none were detected, probably as a result of the small size of the HeLa spheroids coupled with the fact the cells are highly glycolytic with a low metabolic

activity. Our results highlighted the interdependence of temperature and O₂ gradients in tumour spheroids, with both being effected by the surrounding microenvironment as well as the cells metabolic state. We found that the temperature of the spheroid never exceeded ~41/42 °C, explained by the adaption of cells to heat produced via their metabolic activity, decreasing their heat production and activating their heat shock pathway. In cancer cells, they must adapt to ensure excess heat isn't produced, leading to heat shock and cell death. The increase in O₂ levels measured in the spheroids core when exposed to temperatures of 40 °C, may be as a result of reduced consumption and faster diffusion of O₂ and the change in utilising of energy production pathways, switching from OxPhos to glycolysis [223]. The decrease in O₂ may also be as a result of decreased cell viability under such high temperatures. The increase in O₂ was in contrast to the results observed for the temperature dependence of O₂ in the aqueous phase, differences that are accounted for by cell metabolic activity and viability [368]. To investigate whether gradients were caused by spheroids formation we treated the spheroids with cantharidin [369], decreasing the cell-cell interaction causing disaggregation. When they disassembled the O₂ levels increased and the temperatures approach ambient levels. We also investigated the effects of metabolic stimulation in both HCT116 *WT* and *SCO2*^{-/-} cells deficient in oxidative phosphorylation [284], treating cells with FCCP (uncoupler, activates cell respiration) and oligomycin (inhibits ATP synthase) achieving maximal mitochondrial uncoupling [223]. In *WT* spheroids there was a significant increase in deoxygenation as a result of O₂ consumption [283], with a concomitantly increase in spheroid temperatures. In contrast non-respiring *SCO2*^{-/-} cells showed no changes in O₂ or temperature. The *SCO2*^{-/-} cells also showed higher O₂ levels and near ambient temperature in the core linking temperature and O₂ gradients in spheroids to oxidative phosphorylation . In

conclusion tumour spheroids were used successfully to observe the dynamics of O₂ and temperature, dependent on structural integrity, spheroid size, viability and mitochondrial activity.

Our O₂ probes proved to be useful in a mechanistic study involving the Ca²⁺/Mn²⁺ - transporting SPCA2 pump. We discovered that SPCA2 expression in HCT116 cells is dependent upon both cell density and cell deoxygenation. This was in line with previous work which also showed increased expression in a number of colon and mammary tumour cell lines [347]. Furthermore, rapidly proliferating cancer cells have also been identified in deoxygenated regions [370]. For our study we chose 3% O₂ as hypoxia, a realistic concentration of O₂ to mimic the conditions of the intestine in vivo [371], with colon tissues and tumours in vivo displaying heterogeneous O₂ levels ranging from 0 to 5 % [255, 256]. We wished to compare SPCA2 expression in 2D monolayer culture with a more physiologically relevant spheroid model, displaying gradients in O₂ and other nutrients. Due to the fact the different methods of spheroid formation affect size, metabolic activity and viability [320], we first optimised and compared methods of spheroid formation using “free floating culture”, Lipidure™, and “hanging drop” [54]. We aimed to find the spheroid production method with the most uniform size, viability, with physiologically relevant O₂ gradients as well as being easy to culture. The Lipidure™ method proved to be the most uniform, with comparable viability, proliferation capacity size and shape noted between individual spheroids. It also the easiest method of formation in terms of ease of handling. Spheroids produced using HCT116 cells and our chosen formation method showed deep deoxygenation after 3days as a result of active mitochondrial respiration similar to previously published work [324]. Using our intracellular nanoparticle probes we could link hypoxia within spheroids with an increase in

SPCA2 expression. We observed an SPCA2 increase in 3D spheroids comparable to cells grown in 2D at 3% O₂. In order to identify what was regulating SPCA2 in HCT116 cells we next analysed MIST1 a transcription factor of the B family of basic helix-loop-helix (bHLH), previously shown to regulate SPCA2 expression [350]. Because SPCA2 expression increased under hypoxia it may also be regulated by the hypoxia-inducible factor (HIF) pathway. To examine this we added well known inhibitors of HIF-1 α degradation, cobalt chloride and dimethylxalylglycine (DMOG) [370] to the cells, and looked at SPCA2 and MIST1 expression. Both drugs increased expression of both SPCA2 and MIST1 nearly 1.5-2-fold indicating they are likely regulated by the HIF-1 α pathway. Considering SPCA2 is a transporter of both Ca²⁺ and Mn²⁺ we looked at whether changes in expression led to differences in these ions. The lack of any significant differences in intracellular Ca²⁺ between HCT116 *WT* and *SCO2*^{-/-}, cell types with significant differences in SPCA2 expression, led us to believe the role of SPCA2 in hypoxia was primarily related to manganese transport. Our studies into the role of SPCA2 in manganese transport from the cytosol to the golgi are in line with previous work involving the ion transporting properties of this enzyme [334, 347]. Using the fluorescent biosensor GPP130-GFP we could link SPCA2 with the transport of Mn²⁺ from the cytosol of the cell to the golgi and other secretory vesicles. The effect cell density on SPCA2 expression indicated a possible link between the function of this pump and cell cycle progression. Previous work has already shown that manganese has the ability to affect cell cycle progression via MnSOD [372], decreasing cell proliferation. Our experiments using cells overexpressing either SPCA2 or SERCA2b (control), elucidated the role of SPCA2 in transport of manganese out of the cytosol, preventing cell cycle arrest by this ion. The exact mechanism isn't known; however, it shows the role of SPCA2 in colon cancer

cells. For their adaption to hypoxia, preventing cell death and promoting tumour growth.

6. Overall conclusion

Sensing of physiological parameters of the cell and tissue models is of critical importance for various applications, analytical platforms and disease models. This thesis presents several new sensor and probe systems capable of measuring O₂ and temperature in fluorescence imaging mode, particularly PLIM and FLIM, and displaying their uses in various applications.

The development of a new hybrid, multi-functional tissue scaffold system produced by staining commercial porous polystyrene membrane scaffolds, Alvetex™ with the phosphorescent dye PtTFPP using the swelling method enabled us to measure oxygenation of HCT116 and PC12 grown on such scaffolds. We can also monitor the effects of drug stimulation, including inhibitors and stimulators of respiration, imaging the dynamic changes in extracellular O₂. Furthermore, O₂ levels can be linked or correlated with changes in gene expression in the seeded cells and aggregates, a process easily monitored via confocal FLIM-PLIM imaging paired with immunostaining.

The novel cell-penetrating O₂ and temperature-sensitive nanoparticle probes we designed and evaluated for imaging in 3D tissue models. They are capable of efficient staining of various types of mammalian cells, with no adverse effects on cell viability and function. Excellent probe photostability, brightness, stable calibrations and responses to their respective analytes and changing environmental conditions were obtained. The nanoparticle probes were also able to penetrate and measure gradients in our *in vitro* 3D tumour spheroid models (some greater than 500 µm diameter), dimensions well above the limits of light microscopy.

Imaging approach was applied for detailed analysis and comparison of three commonly used spheroid formation methods, "free floating", "hanging drop" and "LipidureTM". Our spheroid model was optimised to ensure uniformity in size and shape in a more physiologically relevant model, displaying natural gradients in O₂ and temperature, proliferating and dying cells and active mitochondria. Using viability probes and proliferation dyes multiplexed with our O₂ probe, we could identify the formation method which produced the most viable spheroid.

Combining the sensors and probes with our tissue models, such as scaffolds, cell aggregates and tumour spheroids, we could monitor drug effects on cells within a 3D microenvironment in two different models, proving they may have a use in future drug toxicity studies. The potency of the anti-cancer drug tirapazamine was apparent in the more hypoxic regions of both our 3D scaffold model and tumour spheroids. Furthermore, we could monitor in real time the concentration and dynamic changes in O₂ within spheroids following adaption to external stimuli. The ability to carry out live cell fluorescence imaging to monitor the dynamics of O₂ and temperature, particularly by multiplexed PLIM/FLIM method, will further our knowledge of the 3D microenvironment in cell and tissue function. The probes were used in a mechanistic study (function of Ca/Mn-transporting SPCA2 protein), monitoring changes in gene expression in response to O₂ changes. The importance of monitoring and knowing O₂ concentration was apparent in the up regulation of SPCA2 because of O₂ and cell density. The link between hypoxia and changes in O₂ regulation led us to discover the role SPCA2 plays in the cell cycle, preventing cell arrest through the regulation of cellular Mn²⁺.

In summary, we have developed new techniques and evaluated new probes which can be used for high-resolution live imaging detection of O₂, temperature and other

important physiological parameters of cell and tissue models. They have proven to be instrumental in the improvement of our understanding of the 3D microenvironment, gene expression and drug effects in cell and tissue function as well as being indispensable in viability studies via live cell microscopy imaging.

7. Thesis outcome

Peer reviewed papers:

Jenkins J, Borisov SM, Papkovsky DB, Dmitriev RI. Sulforhodamine nanothermometer for multi-parametric FLIM imaging. *Analytical Chemistry*. Manuscript submitted. (Chapter 3 and 4)

Jenkins J, Papkovsky DB, Dmitriev RI. The $\text{Ca}^{2+}/\text{Mn}^{2+}$ -transporting SPCA2 pump is regulated by oxygen and cell density in colon cancer cells. *Biochemical Journal* 473, no. 16 2016: 2507-18. (Chapter 4)

Fomin M, Dmitriev RI, **Jenkins J**, Papkovsky DB, Heindl D, König B. A Two-Acceptor Cyanine-Based Fluorescent Indicator for NAD(P)H in Tumor Cell Models. *ACS Sensors*, 2016: p702-709.

Jenkins J, Dmitriev RI, Morten K, McDermott KW, Papkovsky DB. Oxygen-sensing scaffolds for 3-dimensional cell and tissue culture. *Acta Biomater*. 2015;16:126-35. (Chapter 3 and 4)

Book Chapter:

Jenkins J, Dmitriev RI, Papkovsky DB. Imaging Cell and Tissue O_2 by TCSPC-PLIM. In: Advanced Time-Correlated Single Photon Counting Applications. Ed. W. Becker, Springer International Publishing; 2015. p. 225-47.

Published conference proceedings:

Dmitriev RI, **Jenkins J**, Okkelman IA, Papkovsky DB. Multi-parametric imaging of oxygen in scaffold-free and scaffold-based three-dimensional tissue models. European Cells and Materials 2016; p245: Vol. 31. Suppl. 1. (Chapter 3 and 4)

Jenkins J, Dmitriev R, Papkovsky D. The Secretory Pathway Ca²⁺/Mn²⁺-ATPase SPCA2 Regulates Mn²⁺-Dependent Cell Cycle Progression in 3D Culture of Colon Cancer Cells. Biophysical Journal 2016;110:336a. (Chapter 4)

Jenkins J. Local O₂ Gradients in Porous 3D Scaffold Monitored by Phosphorescent Lifetime Imaging Microscopy. Biophysical Journal 2015;108:484a. (Chapter 3)

Dmitriev RI, Borisov SM, **Jenkins J**, Papkovsky DB. Multi-parametric imaging of tumor spheroids with ultra-bright and tunable nanoparticle O₂ probes. *SPIE Proc.*, 2015, p. 932806-932808. (Chapter 4)

Conference presentations:

Oral presentation: "Luminescence lifetime imaging microscopy of temperature and O₂ gradients in 3D tumour cell model". Microscopy Society of Ireland, 40th Annual Meeting. Dublin Institute of Technology, Dublin, Ireland. 8th-10th June 2016.

Poster presentation: "O₂ Imaging in 3D cancer cell aggregates: Optimising spheroid models, studying drug responses and revealing new physiological roles of SPCA2 pump". Biophysical Society, 60th Annual Meeting. Los Angeles United States. February 27th-March 2nd 2016.

Oral presentation: "Assessment of cancer cell oxygenation in three dimensions by PLIM microscopy". IPIC, Photonics Ireland. Cork, Ireland. 2th-4th September 2015.

Oral presentation: "New Systems for Oxygen Imaging in Tissues". Microscopy Society of Ireland and Scottish Microscopy Group - Glasgow, UK. November 27th-28th 2014.

Poster presentation: "O₂ Imaging of Biomaterials in 3D porous Scaffolds". 9th Workshop on Advanced Multi-photon and Fluorescence Lifetime Imaging Techniques. FLIM. Saarbruecken, Germany. May 27th-28th, 2014.

8. Bibliography

- [1] A.I. Jeanes, A. Maya-Mendoza, C.H. Streuli, Cellular microenvironment influences the ability of mammary epithelia to undergo cell cycle, *PloS one* 6(3) (2011) e18144.
- [2] S. Breslin, L. O'Driscoll, Three-dimensional cell culture: the missing link in drug discovery, *Drug Discovery Today* 18(5–6) (2013) 240-249.
- [3] Y. Lu, G. Zhang, C. Shen, K. Uygun, M.L. Yarmush, Q. Meng, A Novel 3D Liver Organoid System for Elucidation of Hepatic Glucose Metabolism, *Biotechnology and Bioengineering* 109(2) (2012) 595-604.
- [4] H.K. Dhiman, A.R. Ray, A.K. Panda, Three-dimensional chitosan scaffold-based MCF-7 cell culture for the determination of the cytotoxicity of tamoxifen, *Biomaterials* 26(9) (2005) 979-986.
- [5] H. Baharvand, S.M. Hashemi, S.K. Ashtiani, A. Farrokhi, Differentiation of human embryonic stem cells into hepatocytes in 2D and 3D culture systems in vitro, *International Journal of Developmental Biology* 50(7) (2006) 645.
- [6] P.D. Benya, J.D. Shaffer, Dedifferentiated chondrocytes reexpress the differentiated collagen phenotype when cultured in agarose gels, *Cell* 30(1) (1982) 215-224.
- [7] N. Bono, D. Pezzoli, L. Levesque, C. Loy, G. Candiani, G. Fiore, D. Mantovani, Unraveling the role of mechanical stimulation on smooth muscle cells: A comparative study between 2D and 3D models, *Biotechnology and Bioengineering* (2016).
- [8] J.A. Hickman, R. Graeser, R. de Hoogt, S. Vidic, C. Brito, M. Gutekunst, H. van der Kuip, Three-dimensional models of cancer for pharmacology and cancer cell biology: Capturing tumor complexity in vitro/ex vivo, *Biotechnology journal* 9(9) (2014) 1115-1128.
- [9] E. Knight, S. Przyborski, Advances in 3D cell culture technologies enabling tissue-like structures to be created in vitro, *Journal of Anatomy* 227(6) (2015) 746-756.
- [10] M. Bokhari, R.J. Carnachan, N.R. Cameron, S.A. Przyborski, Culture of HepG2 liver cells on three dimensional polystyrene scaffolds enhances cell structure and function during toxicological challenge, *Journal of Anatomy* 211(4) (2007) 567-576.

- [11] R. Edmondson, J.J. Broglie, A.F. Adcock, L. Yang, Three-dimensional cell culture systems and their applications in drug discovery and cell-based biosensors, *Assay and Drug Development Technologies* 12(4) (2014) 207-218.
- [12] A. Birgersdotter, R. Sandberg, I. Ernberg, Gene expression perturbation in vitro—A growing case for three-dimensional (3D) culture systems, *Seminars in Cancer Biology* 15(5) (2005) 405-412.
- [13] I. Kola, The state of innovation in drug development, *Clinical Pharmacology & Therapeutics* 83(2) (2008) 227-230.
- [14] J. Arrowsmith, Trial watch: phase III and submission failures: 2007–2010, *Nature reviews Drug discovery* 10(2) (2011) 87-87.
- [15] E. Cukierman, R. Pankov, K.M. Yamada, Cell interactions with three-dimensional matrices, *Current Opinion in Cell Biology* 14(5) (2002) 633-640.
- [16] V.M. Weaver, O.W. Petersen, F. Wang, C. Larabell, P. Briand, C. Damsky, M.J. Bissell, Reversion of the malignant phenotype of human breast cells in three-dimensional culture and in vivo by integrin blocking antibodies, *The Journal of cell biology* 137(1) (1997) 231-245.
- [17] A. Abbott, Cell culture: biology's new dimension, *Nature* 424(6951) (2003) 870-872.
- [18] D. Kerr, T. Wheldon, A. Kerr, R. Freshney, S. Kaye, The effect of adriamycin and 4'-deoxydoxorubicin on cell survival of human lung tumour cells grown in monolayer and as spheroids, *British Journal of Cancer* 54(3) (1986) 423.
- [19] J.K. Tunggal, D.S. Cowan, H. Shaikh, I.F. Tannock, Penetration of anticancer drugs through solid tissue: a factor that limits the effectiveness of chemotherapy for solid tumors, *Clinical Cancer Research* 5(6) (1999) 1583-1586.
- [20] C. Wenzel, B. Riefke, S. Gründemann, A. Krebs, S. Christian, F. Prinz, M. Osterland, S. Golfier, S. Räse, N. Ansari, 3D high-content screening for the identification of compounds that target cells in dormant tumor spheroid regions, *Experimental Cell Research* 323(1) (2014) 131-143.
- [21] S.K. Green, G. Francia, C. Isidoro, R.S. Kerbel, Antiadhesive antibodies targeting E-cadherin sensitize multicellular tumor spheroids to chemotherapy in vitro, *Molecular Cancer Therapeutics* 3(2) (2004) 149-159.
- [22] P. Longati, X. Jia, J. Eimer, A. Wagman, M.-R. Witt, S. Rehnmark, C. Verbeke, R. Toftgård, M. Löhr, R.L. Heuchel, 3D pancreatic carcinoma spheroids induce a

matrix-rich, chemoresistant phenotype offering a better model for drug testing, *BMC Cancer* 13(1) (2013) 1.

[23] A.L. Howes, G.G. Chiang, E.S. Lang, C.B. Ho, G. Powis, K. Vuori, R.T. Abraham, The phosphatidylinositol 3-kinase inhibitor, PX-866, is a potent inhibitor of cancer cell motility and growth in three-dimensional cultures, *Molecular Cancer Therapeutics* 6(9) (2007) 2505-2514.

[24] D. Loessner, K.S. Stok, M.P. Lutolf, D.W. Hutmacher, J.A. Clements, S.C. Rizzi, Bioengineered 3D platform to explore cell–ECM interactions and drug resistance of epithelial ovarian cancer cells, *Biomaterials* 31(32) (2010) 8494-8506.

[25] O.M. Maria, O. Maria, Y. Liu, S.V. Komarova, S.D. Tran, Matrigel improves functional properties of human submandibular salivary gland cell line, *The international journal of biochemistry & cell biology* 43(4) (2011) 622-631.

[26] M. Rimann, U. Graf-Hausner, Synthetic 3D multicellular systems for drug development, *Current Opinion in Biotechnology* 23(5) (2012) 803-809.

[27] B. Weigelt, C.M. Ghajar, M.J. Bissell, The need for complex 3D culture models to unravel novel pathways and identify accurate biomarkers in breast cancer, *Advanced Drug Delivery Reviews* 69–70 (2014) 42-51.

[28] A.J. Ryan, C.M. Brougham, C.D. Garcarena, S.W. Kerrigan, F.J. O'Brien, Towards 3D in vitro models for the study of cardiovascular tissues and disease, *Drug Discovery Today*.

[29] E. Fennema, N. Rivron, J. Rouwkema, C. van Blitterswijk, J. de Boer, Spheroid culture as a tool for creating 3D complex tissues, *Trends in Biotechnology* 31(2) (2013) 108-115.

[30] P.A. Kenny, G.Y. Lee, C.A. Myers, R.M. Neve, J.R. Semeiks, P.T. Spellman, K. Lorenz, E.H. Lee, M.H. Barcellos-Hoff, O.W. Petersen, The morphologies of breast cancer cell lines in three-dimensional assays correlate with their profiles of gene expression, *Molecular oncology* 1(1) (2007) 84-96.

[31] T.R. Sodunke, K.K. Turner, S.A. Caldwell, K.W. McBride, M.J. Reginato, Micropatterns of Matrigel for three-dimensional epithelial cultures, *Biomaterials* 28(27) (2007) 4006-4016.

[32] V. Härmä, J. Virtanen, R. Mäkelä, A. Happonen, J.-P. Mpindi, M. Knuutila, P. Kohonen, J. Lötjönen, O. Kallioniemi, M. Nees, A comprehensive panel of three-dimensional models for studies of prostate cancer growth, invasion and drug responses, *PloS one* 5(5) (2010) e10431.

- [33] R.G. Harrison, Observations on the living developing nerve fiber, *Experimental Biology and Medicine* 4(1) (1906) 140-143.
- [34] M.J. Ware, K. Colbert, V. Keshishian, J. Ho, S.J. Corr, S.A. Curley, B. Godin, Generation of Homogenous Three-Dimensional Pancreatic Cancer Cell Spheroids Using an Improved Hanging Drop Technique, *Tissue Engineering Part C: Methods* 22(4) (2016) 312-321.
- [35] Z. Lao, C.J. Kelly, X.-Y. Yang, W.T. Jenkins, E. Toorens, T. Ganguly, S.M. Evans, C.J. Koch, Improved Methods to Generate Spheroid Cultures from Tumor Cells, Tumor Cells & Fibroblasts or Tumor-Fragments: Microenvironment, Microvesicles and MiRNA, *PloS one* 10(7) (2015) e0133895.
- [36] K. Song, T. Liu, X. Li, Z. Cui, X. Sun, X. Ma, Three-dimensional expansion: in suspension culture of SD rat's osteoblasts in a rotating wall vessel bioreactor, *Biomedical and Environmental Sciences* 20(2) (2007) 91.
- [37] L. Moreira Teixeira, J. Leijten, J. Sobral, R. Jin, v.A. Apeldoorn, J. Feijen, v.C. Blitterswijk, P. Dijkstra, H. Karperien, High throughput generated micro-aggregates of chondrocytes stimulate cartilage formation in vitro and in vivo, *European cells & materials* 23 (2012) 387-399.
- [38] A. Woods, G. Wang, H. Dupuis, Z. Shao, F. Beier, Rac1 signaling stimulates N-cadherin expression, mesenchymal condensation, and chondrogenesis, *Journal of Biological Chemistry* 282(32) (2007) 23500-23508.
- [39] H.-G. Kang, J.M. Jenabi, J. Zhang, N. Keshelava, H. Shimada, W.A. May, T. Ng, C.P. Reynolds, T.J. Triche, P.H. Sorensen, E-cadherin cell-cell adhesion in ewing tumor cells mediates suppression of anoikis through activation of the ErbB4 tyrosine kinase, *Cancer Research* 67(7) (2007) 3094-3105.
- [40] Y. Panchina, I. Kelmanson, M. Matz, K. Lukyanov, N. Usman, S. Lukyanov, A ubiquitous family of putative gap junction molecules, *Current Biology* 10(13) (2000) R473-R474.
- [41] B.A. Bao, C.P. Lai, C.C. Naus, J.R. Morgan, Pannexin1 drives multicellular aggregate compaction via a signaling cascade that remodels the actin cytoskeleton, *Journal of Biological Chemistry* 287(11) (2012) 8407-8416.
- [42] A. Vaheri, A. Enzerink, K. Räsänen, P. Salmenperä, NemoSis, a novel way of fibroblast activation, in inflammation and cancer, *Experimental Cell Research* 315(10) (2009) 1633-1638.

- [43] N. Lumelsky, O. Blondel, P. Laeng, I. Velasco, R. Ravin, R. McKay, Differentiation of embryonic stem cells to insulin-secreting structures similar to pancreatic islets, *Science* 292(5520) (2001) 1389-1394.
- [44] I. Kehat, D. Kenyagin-Karsenti, M. Snir, H. Segev, M. Amit, A. Gepstein, E. Livne, O. Binah, J. Itskovitz-Eldor, L. Gepstein, Human embryonic stem cells can differentiate into myocytes with structural and functional properties of cardiomyocytes, *The Journal of clinical investigation* 108(3) (2001) 407-414.
- [45] H. Suga, T. Kadoshima, M. Minaguchi, M. Ohgushi, M. Soen, T. Nakano, N. Takata, T. Wataya, K. Muguruma, H. Miyoshi, Self-formation of functional adenohypophysis in three-dimensional culture, *Nature* 480(7375) (2011) 57-62.
- [46] J. Rouwkema, N.C. Rivron, C.A. van Blitterswijk, Vascularization in tissue engineering, *Trends in Biotechnology* 26(8) (2008) 434-441.
- [47] J. Koffler, K. Kaufman-Francis, Y. Shandalov, D. Egozi, D.A. Pavlov, A. Landesberg, S. Levenberg, Improved vascular organization enhances functional integration of engineered skeletal muscle grafts, *Proceedings of the National Academy of Sciences* 108(36) (2011) 14789-14794.
- [48] J.M. Kelm, M. Fussenegger, Microscale tissue engineering using gravity-enforced cell assembly, *Trends in Biotechnology* 22(4) (2004) 195-202.
- [49] N.C. Rivron, C.C. Raiss, J. Liu, A. Nandakumar, C. Sticht, N. Gretz, R. Truckenmüller, J. Rouwkema, C.A. van Blitterswijk, Sonic Hedgehog-activated engineered blood vessels enhance bone tissue formation, *Proceedings of the National Academy of Sciences* 109(12) (2012) 4413-4418.
- [50] J. Rouwkema, J.D. Boer, C.A.V. Blitterswijk, Endothelial cells assemble into a 3-dimensional prevascular network in a bone tissue engineering construct, *Tissue Engineering* 12(9) (2006) 2685-2693.
- [51] S. Levenberg, J. Rouwkema, M. Macdonald, E.S. Garfein, D.S. Kohane, D.C. Darland, R. Marini, C.A. van Blitterswijk, R.C. Mulligan, P.A. D'Amore, Engineering vascularized skeletal muscle tissue, *Nature Biotechnology* 23(7) (2005) 879-884.
- [52] A. Asthana, W.S. Kisaalita, Microtissue size and hypoxia in HTS with 3D cultures, *Drug Discovery Today* 17(15) (2012) 810-817.
- [53] S.Y. Lee, E.-K. Jeong, H.M. Jeon, C.H. Kim, H.S. Kang, Implication of necrosis-linked p53 aggregation in acquired apoptotic resistance to 5-FU in MCF-7 multicellular tumour spheroids, *Oncology Reports* 24(1) (2010) 73-79.

- [54] G. Mehta, A.Y. Hsiao, M. Ingram, G.D. Luker, S. Takayama, Opportunities and challenges for use of tumor spheroids as models to test drug delivery and efficacy, *Journal of Controlled Release* 164(2) (2012) 192-204.
- [55] Y. Yoshii, A. Waki, K. Yoshida, A. Kakezuka, M. Kobayashi, H. Namiki, Y. Kuroda, Y. Kiyono, H. Yoshii, T. Furukawa, The use of nanoimprinted scaffolds as 3D culture models to facilitate spontaneous tumor cell migration and well-regulated spheroid formation, *Biomaterials* 32(26) (2011) 6052-6058.
- [56] M.L. O'Connor, D. Xiang, S. Shigdar, J. Macdonald, Y. Li, T. Wang, C. Pu, Z. Wang, L. Qiao, W. Duan, Cancer stem cells: a contentious hypothesis now moving forward, *Cancer Letters* 344(2) (2014) 180-187.
- [57] D. Fang, Y. Kim, C. Lee, S. Aggarwal, K. McKinnon, D. Mesmer, J. Norton, C. Birse, T. He, S. Ruben, Expansion of CD133⁺ colon cancer cultures retaining stem cell properties to enable cancer stem cell target discovery, *British Journal of Cancer* 102(8) (2010) 1265-1275.
- [58] L. Wang, R. Mezencev, N.J. Bowen, L.V. Matyunina, J.F. McDonald, Isolation and characterization of stem-like cells from a human ovarian cancer cell line, *Molecular and Cellular Biochemistry* 363(1-2) (2012) 257-268.
- [59] V. Denes, M. Lakk, A. Makarovskiy, P. Jakso, S. Szappanos, L. Graf, L. Mandel, I. Karadi, P. Geck, Metastasis blood test by flow cytometry: In vivo cancer spheroids and the role of hypoxia, *International Journal of Cancer* 136(7) (2015) 1528-1536.
- [60] H. van der Kuip, T.E. Mürdter, M. Sonnenberg, M. McClellan, S. Gutzeit, A. Gerteis, W. Simon, P. Fritz, W.E. Aulitzky, Short term culture of breast cancer tissues to study the activity of the anticancer drug taxol in an intact tumor environment, *BMC Cancer* 6(1) (2006) 86.
- [61] D.L. Holliday, M.A. Moss, S. Pollock, S. Lane, A.M. Shaaban, R. Millican-Slater, C. Nash, A.M. Hanby, V. Speirs, The practicalities of using tissue slices as preclinical organotypic breast cancer models, *Journal of Clinical Pathology* 66(3) (2013) 253-255.
- [62] H. Salmon, K. Franciszkiewicz, D. Damotte, M.-C. Dieu-Nosjean, P. Validire, A. Trautmann, F. Mami-Chouaib, E. Donnadieu, Matrix architecture defines the preferential localization and migration of T cells into the stroma of human lung tumors, *The Journal of clinical investigation* 122(3) (2012) 899-910.

- [63] Y. Liu, F. Lang, X. Xie, S. Prabhu, J. Xu, D. Sampath, K. Aldape, G. Fuller, V. Puduvalli, Efficacy of adenovirally expressed soluble TRAIL in human glioma organotypic slice culture and glioma xenografts, *Cell death & disease* 2(2) (2011) e121.
- [64] M. Geer, K.F. Kuhlmann, C.T. Bakker, F. Kate, R. Oude Elferink, P.J. Bosma, Ex-vivo evaluation of gene therapy vectors in human pancreatic (cancer) tissue slices, *World Journal of Gastroenterology* 15(11) (2009) 1359-1366.
- [65] M.A. Stoff-Khalili, A. Stoff, A.A. Rivera, J.M. Mathis, M. Everts, M. Wang, Y. Kawakami, R. Waehler, Q.L. Matthews, M. Yamamoto, Gene transfer to carcinoma of the breast with fiber-modified adenoviral vectors in a tissue slice model system, *Cancer biology & therapy* 4(11) (2005) 1203-1210.
- [66] R.L. Fisher, A.E. Vickers, Preparation and culture of precision-cut organ slices from human and animal, *Xenobiotica* 43(1) (2013) 8-14.
- [67] M. Dong, C. Philippi, B. Loretz, N. Nafee, U.F. Schaefer, G. Friedel, S. Ammon-Treiber, E.-U. Griese, C.-M. Lehr, U. Klotz, Tissue slice model of human lung cancer to investigate telomerase inhibition by nanoparticle delivery of antisense 2'-O-methyl-RNA, *International Journal of Pharmaceutics* 419(1) (2011) 33-42.
- [68] J.O. Schmid, M. Dong, S. Haubeiss, G. Friedel, S. Bode, A. Grabner, G. Ott, T.E. Mürdter, M. Oren, W.E. Aulitzky, Cancer cells Cue the p53 response of cancer-associated fibroblasts to cisplatin, *Cancer Research* 72(22) (2012) 5824-5832.
- [69] J. Arsenault, A. Nagy, J.T. Henderson, J.A. O'Brien, Regioselective biolistic targeting in organotypic brain slices using a modified gene gun, *Journal of visualized experiments: JoVE* (92) (2014).
- [70] J.T. Ting, T.L. Daigle, Q. Chen, G. Feng, Acute brain slice methods for adult and aging animals: application of targeted patch clamp analysis and optogenetics, *Patch-Clamp Methods and Protocols* (2014) 221-242.
- [71] J. Glykys, K.J. Staley, Developmental Decrease of Neuronal Chloride Concentration Is Independent of Trauma in Thalamocortical Brain Slices, *PloS one* 11(6) (2016) e0158012.
- [72] A.R. Parrish, A.J. Gandolfi, K. Brendel, Precision-cut tissue slices: applications in pharmacology and toxicology, *Life sciences* 57(21) (1995) 1887-1901.
- [73] J. Jenkins, R.I. Dmitriev, K. Morten, K.W. McDermott, D.B. Papkovsky, Oxygen-sensing scaffolds for 3-dimensional cell and tissue culture, *Acta biomaterialia* 16 (2015) 126-135.

- [74] A.J. Engler, S. Sen, H.L. Sweeney, D.E. Discher, Matrix elasticity directs stem cell lineage specification, *Cell* 126(4) (2006) 677-689.
- [75] A.S. Hayward, N. Sano, S.A. Przyborski, N.R. Cameron, Acrylic-Acid-Functionalized PolyHIPE Scaffolds for Use in 3D Cell Culture, *Macromolecular rapid communications* 34(23-24) (2013) 1844-1849.
- [76] M.W. Tibbitt, K.S. Anseth, Hydrogels as extracellular matrix mimics for 3D cell culture, *Biotechnology and Bioengineering* 103(4) (2009) 655-663.
- [77] L. Jongpaiboonkit, W.J. King, G.E. Lyons, A.L. Paguirigan, J.W. Warrick, D.J. Beebe, W.L. Murphy, An adaptable hydrogel array format for 3-dimensional cell culture and analysis, *Biomaterials* 29(23) (2008) 3346-3356.
- [78] X. Chen, A. Ergun, H. Gevgilili, S. Ozkan, D.M. Kalyon, H. Wang, Shell-core bi-layered scaffolds for engineering of vascularized osteon-like structures, *Biomaterials* 34(33) (2013) 8203-8212.
- [79] R. Sharma, S.Z. Barakzai, S.E. Taylor, F.X. Donadeu, Epidermal-like architecture obtained from equine keratinocytes in three-dimensional cultures, *Journal of tissue engineering and regenerative medicine* (2013).
- [80] D. Nisbet, J.S. Forsythe, W. Shen, D. Finkelstein, M.K. Horne, Review paper: a review of the cellular response on electrospun nanofibers for tissue engineering, *Journal of Biomaterials Applications* (2008).
- [81] S. Levenberg, N.F. Huang, E. Lavik, A.B. Rogers, J. Itskovitz-Eldor, R. Langer, Differentiation of human embryonic stem cells on three-dimensional polymer scaffolds, *Proceedings of the National Academy of Sciences* 100(22) (2003) 12741-12746.
- [82] A.G. Mikos, G. Sarakinos, S.M. Leite, J.P. Vacant, R. Langer, Laminated three-dimensional biodegradable foams for use in tissue engineering, *Biomaterials* 14(5) (1993) 323-330.
- [83] E. Knight, B. Murray, R. Carnachan, S. Przyborski, Alvetex(R): polystyrene scaffold technology for routine three dimensional cell culture, *Methods Mol Biol* 695 (2011) 323-40.
- [84] B. Guillotin, F. Guillemot, Cell patterning technologies for organotypic tissue fabrication, *Trends in Biotechnology* 29(4) (2011) 183-190.

- [85] S. Tasoglu, U.A. Gurkan, S. Wang, U. Demirci, Manipulating biological agents and cells in micro-scale volumes for applications in medicine, *Chemical Society Reviews* 42(13) (2013) 5788-5808.
- [86] A. Arslan-Yildiz, R. El Assal, P. Chen, S. Guven, F. Inci, U. Demirci, Towards artificial tissue models: past, present, and future of 3D bioprinting, *Biofabrication* 8(1) (2016) 014103.
- [87] Y.-J. Seol, H.-W. Kang, S.J. Lee, A. Atala, J.J. Yoo, Bioprinting technology and its applications, *European Journal of Cardio-Thoracic Surgery* 46(3) (2014) 342-348.
- [88] J.Y. Park, J.-C. Choi, J.-H. Shim, J.-S. Lee, H. Park, S.W. Kim, J. Doh, D.-W. Cho, A comparative study on collagen type I and hyaluronic acid dependent cell behavior for osteochondral tissue bioprinting, *Biofabrication* 6(3) (2014) 035004.
- [89] C.L. Ventola, Medical applications for 3D printing: current and projected uses, *PT* 39(10) (2014) 704-711.
- [90] S. Moon, E. Ceyhan, U.A. Gurkan, U. Demirci, Statistical modeling of single target cell encapsulation, *PloS one* 6(7) (2011) e21580.
- [91] L. Koch, M. Gruene, C. Unger, B. Chichkov, Laser assisted cell printing, *Current Pharmaceutical Biotechnology* 14(1) (2013) 91-97.
- [92] C.J. Ferris, K.G. Gilmore, G.G. Wallace, Biofabrication: an overview of the approaches used for printing of living cells, *Applied Microbiology and Biotechnology* 97(10) (2013) 4243-4258.
- [93] K.C. Hribar, P. Soman, J. Warner, P. Chung, S. Chen, Light-assisted direct-write of 3D functional biomaterials, *Lab on a chip* 14(2) (2014) 268-275.
- [94] F. Marga, K. Jakab, C. Khatiwala, B. Shephard, S. Dorfman, G. Forgacs, Organ printing: a novel tissue engineering paradigm, 5th European Conference of the International Federation for Medical and Biological Engineering, Springer, 2011, pp. 27-30.
- [95] S. Michael, H. Sorg, C.-T. Peck, L. Koch, A. Deiwick, B. Chichkov, P.M. Vogt, K. Reimers, Tissue engineered skin substitutes created by laser-assisted bioprinting form skin-like structures in the dorsal skin fold chamber in mice, *PloS one* 8(3) (2013) e57741.
- [96] W. Lee, J. Pinckney, V. Lee, J.-H. Lee, K. Fischer, S. Polio, J.-K. Park, S.-S. Yoo, Three-dimensional bioprinting of rat embryonic neural cells, *Neuroreport* 20(8) (2009) 798-803.

- [97] R. Lozano, L. Stevens, B.C. Thompson, K.J. Gilmore, R. Gorkin, E.M. Stewart, M. in het Panhuis, M. Romero-Ortega, G.G. Wallace, 3D printing of layered brain-like structures using peptide modified gellan gum substrates, *Biomaterials* 67 (2015) 264-273.
- [98] K.M. Charoen, B. Fallica, Y.L. Colson, M.H. Zaman, M.W. Grinstaff, Embedded multicellular spheroids as a biomimetic 3D cancer model for evaluating drug and drug-device combinations, *Biomaterials* 35(7) (2014) 2264-2271.
- [99] L.Y. Wu, D. Di Carlo, L.P. Lee, Microfluidic self-assembly of tumor spheroids for anticancer drug discovery, *Biomedical Microdevices* 10(2) (2008) 197-202.
- [100] L. Horváth, Y. Umehara, C. Jud, F. Blank, A. Petri-Fink, B. Rothen-Rutishauser, Engineering an in vitro air-blood barrier by 3D bioprinting, *Scientific reports* 5 (2015).
- [101] H. Li, X. Fan, J. Houghton, Tumor microenvironment: the role of the tumor stroma in cancer, *Journal of Cellular Biochemistry* 101(4) (2007) 805-815.
- [102] X. Wang, L. Sun, M.V. Maffini, A. Soto, C. Sonnenschein, D.L. Kaplan, A complex 3D human tissue culture system based on mammary stromal cells and silk scaffolds for modeling breast morphogenesis and function, *Biomaterials* 31(14) (2010) 3920-3929.
- [103] C. Hoffmann, D. Feger, O. Siedentopf, H. Weber, S. Ueber, J.E. Ehlert, Co-spheroid analysis reveals attenuating effect of HS27A stroma cells on DLD1 colon carcinoma susceptibility to MEK kinase inhibitor trametinib, *Cancer Research* 75(15 Supplement) (2015) 3377-3377.
- [104] L. Gibot, M. Madi, R. Vézinet, M. Rols, Mixed Spheroids as a Relevant 3D Biological Tool to Understand Therapeutic Window of Electrochemotherapy, 1st World Congress on Electroporation and Pulsed Electric Fields in Biology, Medicine and Food & Environmental Technologies, Springer, 2016, pp. 200-203.
- [105] F. Pampaloni, N. Ansari, E.H. Stelzer, High-resolution deep imaging of live cellular spheroids with light-sheet-based fluorescence microscopy, *Cell and Tissue Research* 352(1) (2013) 161-177.
- [106] S.J. Sahl, W. Moerner, Super-resolution fluorescence imaging with single molecules, *Current opinion in structural biology* 23(5) (2013) 778-787.
- [107] S.-H. Shim, C. Xia, G. Zhong, H.P. Babcock, J.C. Vaughan, B. Huang, X. Wang, C. Xu, G.-Q. Bi, X. Zhuang, Super-resolution fluorescence imaging of

- organelles in live cells with photoswitchable membrane probes, *Proceedings of the National Academy of Sciences* 109(35) (2012) 13978-13983.
- [108] Y.M. Wang, B. Judkewitz, C.A. DiMarzio, C. Yang, Deep-tissue focal fluorescence imaging with digitally time-reversed ultrasound-encoded light, *Nature communications* 3 (2012) 928.
- [109] K. König, A. Uchugonova, E. Gorjup, Multiphoton fluorescence lifetime imaging of 3D-stem cell spheroids during differentiation, *Microscopy Research and Technique* 74(1) (2011) 9-17.
- [110] F.C. Zanacchi, Z. Lavagnino, M.P. Donnorso, A. Del Bue, L. Furia, M. Faretta, A. Diaspro, Live-cell 3D super-resolution imaging in thick biological samples, *Nature methods* 8(12) (2011) 1047-1049.
- [111] M. Wartenberg, H. Acker, Quantitative recording of vitality patterns in living multicellular spheroids by confocal microscopy, *Micron* 26(5) (1995) 395-404.
- [112] A.J. Walsh, R.S. Cook, M.E. Sanders, L. Aurisicchio, G. Ciliberto, C.L. Arteaga, M.C. Skala, Quantitative optical imaging of primary tumor organoid metabolism predicts drug response in breast cancer, *Cancer Research* 74(18) (2014) 5184-5194.
- [113] C. Greb, *Basic Principles of Luminescence*, (2012).
- [114] J.W. Lichtman, J.-A. Conchello, Fluorescence microscopy, *Nature methods* 2(12) (2005) 910-919.
- [115] E.M. Goldys, *Fluorescence applications in biotechnology and life sciences*, John Wiley & Sons 2009.
- [116] W. Becker, *Advanced Time-Correlated Single Photon Counting Applications*, Springer 2015.
- [117] K. Suhling, L.M. Hirvonen, J.A. Levitt, P.-H. Chung, C. Tregidgo, A. Le Marois, D.A. Rusakov, K. Zheng, S. Ameer-Beg, S. Poland, Fluorescence lifetime imaging (FLIM): Basic concepts and some recent developments, *Medical Photonics* 27 (2015) 3-40.
- [118] M.Y. Berezin, S. Achilefu, Fluorescence lifetime measurements and biological imaging, *Chemical reviews* 110(5) (2010) 2641-2684.
- [119] V. Shcheslavskiy, A. Neubauer, R. Bukowiecki, F. Dinter, W. Becker, Combined fluorescence and phosphorescence lifetime imaging, *Applied Physics Letters* 108(9) (2016) 091111.

- [120] R.I. Dmitriev, D.B. Papkovsky, Optical probes and techniques for O₂ measurement in live cells and tissue, *Cellular and molecular life sciences : CMLS* 69(12) (2012) 2025-39.
- [121] C. Schweitzer, R. Schmidt, Physical mechanisms of generation and deactivation of singlet oxygen, *Chemical reviews* 103(5) (2003) 1685-1758.
- [122] M. Fernández-Suárez, A.Y. Ting, Fluorescent probes for super-resolution imaging in living cells, *Nature Reviews Molecular Cell Biology* 9(12) (2008) 929-943.
- [123] C.A. Combs, Fluorescence microscopy: a concise guide to current imaging methods, *Current Protocols in Neuroscience* (2010) 2.1. 1-2.1. 14.
- [124] A. Fercher, T.C. O’Riordan, A.V. Zhdanov, R.I. Dmitriev, D.B. Papkovsky, Imaging of cellular oxygen and analysis of metabolic responses of mammalian cells, *Live Cell Imaging*, Springer2010, pp. 257-273.
- [125] D.F. Wilson, O.S. Finikova, A.Y. Lebedev, S. Apreleva, A. Pastuszko, W.M. Lee, S.A. Vinogradov, Measuring oxygen in living tissue: intravascular, interstitial, and “tissue” oxygen measurements, *Oxygen Transport to Tissue XXXII*, Springer2011, pp. 53-59.
- [126] T.C. O’Riordan, A.V. Zhdanov, G.V. Ponomarev, D.B. Papkovsky, Analysis of intracellular oxygen and metabolic responses of mammalian cells by time-resolved fluorometry, *Analytical chemistry* 79(24) (2007) 9414-9419.
- [127] W.A. Lea, A. Simeonov, Fluorescence polarization assays in small molecule screening, *Expert opinion on drug discovery* 6(1) (2011) 17-32.
- [128] J.C. Owicki, Fluorescence polarization and anisotropy in high throughput screening: perspectives and primer, *Journal of Biomolecular Screening* 5(5) (2000) 297-306.
- [129] Y. Chen, A. Periasamy, Characterization of two-photon excitation fluorescence lifetime imaging microscopy for protein localization, *Microscopy Research and Technique* 63(1) (2004) 72-80.
- [130] J. Jenkins, R. Dmitriev, D. Papkovsky, Imaging Cell and Tissue O₂ by TCSPC-PLIM, in: W. Becker (Ed.), *Advanced Time-Correlated Single Photon Counting Applications*, Springer International Publishing2015, pp. 225-247.
- [131] A. Vollrath, S. Schubert, U.S. Schubert, Fluorescence imaging of cancer tissue based on metal-free polymeric nanoparticles—a review, *Journal of Materials Chemistry B* 1(15) (2013) 1994-2007.

- [132] S. Foersch, A. Heimann, A. Ayyad, G.A. Spoden, L. Florin, K. Mpoukouvalas, R. Kiesslich, O. Kempfski, M. Goetz, P. Charalampaki, Confocal laser endomicroscopy for diagnosis and histomorphologic imaging of brain tumors in vivo, *PloS one* 7(7) (2012) e41760.
- [133] X.-D. Jiang, R. Gao, Y. Yue, G.-T. Sun, W. Zhao, A NIR BODIPY dye bearing 3, 4, 4 a-trihydroxanthene moieties, *Organic & biomolecular chemistry* 10(34) (2012) 6861-6865.
- [134] R. Xu, B. Qiang, J. Mao, Near infrared imaging of tissue heterogeneity: probe design and sensitivity analysis, 2005 IEEE Engineering in Medicine and Biology 27th Annual Conference, IEEE, 2006, pp. 278-281.
- [135] A.J. Nichols, E. Roussakis, O.J. Klein, C.L. Evans, Click-Assembled, Oxygen-Sensing Nanoconjugates for Depth-Resolved, Near-Infrared Imaging in a 3 D Cancer Model, *Angewandte Chemie International Edition* 53(14) (2014) 3671-3674.
- [136] R.I. Dmitriev, S.M. Borisov, H. DÜssmann, S. Sun, B.J. Müller, J. Prehn, V.P. Baklaushev, I. Klimant, D.B. Papkovsky, Versatile Conjugated Polymer Nanoparticles for High-Resolution O₂ Imaging in Cells and 3D Tissue Models, *ACS Nano* 9(5) (2015) 5275-5288.
- [137] S. Shukla, A.P. Skoumbourdis, M.J. Walsh, A.M. Hartz, K.L. Fung, C.-P. Wu, M.M. Gottesman, B.r. Bauer, C.J. Thomas, S.V. Ambudkar, Synthesis and characterization of a BODIPY conjugate of the BCR-ABL kinase inhibitor Tassigna (nilotinib): evidence for transport of Tassigna and its fluorescent derivative by ABC drug transporters, *Molecular Pharmaceutics* 8(4) (2011) 1292-1302.
- [138] A. Matsui, E. Tanaka, H.S. Choi, V. Kianzad, S. Gioux, S.J. Lomnes, J.V. Frangioni, Real-time, near-infrared, fluorescence-guided identification of the ureters using methylene blue, *Surgery* 148(1) (2010) 78-86.
- [139] X. Zhao, Y. Li, D. Jin, Y. Xing, X. Yan, L. Chen, A near-infrared multifunctional fluorescent probe with an inherent tumor-targeting property for bioimaging, *Chemical Communications* 51(58) (2015) 11721-11724.
- [140] K. Sano, M. Mitsunaga, T. Nakajima, P.L. Choyke, H. Kobayashi, In vivo breast cancer characterization imaging using two monoclonal antibodies activatably labeled with near infrared fluorophores, *Breast Cancer Res* 14(2) (2012) R61.
- [141] X. Tan, S. Luo, D. Wang, Y. Su, T. Cheng, C. Shi, A NIR heptamethine dye with intrinsic cancer targeting, imaging and photosensitizing properties, *Biomaterials* 33(7) (2012) 2230-2239.

- [142] H. Lee, W. Akers, K. Bhushan, S. Bloch, G. Sudlow, R. Tang, S. Achilefu, Near-infrared pH-activatable fluorescent probes for imaging primary and metastatic breast tumors, *Bioconjugate Chemistry* 22(4) (2011) 777-784.
- [143] R. Weissleder, C.-H. Tung, U. Mahmood, A. Bogdanov, In vivo imaging of tumors with protease-activated near-infrared fluorescent probes, *Nature Biotechnology* 17(4) (1999) 375-378.
- [144] J. Li, K. Chen, H. Liu, K. Cheng, M. Yang, J. Zhang, J.D. Cheng, Y. Zhang, Z. Cheng, Activatable near-infrared fluorescent probe for in vivo imaging of fibroblast activation protein- α , *Bioconjugate Chemistry* 23(8) (2012) 1704-1711.
- [145] B.-W. Xie, I.M. Mol, S. Keereweer, E.R. Van Beek, I. Que, T.J. Snoeks, A. Chan, E.L. Kaijzel, C.W. Löwik, Dual-wavelength imaging of tumor progression by activatable and targeting near-infrared fluorescent probes in a bioluminescent breast cancer model, *PloS one* 7(2) (2012) e31875.
- [146] T.K. Dash, V.B. Konkimalla, Poly- ϵ -caprolactone based formulations for drug delivery and tissue engineering: A review, *Journal of Controlled Release* 158(1) (2012) 15-33.
- [147] P. Ahlin Grabnar, J. Kristl, The manufacturing techniques of drug-loaded polymeric nanoparticles from preformed polymers, *Journal of Microencapsulation* 28(4) (2011) 323-335.
- [148] S. Mao, W. Sun, T. Kissel, Chitosan-based formulations for delivery of DNA and siRNA, *Advanced Drug Delivery Reviews* 62(1) (2010) 12-27.
- [149] Z. Liu, Y. Jiao, Y. Wang, C. Zhou, Z. Zhang, Polysaccharides-based nanoparticles as drug delivery systems, *Advanced Drug Delivery Reviews* 60(15) (2008) 1650-1662.
- [150] A. Musyanovych, R. Rossmann, C. Tontsch, K. Landfester, Effect of hydrophilic comonomer and surfactant type on the colloidal stability and size distribution of carboxyl- and amino-functionalized polystyrene particles prepared by miniemulsion polymerization, *Langmuir* 23(10) (2007) 5367-5376.
- [151] A. Albanese, P.S. Tang, W.C. Chan, The effect of nanoparticle size, shape, and surface chemistry on biological systems, *Annual Review of Biomedical Engineering* 14 (2012) 1-16.
- [152] J. Wang, J.D. Byrne, M.E. Napier, J.M. DeSimone, More effective nanomedicines through particle design, *Small* 7(14) (2011) 1919-1931.

- [153] F. Alexis, E. Pridgen, L.K. Molnar, O.C. Farokhzad, Factors affecting the clearance and biodistribution of polymeric nanoparticles, *Molecular Pharmaceutics* 5(4) (2008) 505-515.
- [154] J.C. Pickup, F. Hussain, N.D. Evans, O.J. Rolinski, D.J. Birch, Fluorescence-based glucose sensors, *Biosensors and Bioelectronics* 20(12) (2005) 2555-2565.
- [155] A. San Martín, S. Ceballo, I. Ruminot, R. Lerchundi, W.B. Frommer, L.F. Barros, A genetically encoded FRET lactate sensor and its use to detect the Warburg effect in single cancer cells, *PloS one* 8(2) (2013) e57712.
- [156] X. Zhang, X. Zhang, B. Yang, M. Liu, W. Liu, Y. Chen, Y. Wei, Polymerizable aggregation-induced emission dye-based fluorescent nanoparticles for cell imaging applications, *Polymer Chemistry* 5(2) (2014) 356-360.
- [157] W. Becker, Introduction to Multi-dimensional TCSPC, *Advanced Time-Correlated Single Photon Counting Applications*, Springer 2015, pp. 1-63.
- [158] I.H. Madshus, Regulation of intracellular pH in eukaryotic cells, *Biochemical Journal* 250(1) (1988) 1.
- [159] M. Fidelman, S. Seeholzer, K. Walsh, R. Moore, Intracellular pH mediates action of insulin on glycolysis in frog skeletal muscle, *American Journal of Physiology-Cell Physiology* 242(1) (1982) C87-C93.
- [160] J. Han, K. Burgess, Fluorescent indicators for intracellular pH, *Chemical reviews* 110(5) (2009) 2709-2728.
- [161] N. Altan, Y. Chen, M. Schindler, S.M. Simon, Defective acidification in human breast tumor cells and implications for chemotherapy, *The Journal of experimental medicine* 187(10) (1998) 1583-1598.
- [162] P. Sarder, D. Maji, S. Achilefu, Molecular probes for fluorescence lifetime imaging, *Bioconjugate chemistry* 26(6) (2015) 963-974.
- [163] C. Hille, M. Berg, L. Bressel, D. Munzke, P. Primus, H.-G. Löhmannsröben, C. Dosche, Time-domain fluorescence lifetime imaging for intracellular pH sensing in living tissues, *Analytical and bioanalytical chemistry* 391(5) (2008) 1871-1879.
- [164] M.Y. Berezin, J. Kao, S. Achilefu, pH-Dependent Optical Properties of Synthetic Fluorescent Imidazoles, *Chemistry—A European Journal* 15(14) (2009) 3560-3566.
- [165] A. Almutairi, S.J. Guillaudeu, M.Y. Berezin, S. Achilefu, J.M. Fréchet, Biodegradable pH-sensing dendritic nanoprobe for near-infrared fluorescence

lifetime and intensity imaging, *Journal of the American Chemical Society* 130(2) (2008) 444-445.

[166] O. Kreft, A.M. Javier, G.B. Sukhorukov, W.J. Parak, Polymer microcapsules as mobile local pH-sensors, *Journal of Materials Chemistry* 17(42) (2007) 4471-4476.

[167] O. Seksek, N. Henry-Toulme, F. Sureau, J. Bolard, SNARF-1 as an intracellular pH indicator in laser microspectrofluorometry: a critical assessment, *Analytical biochemistry* 193(1) (1991) 49-54.

[168] K. Buckler, R. Vaughan-Jones, Application of a new pH-sensitive fluoroprobe (carboxy-SNARF-1) for intracellular pH measurement in small, isolated cells, *Pflügers Archiv* 417(2) (1990) 234-239.

[169] V.K. Ramshesh, J.J. Lemasters, Imaging of mitochondrial pH using SNARF-1, *Mitochondrial Bioenergetics: Methods and Protocols* (2012) 243-248.

[170] T. Jokic, S.M. Borisov, R. Saf, D.A. Nielsen, M. Köhl, I. Klimant, Highly photostable near-infrared fluorescent pH indicators and sensors based on BF₂-chelated tetraarylazadipyrrromethene dyes, *Analytical chemistry* 84(15) (2012) 6723-6730.

[171] Y. Ni, J. Wu, Far-red and near infrared BODIPY dyes: synthesis and applications for fluorescent pH probes and bio-imaging, *Organic & biomolecular chemistry* 12(23) (2014) 3774-3791.

[172] T.S. Blacker, M.R. Duchon, Investigating mitochondrial redox state using NADH and NADPH autofluorescence, *Free Radical Biology and Medicine* (2016).

[173] T.S. Blacker, Z.F. Mann, J.E. Gale, M. Ziegler, A.J. Bain, G. Szabadkai, M.R. Duchon, Separating NADH and NADPH fluorescence in live cells and tissues using FLIM, *Nature communications* 5 (2014).

[174] D.S. Bilan, M.E. Matlashov, A.Y. Gorokhovatsky, C. Schultz, G. Enikolopov, V.V. Belousov, Genetically encoded fluorescent indicator for imaging NAD⁺/NADH ratio changes in different cellular compartments, *Biochimica et Biophysica Acta (BBA)-General Subjects* 1840(3) (2014) 951-957.

[175] X.A. Cambronne, M.L. Stewart, D. Kim, A.M. Jones-Brunette, R.K. Morgan, D.L. Farrens, M.S. Cohen, R.H. Goodman, Biosensor reveals multiple sources for mitochondrial NAD⁺, *Science* 352(6292) (2016) 1474-1477.

[176] M. Balu, A. Mazhar, C.K. Hayakawa, R. Mittal, T.B. Krasieva, K. König, V. Venugopalan, B.J. Tromberg, In vivo multiphoton NADH fluorescence reveals

depth-dependent keratinocyte metabolism in human skin, *Biophysical Journal* 104(1) (2013) 258-267.

[177] B. Chance, H. Baltscheffsky, Respiratory enzymes in oxidative phosphorylation VII. Binding of intramitochondrial reduced pyridine nucleotide, *Journal of Biological Chemistry* 233(3) (1958) 736-739.

[178] B. Chance, N. Oshino, T. Sugano, A. Mayevsky, Basic principles of tissue oxygen determination from mitochondrial signals, *Oxygen Transport to Tissue*, Springer 1973, pp. 277-292.

[179] W.Y. Sanchez, T.W. Prow, W.H. Sanchez, J.E. Grice, M.S. Roberts, Analysis of the metabolic deterioration of ex vivo skin from ischemic necrosis through the imaging of intracellular NAD (P) H by multiphoton tomography and fluorescence lifetime imaging microscopy, *Journal of biomedical optics* 15(4) (2010) 046008-046008-11.

[180] J.A. Palero, A.N. Bader, H.S. de Bruijn, H.J. Sterenborg, H.C. Gerritsen, In vivo monitoring of protein-bound and free NADH during ischemia by nonlinear spectral imaging microscopy, *Biomedical optics express* 2(5) (2011) 1030-1039.

[181] A. Bahat, I. Tur-Kaspa, A. Gakamsky, L.C. Giojalas, H. Breitbart, M. Eisenbach, Thermotaxis of mammalian sperm cells: a potential navigation mechanism in the female genital tract, *Nature Medicine* 9(2) (2003) 149-150.

[182] D. Warner, R. Shine, The adaptive significance of temperature-dependent sex determination in a reptile, *Nature* 451(7178) (2008) 566-568.

[183] R.S. Seymour, Biophysics and physiology of temperature regulation in thermogenic flowers, *Bioscience Reports* 21(2) (2001) 223-236.

[184] B.B. Lowell, B.M. Spiegelman, Towards a molecular understanding of adaptive thermogenesis, *Nature* 404(6778) (2000) 652-660.

[185] M. Monti, L. Brandt, J. Ikomi-Kumm, H. Olsson, Microcalorimetric investigation of cell metabolism in tumour cells from patients with non-Hodgkin lymphoma (NHL), *Scandinavian journal of haematology* 36(4) (1986) 353-357.

[186] S. Uchiyama, A. Prasanna de Silva, K. Iwai, Luminescent molecular thermometers, *Journal of chemical education* 83(5) (2006) 720.

[187] C. Chapman, Y. Liu, G. Sonek, B. Tromberg, The use of exogenous fluorescent probes for temperature measurements in single living cells, *Photochemistry and Photobiology* 62(3) (1995) 416-425.

- [188] O. Zohar, M. Ikeda, H. Shinagawa, H. Inoue, H. Nakamura, D. Elbaum, D.L. Alkon, T. Yoshioka, Thermal imaging of receptor-activated heat production in single cells, *Biophysical Journal* 74(1) (1998) 82-89.
- [189] K. Okabe, N. Inada, C. Gota, Y. Harada, T. Funatsu, S. Uchiyama, Intracellular temperature mapping with a fluorescent polymeric thermometer and fluorescence lifetime imaging microscopy, *Nature communications* 3 (2012) 705.
- [190] E. Ring, K. Ammer, Infrared thermal imaging in medicine, *Physiological measurement* 33(3) (2012) R33.
- [191] X.-d. Wang, O.S. Wolfbeis, R.J. Meier, Luminescent probes and sensors for temperature, *Chemical Society Reviews* 42(19) (2013) 7834-7869.
- [192] T. Hayashi, N. Fukuda, S. Uchiyama, N. Inada, A cell-permeable fluorescent polymeric thermometer for intracellular temperature mapping in mammalian cell lines, *PloS one* 10(2) (2015) e0117677.
- [193] J.S. Donner, S.A. Thompson, M.P. Kreuzer, G. Baffou, R. Quidant, Mapping intracellular temperature using green fluorescent protein, *Nano Letters* 12(4) (2012) 2107-2111.
- [194] B. Valeur, M.N. Berberan-Santos, *Molecular fluorescence: principles and applications*, John Wiley & Sons 2012.
- [195] J. Sakakibara, R. Adrian, Whole field measurement of temperature in water using two-color laser induced fluorescence, *Experiments in Fluids* 26(1-2) (1999) 7-15.
- [196] A. Soleilhac, M. Girod, P. Dugourd, B. Burdin, J. Parvole, P.-Y. Dugas, F. Bayard, E. Lacôte, E. Bourgeat-Lami, R. Antoine, Temperature response of rhodamine B-doped latex particles. From solution to single particles, *Langmuir* 32(16) (2016) 4052-4058.
- [197] I. Rosenthal, P. Peretz, K. Muszkat, Thermochromic and hyperchromic effects in rhodamine B solutions, *Journal of Physical Chemistry* 83(3) (1979) 350-353.
- [198] D. Day, M. Gu, Optical characterization of the heating performance of microchannel fluid flow, *Optics and Lasers in Engineering* 48(1) (2010) 32-36.
- [199] Y. Onganer, E.L. Quitevis, Effect of solvent on nonradiative processes in xanthene dyes: pyronin B in alcohols and alcohol-water mixtures, *The Journal of Physical Chemistry* 96(20) (1992) 7996-8001.

- [200] C. Paviolo, A. Clayton, S. McArthur, P. Stoddart, Temperature measurement in the microscopic regime: a comparison between fluorescence lifetime-and intensity-based methods, *Journal of microscopy* 250(3) (2013) 179-188.
- [201] Y.Y. Chen, A.W. Wood, Application of a temperature-dependent fluorescent dye (Rhodamine B) to the measurement of radiofrequency radiation-induced temperature changes in biological samples, *Bioelectromagnetics* 30(7) (2009) 583-590.
- [202] S. Arai, S.-C. Lee, D. Zhai, M. Suzuki, Y.T. Chang, A molecular fluorescent probe for targeted visualization of temperature at the endoplasmic reticulum, *Scientific reports* 4 (2014) 6701.
- [203] H. Itoh, S. Arai, T. Sudhakaran, S.-C. Lee, Y.-T. Chang, S.i. Ishiwata, M. Suzuki, E.B. Lane, Direct organelle thermometry with fluorescence lifetime imaging microscopy in single myotubes, *Chemical Communications* 52(24) (2016) 4458-4461.
- [204] R.P. Rubin, G.B. Weiss, W. James Jr, *Calcium in biological systems*, Springer Science & Business Media 2013.
- [205] C. Wei, X. Wang, M. Zheng, H. Cheng, Calcium gradients underlying cell migration, *Current opinion in cell biology* 24(2) (2012) 254-261.
- [206] E.A. Lukyanetz, V.M. Shkryl, O.V. Kravchuk, P.G. Kostyuk, Effect of hypoxia on calcium channels depends on extracellular calcium in CA1 hippocampal neurons, *Brain Res* 980(1) (2003) 128-34.
- [207] K.A. Seta, Y. Yuan, Z. Spicer, G. Lu, J. Bedard, T.K. Ferguson, P. Pathrose, A. Cole-Strauss, A. Kaufhold, D.E. Millhorn, The role of calcium in hypoxia-induced signal transduction and gene expression, *Cell Calcium* 36(3) (2004) 331-340.
- [208] O.H. Petersen, N. Burdakova, *Fluorescent Probes Used for Measuring Intracellular Calcium*, eLS, John Wiley & Sons, Ltd 2001.
- [209] I. Johnson, Review: Fluorescent probes for living cells, *The Histochemical Journal* 30(3) (1998) 123-140.
- [210] O. Garaschuk, O. Griesbeck, A. Konnerth, Troponin C-based biosensors: a new family of genetically encoded indicators for in vivo calcium imaging in the nervous system, *Cell calcium* 42(4) (2007) 351-361.

- [211] R.M. Paredes, J.C. Etzler, L.T. Watts, W. Zheng, J.D. Lechleiter, Chemical calcium indicators, *Methods* 46(3) (2008) 143-151.
- [212] N.L. Rochefort, H. Jia, A. Konnerth, Calcium imaging in the living brain: prospects for molecular medicine, *Trends in molecular medicine* 14(9) (2008) 389-399.
- [213] J.T. Russell, Imaging calcium signals in vivo: a powerful tool in physiology and pharmacology, *British journal of pharmacology* 163(8) (2011) 1605-1625.
- [214] Y. Zhao, S. Araki, J. Wu, T. Teramoto, Y.-F. Chang, M. Nakano, A.S. Abdelfattah, M. Fujiwara, T. Ishihara, T. Nagai, An expanded palette of genetically encoded Ca²⁺ indicators, *Science* 333(6051) (2011) 1888-1891.
- [215] G. Grynkiewicz, M. Poenie, R.Y. Tsien, A new generation of Ca²⁺ indicators with greatly improved fluorescence properties, *Journal of Biological Chemistry* 260(6) (1985) 3440-3450.
- [216] K. Hirabayashi, K. Hanaoka, T. Egawa, C. Kobayashi, S. Takahashi, T. Komatsu, T. Ueno, T. Terai, Y. Ikegaya, T. Nagano, Development of Practical Red Fluorescent Probe for Cytoplasmic Calcium Ions with Greatly Improved Cell-membrane Permeability, *Cell Calcium* (2016).
- [217] A. Minta, J. Kao, R.Y. Tsien, Fluorescent indicators for cytosolic calcium based on rhodamine and fluorescein chromophores, *Journal of Biological Chemistry* 264(14) (1989) 8171-8178.
- [218] J. Nakai, M. Ohkura, K. Imoto, A high signal-to-noise Ca²⁺ probe composed of a single green fluorescent protein, *Nature biotechnology* 19(2) (2001) 137-141.
- [219] Y.N. Tallini, M. Ohkura, B.-R. Choi, G. Ji, K. Imoto, R. Doran, J. Lee, P. Plan, J. Wilson, H.-B. Xin, Imaging cellular signals in the heart in vivo: Cardiac expression of the high-signal Ca²⁺ indicator GCaMP2, *Proceedings of the National Academy of Sciences of the United States of America* 103(12) (2006) 4753-4758.
- [220] M. Ohkura, M. Matsuzaki, H. Kasai, K. Imoto, J. Nakai, Genetically encoded bright Ca²⁺ probe applicable for dynamic Ca²⁺ imaging of dendritic spines, *Analytical chemistry* 77(18) (2005) 5861-5869.
- [221] J. Akerboom, J.D.V. Rivera, M.M.R. Guilbe, E.C.A. Malavé, H.H. Hernandez, L. Tian, S.A. Hires, J.S. Marvin, L.L. Looger, E.R. Schreier, Crystal structures of the GCaMP calcium sensor reveal the mechanism of fluorescence signal change and aid rational design, *Journal of Biological Chemistry* 284(10) (2009) 6455-6464.

- [222] R. Laine, D.W. Stuckey, H. Manning, S.C. Warren, G. Kennedy, D. Carling, C. Dunsby, A. Sardini, P.M. French, Fluorescence lifetime readouts of Troponin-C-based calcium FRET sensors: A quantitative comparison of CFP and mTFP1 as donor fluorophores, *PLoS One* 7(11) (2012) e49200.
- [223] M.D. Brand, D.G. Nicholls, Assessing mitochondrial dysfunction in cells, *Biochemical Journal* 435(2) (2011) 297-312.
- [224] G.L. Semenza, Oxygen homeostasis, *Wiley Interdisciplinary Reviews: Systems Biology and Medicine* 2(3) (2010) 336-361.
- [225] D.B. Papkovsky, R.I. Dmitriev, Biological detection by optical oxygen sensing, *Chemical Society Reviews* 42(22) (2013) 8700-8732.
- [226] Y. Feng, J. Cheng, L. Zhou, X. Zhou, H. Xiang, Ratiometric optical oxygen sensing: a review in respect of material design, *Analyst* 137(21) (2012) 4885-4901.
- [227] M. Quaranta, S.M. Borisov, I. Klimant, Indicators for optical oxygen sensors, *Bioanal Rev* 4(2-4) (2012) 115-157.
- [228] Y. Amao, I. Okura, Optical oxygen sensor devices using metalloporphyrins, *Journal of Porphyrins and Phthalocyanines* 13(11) (2009) 1111-1122.
- [229] A. Ruggi, F.W. van Leeuwen, A.H. Velders, Interaction of dioxygen with the electronic excited state of Ir (III) and Ru (II) complexes: principles and biomedical applications, *Coordination Chemistry Reviews* 255(21) (2011) 2542-2554.
- [230] S.J. Cringle, K.Y. Paula, E.-N. Su, D.-Y. Yu, Oxygen distribution and consumption in the developing rat retina, *Investigative ophthalmology & visual science* 47(9) (2006) 4072-4076.
- [231] K. Kellner, G. Liebsch, I. Klimant, O.S. Wolfbeis, T. Blunk, M.B. Schulz, A. Göpferich, Determination of oxygen gradients in engineered tissue using a fluorescent sensor, *Biotechnology and Bioengineering* 80(1) (2002) 73-83.
- [232] A.A. Gerencser, A. Neilson, S.W. Choi, U. Edman, N. Yadava, R.J. Oh, D.A. Ferrick, D.G. Nicholls, M.D. Brand, Quantitative microplate-based respirometry with correction for oxygen diffusion, *Analytical chemistry* 81(16) (2009) 6868-6878.
- [233] X.-D. Wang, O.S. Wolfbeis, Fiber-optic chemical sensors and biosensors (2008–2012), *Analytical chemistry* 85(2) (2012) 487-508.
- [234] X.-d. Wang, H.-x. Chen, Y. Zhao, X. Chen, X.-r. Wang, Optical oxygen sensors move towards colorimetric determination, *TrAC Trends in Analytical Chemistry* 29(4) (2010) 319-338.

- [235] S.M. Borisov, T. Mayr, I. Klimant, Poly (styrene-block-vinylpyrrolidone) beads as a versatile material for simple fabrication of optical nanosensors, *Analytical chemistry* 80(3) (2008) 573-582.
- [236] Y. Amao, K. Asai, T. Miyashita, I. Okura, Novel optical oxygen sensing material: platinum porphyrin-fluoropolymer film, *Polymers for Advanced Technologies* 11(8-12) (2000) 705-709.
- [237] X. Chen, Z. Zhong, Z. Li, Y. Jiang, X. Wang, K. Wong, Characterization of ormosil film for dissolved oxygen-sensing, *Sensors and Actuators B: Chemical* 87(2) (2002) 233-238.
- [238] H. Glever, B. MacCraith, J. Vos, The preparation of a sol-gel glass oxygen sensor incorporating a covalently bound fluorescent dye, *Analytical Communications* 36(1) (1999) 3-4.
- [239] H. Schmidt, G. Jonschker, S. Goedicke, M. Mennig, The sol-gel process as a basic technology for nanoparticle-dispersed inorganic-organic composites, *Journal of Sol-Gel Science and Technology* 19(1-3) (2000) 39-51.
- [240] C. Sanchez, F. Ribot, B. Lebeau, Molecular design of hybrid organic-inorganic nanocomposites synthesized via sol-gel chemistry, *Journal of Materials Chemistry* 9(1) (1999) 35-44.
- [241] L. Cot, A. Ayrat, J. Durand, C. Guizard, N. Hovnanian, A. Julbe, A. Larbot, Inorganic membranes and solid state sciences, *Solid State Sciences* 2(3) (2000) 313-334.
- [242] E.R. Carraway, J.N. Demas, B.A. DeGraff, J.R. Bacon, Photophysics and photochemistry of oxygen sensors based on luminescent transition-metal complexes, *Analytical chemistry* 63(4) (1991) 337-342.
- [243] R.I. Dmitriev, D.B. Papkovsky, Intracellular probes for imaging oxygen concentration: how good are they?, *Methods and Applications in Fluorescence* 3(3) (2015) 034001.
- [244] M.C. Hogan, Phosphorescence quenching method for measurement of intracellular in isolated skeletal muscle fibers, *Journal of Applied Physiology* 86(2) (1999) 720-724.
- [245] U. Neugebauer, Y. Pellegrin, M. Devocelle, R.J. Forster, W. Signac, N. Moran, T.E. Keyes, Ruthenium polypyridyl peptide conjugates: membrane permeable probes for cellular imaging, *Chemical Communications* (42) (2008) 5307-5309.

- [246] A. Fercher, G.V. Ponomarev, D. Yashunski, D. Papkovsky, Evaluation of the derivatives of phosphorescent Pt-coproporphyrin as intracellular oxygen-sensitive probes, *Analytical and Bioanalytical Chemistry* 396(5) (2010) 1793-1803.
- [247] C. Wu, B. Bull, K. Christensen, J. McNeill, Ratiometric Single-Nanoparticle Oxygen Sensors for Biological Imaging, *Angewandte Chemie International Edition* 48(15) (2009) 2741-2745.
- [248] X.-d. Wang, H.H. Gorris, J.A. Stolwijk, R.J. Meier, D.B. Groegel, J. Wegener, O.S. Wolfbeis, Self-referenced RGB colour imaging of intracellular oxygen, *Chemical Science* 2(5) (2011) 901-906.
- [249] S. Das, P.K. Suresh, R. Desmukh, Design of Eudragit RL 100 nanoparticles by nanoprecipitation method for ocular drug delivery, *Nanomedicine: Nanotechnology, Biology and Medicine* 6(2) (2010) 318-323.
- [250] A. Fercher, S.M. Borisov, A.V. Zhdanov, I. Klimant, D.B. Papkovsky, Intracellular O₂ sensing probe based on cell-penetrating phosphorescent nanoparticles, *Acs Nano* 5(7) (2011) 5499-5508.
- [251] S.M. Borisov, T. Mayr, G. Mistlberger, K. Waich, K. Koren, P. Chojnacki, I. Klimant, Precipitation as a simple and versatile method for preparation of optical nanochemosensors, *Talanta* 79(5) (2009) 1322-1330.
- [252] R. Dmitriev, S. Borisov, A. Kondrashina, J.P. Pakan, U. Anilkumar, J.M. Prehn, A. Zhdanov, K. McDermott, I. Klimant, D. Papkovsky, Imaging oxygen in neural cell and tissue models by means of anionic cell-permeable phosphorescent nanoparticles, *Cell. Mol. Life Sci.* (2014) 1-15.
- [253] A. Verma, F. Stellacci, Effect of surface properties on nanoparticle–cell interactions, *Small* 6(1) (2010) 12-21.
- [254] M. Nikinmaa, What is hypoxia?, *Acta Physiologica* 209(1) (2013) 1-4.
- [255] L. Albenberg, T.V. Esipova, C.P. Judge, K. Bittinger, J. Chen, A. Laughlin, S. Grunberg, R.N. Baldassano, J.D. Lewis, H. Li, S.R. Thom, F.D. Bushman, S.A. Vinogradov, G.D. Wu, Correlation between intraluminal oxygen gradient and radial partitioning of intestinal microbiota, *Gastroenterology* 147(5) (2014) 1055-63.
- [256] M.G. Espey, Role of oxygen gradients in shaping redox relationships between the human intestine and its microbiota, *Free Radic Biol Med* 55 (2013) 130-40.
- [257] W. Liu, S.-M. Shen, X.-Y. Zhao, G.-Q. Chen, Targeted genes and interacting proteins of hypoxia inducible factor-1, *International Journal of Biochemistry and Molecular Biology* 3(2) (2012) 165-178.

- [258] M.L. Lemus-Varela, M.E. Flores-Soto, R. Cervantes-Munguia, B.M. Torres-Mendoza, G. Gudino-Cabrera, V. Chaparro-Huerta, D. Ortuno-Sahagun, C. Beas-Zarate, Expression of HIF-1 alpha, VEGF and EPO in peripheral blood from patients with two cardiac abnormalities associated with hypoxia, *Clinical biochemistry* 43(3) (2010) 234-9.
- [259] J. Leedale, A. Herrmann, J. Bagnall, A. Fercher, D. Papkovsky, V. Sée, R.N. Bearon, Modeling the dynamics of hypoxia inducible factor-1 α (HIF-1 α) within single cells and 3D cell culture systems, *Mathematical Biosciences* 258 (2014) 33-43.
- [260] C.E. Forristal, K.L. Wright, N.A. Hanley, R.O.C. Oreffo, F.D. Houghton, Hypoxia inducible factors regulate pluripotency and proliferation in human embryonic stem cells cultured at reduced oxygen tensions, *Reproduction* (Cambridge, England) 139(1) (2010) 85-97.
- [261] G.L. Semenza, Hypoxia-inducible factors in physiology and medicine, *Cell* 148(3) (2012) 399-408.
- [262] J. Bagnall, J. Leedale, S.E. Taylor, D.G. Spiller, M.R. White, K.J. Sharkey, R.N. Bearon, V. See, Tight control of hypoxia-inducible factor-alpha transient dynamics is essential for cell survival in hypoxia, *J Biol Chem* 289(9) (2014) 5549-64.
- [263] K. Nakayama, Cellular signal transduction of the hypoxia response, *Journal of biochemistry* 146(6) (2009) 757-765.
- [264] P. Vaupel, M. Höckel, A. Mayer, Detection and characterization of tumor hypoxia using pO₂ histography, *Antioxidants & redox signaling* 9(8) (2007) 1221-1236.
- [265] S. McKeown, Defining normoxia, physoxia and hypoxia in tumours—implications for treatment response, *The British journal of radiology* 87(1035) (2014) 20130676.
- [266] G.L. Semenza, Defining the role of hypoxia-inducible factor 1 in cancer biology and therapeutics, *Oncogene* 29(5) (2010) 625-634.
- [267] D. Liao, R.S. Johnson, Hypoxia: a key regulator of angiogenesis in cancer, *Cancer and Metastasis Reviews* 26(2) (2007) 281-290.
- [268] P. Swietach, R.D. Vaughan-Jones, A.L. Harris, Regulation of tumor pH and the role of carbonic anhydrase 9, *Cancer and Metastasis Reviews* 26(2) (2007) 299-310.

- [269] D.A. Chan, A.J. Giaccia, Hypoxia, gene expression, and metastasis, *Cancer and Metastasis Reviews* 26(2) (2007) 333-339.
- [270] B.J. Moeller, R.A. Richardson, M.W. Dewhirst, Hypoxia and radiotherapy: opportunities for improved outcomes in cancer treatment, *Cancer and Metastasis Reviews* 26(2) (2007) 241-248.
- [271] G.L. Semenza, Hypoxia, clonal selection, and the role of HIF-1 in tumor progression, *Critical reviews in biochemistry and molecular biology* 35(2) (2000) 71-103.
- [272] S. Pisarcik, J. Maylor, W. Lu, X. Yun, C. Udem, J. Sylvester, G.L. Semenza, L.A. Shimoda, Activation of hypoxia-inducible factor-1 in pulmonary arterial smooth muscle cells by endothelin-1, *American Journal of Physiology-Lung Cellular and Molecular Physiology* 304(8) (2013) L549-L561.
- [273] E.C. Fletcher, J. Lesske, R. Behm, C.r. Miller, H. Stauss, T. Unger, Carotid chemoreceptors, systemic blood pressure, and chronic episodic hypoxia mimicking sleep apnea, *Journal of Applied Physiology* 72(5) (1992) 1978-1984.
- [274] C. Michiels, Physiological and pathological responses to hypoxia, *The American journal of pathology* 164(6) (2004) 1875-1882.
- [275] M.G. Vander Heiden, L.C. Cantley, C.B. Thompson, Understanding the Warburg effect: the metabolic requirements of cell proliferation, *science* 324(5930) (2009) 1029-1033.
- [276] P. Trayhurn, Hypoxia and adipose tissue function and dysfunction in obesity, *Physiological Reviews* 93(1) (2013) 1-21.
- [277] R. Richards, M.D. Jenkinson, B.J. Haylock, V. See, Cell cycle progression in glioblastoma cells is unaffected by pathophysiological levels of hypoxia, *PeerJ* 4 (2016) e1755.
- [278] R.I. Dmitriev, A.V. Zhdanov, Y.M. Nolan, D.B. Papkovsky, Imaging of neurosphere oxygenation with phosphorescent probes, *Biomaterials* 34(37) (2013) 9307-9317.
- [279] J. Hynes, T.C. O'Riordan, A.V. Zhdanov, G. Uray, Y. Will, D.B. Papkovsky, In vitro analysis of cell metabolism using a long-decay pH-sensitive lanthanide probe and extracellular acidification assay, *Analytical biochemistry* 390(1) (2009) 21-8.

- [280] D. Aigner, R. Dmitriev, S. Borisov, D. Papkovsky, I. Klimant, pH-sensitive perylene bisimide probes for live cell fluorescence lifetime imaging, *Journal of Materials Chemistry B* 2(39) (2014) 6792-6801.
- [281] N.B. Pestov, R.I. Dmitriev, M.B. Kostina, T.V. Korneenko, M.I. Shakhparonov, N.N. Modyanov, Structural evolution and tissue-specific expression of tetrapod-specific second isoform of secretory pathway Ca²⁺-ATPase, *Biochemical and Biophysical Research Communications* 417(4) (2012) 1298-1303.
- [282] P. Lewis, D. Sheehan, R. Soares, A.V. Coelho, K.D. O'Halloran, Chronic sustained hypoxia-induced redox remodeling causes contractile dysfunction in mouse sternohyoid muscle, *Frontiers in physiology* 6 (2015).
- [283] R.I. Dmitriev, A.V. Kondrashina, K. Koren, I. Klimant, A.V. Zhdanov, J.M. Pakan, K.W. McDermott, D.B. Papkovsky, Small molecule phosphorescent probes for O₂ imaging in 3D tissue models, *Biomaterials Science* (2014).
- [284] H.J. Sung, W. Ma, P.-y. Wang, J. Hynes, T.C. O'Riordan, C.A. Combs, J.P. McCoy Jr, F. Bunz, J.-G. Kang, P.M. Hwang, Mitochondrial respiration protects against oxygen-associated DNA damage, *Nature communications* 1 (2010) 5.
- [285] A.V. Zhdanov, R.I. Dmitriev, D.B. Papkovsky, Bafilomycin A1 activates HIF-dependent signalling in human colon cancer cells via mitochondrial uncoupling, *Bioscience reports* 32(6) (2012) 587-595.
- [286] M. Brower, D.N. Carney, H.K. Oie, A.F. Gazdar, J.D. Minna, Growth of cell lines and clinical specimens of human non-small cell lung cancer in a serum-free defined medium, *Cancer Research* 46(2) (1986) 798-806.
- [287] A. Guzman, M.J. Ziperstein, L.J. Kaufman, The effect of fibrillar matrix architecture on tumor cell invasion of physically challenging environments, *Biomaterials* 35(25) (2014) 6954-6963.
- [288] R.I. Dmitriev, D.B. Papkovsky, In vitro ischemia decreases histone H4K16 acetylation in neural cells, *FEBS Letters* 589(1) (2015) 138-144.
- [289] R.I. Dmitriev, D.B. Papkovsky, Multi-parametric O₂ imaging in three-dimensional neural cell models with the phosphorescent probes, *Methods Mol Biol* 1254 (2015) 55-71.
- [290] S. Mukhopadhyay, C. Bachert, D.R. Smith, A.D. Linstedt, Manganese-induced trafficking and turnover of the cis-Golgi glycoprotein GPP130, *Molecular biology of the cell* 21(7) (2010) 1282-1292.

- [291] D. Hutmacher, S. Cool, Concepts of scaffold-based tissue engineering—the rationale to use solid free-form fabrication techniques, *Journal of cellular and molecular medicine* 11(4) (2007) 654-669.
- [292] C.E. Caicedo-Carvajal, Q. Liu, Y. Remache, A. Goy, K.S. Suh, Cancer tissue engineering: a novel 3d polystyrene scaffold for in vitro isolation and amplification of lymphoma cancer cells from heterogeneous cell mixtures, *Journal of tissue engineering* 2(1) (2011).
- [293] M. Schutte, B. Fox, M.-O. Baradez, A. Devonshire, J. Minguez, M. Bokhari, S. Przyborski, D. Marshall, Rat primary hepatocytes show enhanced performance and sensitivity to acetaminophen during three-dimensional culture on a polystyrene scaffold designed for routine use, *Assay and drug development technologies* 9(5) (2011) 475-486.
- [294] J.M. Pakan, K.W. McDermott, A method to investigate radial glia cell behavior using two-photon time-lapse microscopy in an ex vivo model of spinal cord development, *Frontiers in neuroanatomy* 8 (2014).
- [295] M.-H. Wu, J.P.G. Urban, Z.F. Cui, Z. Cui, X. Xu, Effect of Extracellular pH on Matrix Synthesis by Chondrocytes in 3D Agarose Gel, *Biotechnology Progress* 23(2) (2007) 430-434.
- [296] T. Bartosh, Z. Wang, A.A. Rosales, S.D. Dimitrijevic, R.S. Roque, 3D-model of adult cardiac stem cells promotes cardiac differentiation and resistance to oxidative stress, *Journal of cellular biochemistry* 105(2) (2008) 612-623.
- [297] K.A. Foster, F. Galeffi, F.J. Gerich, D.A. Turner, M. Müller, Optical and pharmacological tools to investigate the role of mitochondria during oxidative stress and neurodegeneration, *Progress in neurobiology* 79(3) (2006) 136-171.
- [298] H. Harrington, F. Rose, Y. Reinwald, L. Buttery, A. Ghaemmaghami, J. Aylott, Electrospun PLGA fibre sheets incorporating fluorescent nanosensors: self-reporting scaffolds for application in tissue engineering, *Analytical Methods* 5(1) (2013) 68-71.
- [299] I. Streeter, U. Cheema, Oxygen consumption rate of cells in 3D culture: The use of experiment and simulation to measure kinetic parameters and optimise culture conditions, *Analyst* 136(19) (2011) 4013-4019.
- [300] E. Volkmer, I. Drosse, S. Otto, A. Stangelmayer, M. Stengele, B.C. Kallukalam, W. Mutschler, M. Schieker, Hypoxia in static and dynamic 3D culture

systems for tissue engineering of bone, *Tissue Engineering Part A* 14(8) (2008) 1331-1340.

[301] C. Toncelli, O.V. Arzhakova, A. Dolgova, A.L. Volynskii, N.F. Bakeev, J.P. Kerry, D.B. Papkovsky, Discrete phosphorescent oxygen sensors produced from high density polyethylene films by local solvent-crazing, *Analytical chemistry* (2014).

[302] C. Kelly, C. Toncelli, J. Kerry, D.B. Papkovsky, Phosphorescent O₂ sensors based on polyolefin fabric materials, *Journal of Materials Chemistry C* (2014).

[303] Y. Amao, Probes and Polymers for Optical Sensing of Oxygen, *Microchim. Acta* 143(1) (2003) 1-12.

[304] C.K. Lee, C.E. Diesendruck, E. Lu, A.N. Pickett, P.A. May, J.S. Moore, P.V. Braun, Solvent Swelling activation of a mechanophore in a polymer network, *Macromolecules* 47(8) (2014) 2690-2694.

[305] S. Borisov, G. Nuss, I. Klimant, Red light-excitable oxygen sensing materials based on platinum (II) and palladium (II) benzoporphyrins, *Analytical chemistry* 80(24) (2008) 9435-9442.

[306] C. O'driscoll, A. Gorman, Hypoxia induces neurite outgrowth in PC12 cells that is mediated through adenosine A_{2A} receptors, *Neuroscience* 131(2) (2005) 321-329.

[307] M.F. Czyzyk-Krzeska, B.A. Furnari, E.E. Lawson, D.E. Millhorn, Hypoxia increases rate of transcription and stability of tyrosine hydroxylase mRNA in pheochromocytoma (PC12) cells, *Journal of biological chemistry* 269(1) (1994) 760-764.

[308] M.J. Ruedas-Rama, J.D. Walters, A. Orte, E.A. Hall, Fluorescent nanoparticles for intracellular sensing: a review, *Analytica Chimica Acta* 751 (2012) 1-23.

[309] A. Zhdanov, C. Favre, L. O'Flaherty, J. Adam, R. O'Connor, P. Pollard, D. Papkovsky, Comparative bioenergetic assessment of transformed cells using a cell energy budget platform, *Integrative Biology* 3(11) (2011) 1135-1142.

[310] W. Jarmuszkiewicz, A. Woyda-Ploszczyca, A. Koziel, J. Majerczak, J.A. Zoladz, Temperature controls oxidative phosphorylation and reactive oxygen species production through uncoupling in rat skeletal muscle mitochondria, *Free Radical Biology and Medicine* 83 (2015) 12-20.

- [311] M. Mahmoudi, A.M. Abdelmonem, S. Behzadi, J.H. Clement, S. Dutz, M.R. Ejtehadi, R. Hartmann, K. Kantner, U. Linne, P. Maffre, Temperature: the “ignored” factor at the nanobio interface, *ACS nano* 7(8) (2013) 6555-6562.
- [312] H. Zhou, M. Sharma, O. Berezin, D. Zuckerman, M.Y. Berezin, Nanothermometry: From Microscopy to Thermal Treatments, *ChemPhysChem* 17(1) (2016) 27-36.
- [313] E.A. Repasky, S.S. Evans, M.W. Dewhirst, Temperature matters! And why it should matter to tumor immunologists, *Cancer immunology research* 1(4) (2013) 210-216.
- [314] M. Chakraborty, S. Mukhopadhyay, A. Dasgupta, S. Banerjee, S. Patsa, J. Ray, K. Chaudhuri, A new paradigm of oral cancer detection using digital infrared thermal imaging, *SPIE Medical Imaging, International Society for Optics and Photonics*, 2016, pp. 97853I-97853I-7.
- [315] R. Tanimoto, T. Hiraiwa, Y. Nakai, Y. Shindo, K. Oka, N. Hiroi, A. Funahashi, Detection of Temperature Difference in Neuronal Cells, *Scientific reports* 6 (2016).
- [316] G. Baffou, H. Rigneault, D. Marguet, L. Jullien, A critique of methods for temperature imaging in single cells, *Nature Methods* 11(9) (2014) 899-901.
- [317] J. Jenkins, D. Papkovsky, R. Dmitriev, The Ca²⁺/Mn²⁺-transporting SPCA2 pump is regulated by oxygen and cell density in colon cancer cells, *Biochemical Journal* (2016) BCJ20160477.
- [318] S. Raghavan, M.R. Ward, K.R. Rowley, R.M. Wold, S. Takayama, R.J. Buckanovich, G. Mehta, Formation of stable small cell number three-dimensional ovarian cancer spheroids using hanging drop arrays for preclinical drug sensitivity assays, *Gynecologic oncology* 138(1) (2015) 181-189.
- [319] C.T. Lum, A.S.-T. Wong, M.C. Lin, C.-M. Che, R.W.-Y. Sun, A gold (III) porphyrin complex as an anti-cancer candidate to inhibit growth of cancer-stem cells, *Chemical Communications* 49(39) (2013) 4364-4366.
- [320] R.I. Dmitriev, S.M. Borisov, J. Jenkins, D.B. Papkovsky, Multi-parametric imaging of tumor spheroids with ultra-bright and tunable nanoparticle O₂ probes, *SPIE BiOS, International Society for Optics and Photonics*, 2015, pp. 932806-932806-8.

- [321] A.M. Crane, S.K. Bhattacharya, The use of bromodeoxyuridine incorporation assays to assess corneal stem cell proliferation, *Corneal Regenerative Medicine: Methods and Protocols* (2013) 65-70.
- [322] R. Hunter, Temperature gradients in female reproductive tissues and their potential significance, *Anim Reprod* 6 (2009) 7-15.
- [323] W.A. Denny, Hypoxia-activated prodrugs in cancer therapy: progress to the clinic, *Future Oncology* 6(3) (2010) 419-428.
- [324] J.M. Brown, W.R. Wilson, Exploiting tumour hypoxia in cancer treatment, *Nat Rev Cancer* 4(6) (2004) 437-447.
- [325] A.L. Harris, Hypoxia—a key regulatory factor in tumour growth, *Nature Reviews Cancer* 2(1) (2002) 38-47.
- [326] Y.-A. Chen, A.D. King, H.-C. Shih, C.-C. Peng, C.-Y. Wu, W.-H. Liao, Y.-C. Tung, Generation of oxygen gradients in microfluidic devices for cell culture using spatially confined chemical reactions, *Lab on a Chip* 11(21) (2011) 3626-3633.
- [327] H. Page, P. Flood, E.G. Reynaud, Three-dimensional tissue cultures: current trends and beyond, *Cell and tissue research* 352(1) (2013) 123-131.
- [328] A.V. Zhdanov, R.I. Dmitriev, J. Hynes, D.B. Papkovsky, Kinetic analysis of local oxygenation and respiratory responses of mammalian cells using intracellular oxygen-sensitive probes and time-resolved fluorometry, *Methods in Enzymology* 542 (2013) 183-207.
- [329] M.-Y. Feng, R. Rao, New insights into store-independent Ca(2+) entry: secretory pathway calcium ATPase 2 in normal physiology and cancer, *International Journal of Oral Science* 5(2) (2013) 71-74.
- [330] G.E. Shull, M.L. Miller, V. Prasad, Secretory Pathway Stress Responses as Possible Mechanisms of Disease Involving Golgi Ca(2+) Pump Dysfunction, *Biofactors (Oxford, England)* 37(3) (2011) 150-158.
- [331] B.M. Cross, A. Hack, T.A. Reinhardt, R. Rao, SPCA2 Regulates Orai1 Trafficking and Store Independent Ca(2+) Entry in a Model of Lactation, *PLoS ONE* 8(6) (2013) e67348.
- [332] H.M. Faddy, C.E. Smart, R. Xu, G.Y. Lee, P.A. Kenny, M. Feng, R. Rao, M.A. Brown, M.J. Bissell, S.J. Roberts-Thomson, G.R. Monteith, Localization of plasma membrane and secretory calcium pumps in the mammary gland, *Biochemical and Biophysical Research Communications* 369(3) (2008) 977-981.

- [333] T.A. Reinhardt, J.D. Lippolis, Mammary gland involution is associated with rapid down regulation of major mammary Ca²⁺-ATPases, *Biochemical and Biophysical Research Communications* 378(1) (2009) 99-102.
- [334] L. Dode, J.P. Andersen, J. Vanoevelen, L. Raeymaekers, L. Missiaen, B. Vilsen, F. Wuytack, Dissection of the functional differences between human secretory pathway Ca²⁺/Mn²⁺-ATPase (SPCA) 1 and 2 isoenzymes by steady-state and transient kinetic analyses, *Journal of biological chemistry* 281(6) (2006) 3182-3189.
- [335] M. Brini, E. Carafoli, The plasma membrane Ca²⁺ ATPase and the plasma membrane sodium calcium exchanger cooperate in the regulation of cell calcium, *Cold Spring Harbor perspectives in biology* 3(2) (2011) a004168.
- [336] P. Vangheluwe, M.R. Sepulveda, L. Missiaen, L. Raeymaekers, F. Wuytack, J. Vanoevelen, Intracellular Ca²⁺-and Mn²⁺-transport ATPases, *Chemical reviews* 109(10) (2009) 4733-4759.
- [337] V.C. Culotta, M. Yang, M.D. Hall, Manganese transport and trafficking: lessons learned from *Saccharomyces cerevisiae*, *Eukaryotic Cell* 4(7) (2005) 1159-1165.
- [338] K.K. Kumar, J.E.W. Lowe, A.A. Aboud, M.D. Neely, R. Redha, J.A. Bauer, M. Odak, C.D. Weaver, J. Meiler, M. Aschner, A.B. Bowman, Cellular manganese content is developmentally regulated in human dopaminergic neurons, *Sci. Rep.* 4 (2014).
- [339] M. Coassin, F. Ursini, A. Bindoli, Antioxidant effect of manganese, *Archives of biochemistry and biophysics* 299(2) (1992) 330-333.
- [340] Y.-S. Ho, R. Vincent, M.S. Dey, J.W. Slot, J.D. Crapo, Transgenic Models for the Study of Lung Antioxidant Defense: Enhanced Manganese-containing Superoxide Dismutase Activity Gives Partial Protection to B6C3 Hybrid Mice Exposed to Hyperoxia, *American Journal of Respiratory Cell and Molecular Biology* 18(4) (1998) 538-547.
- [341] A.N. Jensen, L.T. Jensen, Manganese Transport, Trafficking and Function in Invertebrates, (2014).
- [342] A. Takeda, Manganese action in brain function, *Brain Research Reviews* 41(1) (2003) 79-87.

- [343] K. Tuschl, P.B. Mills, P.T. Clayton, Chapter Twelve - Manganese and the Brain, in: P.B. Kailash, A.S. Susanne (Eds.), *International Review of Neurobiology*, Academic Press 2013, pp. 277-312.
- [344] V.A. Fitsanakis, M. Aschner, The importance of glutamate, glycine, and γ -aminobutyric acid transport and regulation in manganese, mercury and lead neurotoxicity, *Toxicology and Applied Pharmacology* 204(3) (2005) 343-354.
- [345] P. Zhao, W. Zhong, X. Ying, Z. Yuan, J. Fu, Z. Zhou, Manganese chloride-induced G0/G1 and S phase arrest in A549 cells, *Toxicology* 250(1) (2008) 39-46.
- [346] D. Bernard, B. Quatannens, A. Begue, B. Vandebunder, C. Abbadie, Antiproliferative and antiapoptotic effects of crel may occur within the same cells via the up-regulation of manganese superoxide dismutase, *Cancer Research* 61(6) (2001) 2656-2664.
- [347] J. Vanoevelen, L. Dode, K. Van Baelen, R.J. Fairclough, L. Missiaen, L. Raeymaekers, F. Wuytack, The secretory pathway $\text{Ca}^{2+}/\text{Mn}^{2+}$ -ATPase 2 is a Golgi-localized pump with high affinity for Ca^{2+} ions, *Journal of biological chemistry* 280(24) (2005) 22800-22808.
- [348] J. Fandrey, S. Frede, W. Jelkmann, Role of hydrogen peroxide in hypoxia-induced erythropoietin production, *Biochem. J* 303 (1994) 507-510.
- [349] E.C. Vaux, E. Metzen, K.M. Yeates, P.J. Ratcliffe, Regulation of hypoxia-inducible factor is preserved in the absence of a functioning mitochondrial respiratory chain, *Blood* 98(2) (2001) 296-302.
- [350] V.C. Garside, A.S. Kowalik, C.L. Johnson, D. DiRenzo, S.F. Konieczny, C.L. Pin, MIST1 Regulates the Pancreatic Acinar Cell Expression of Atp2c2, the gene encoding Secretory Pathway Calcium ATPase 2, *Experimental Cell Research* 316(17) (2010) 2859-2870.
- [351] M.A. Fenech, C.M. Sullivan, L.T. Ferreira, R. Mehmood, W.A. MacDonald, P.B. Stathopoulos, C.L. Pin, Atp2c2 Is Transcribed From a Unique Transcriptional Start Site in Mouse Pancreatic Acinar Cells, *Journal of Cellular Physiology* (2016).
- [352] C.L. Pin, A.C. Bonvissuto, S.F. Konieczny, Mist1 expression is a common link among serous exocrine cells exhibiting regulated exocytosis, *The Anatomical Record* 259(2) (2000) 157-167.
- [353] I. Vandecaetsbeek, P. Vangheluwe, L. Raeymaekers, F. Wuytack, J. Vanoevelen, The Ca^{2+} pumps of the endoplasmic reticulum and Golgi apparatus, *Cold Spring Harbor perspectives in biology* 3(5) (2011) a004184.

- [354] T.A. Reinhardt, J.D. Lippolis, R.E. Sacco, The Ca²⁺/H⁺ antiporter TMEM165 expression, localization in the developing, lactating and involuting mammary gland parallels the secretory pathway Ca²⁺ ATPase (SPCA1), *Biochemical and Biophysical Research Communications* 445(2) (2014) 417-421.
- [355] H. Yang, Q. Zhang, J. He, W. Lu, Regulation of calcium signaling in lung cancer, *Journal of Thoracic Disease* 2(1) (2010) 52-56.
- [356] B.R. O'Donnell, P.E. Bickler, Influence of pH on calcium influx during hypoxia in rat cortical brain slices, *Stroke* 25(1) (1994) 171-177.
- [357] W.T. Mason, *Fluorescent and luminescent probes for biological activity: a practical guide to technology for quantitative real-time analysis*, Academic Press 1999.
- [358] O.S. Wolfbeis, Fiber-optic chemical sensors and biosensors, *Analytical chemistry* 76(12) (2004) 3269-3284.
- [359] A.V. Zhdanov, V.I. Ogurtsov, C.T. Taylor, D.B. Papkovsky, Monitoring of cell oxygenation and responses to metabolic stimulation by intracellular oxygen sensing technique, *Integrative Biology* 2(9) (2010) 443-451.
- [360] A.V. Kondrashina, R.I. Dmitriev, S.M. Borisov, I. Klimant, I. O'Brien, Y.M. Nolan, A.V. Zhdanov, D.B. Papkovsky, A phosphorescent nanoparticle-based probe for sensing and imaging of (intra) cellular oxygen in multiple detection modalities, *Advanced Functional Materials* 22(23) (2012) 4931-4939.
- [361] R.I. Dmitriev, S.M. Borisov, A.V. Kondrashina, J.M. Pagan, U. Anilkumar, J.H. Prehn, A.V. Zhdanov, K.W. McDermott, I. Klimant, D.B. Papkovsky, Imaging oxygen in neural cell and tissue models by means of anionic cell-permeable phosphorescent nanoparticles, *Cell. Mol. Life Sci.* 72(2) (2015) 367-381.
- [362] H.D. Duong, J.I. Rhee, Exploitation of thermo-effect of rhodamine B entrapped in sol-gel matrix and silica gel for temperature detection, *Sensors and Actuators B: Chemical* 124(1) (2007) 18-23.
- [363] D. Ross, M. Gaitan, L.E. Locascio, Temperature measurement in microfluidic systems using a temperature-dependent fluorescent dye, *Analytical chemistry* 73(17) (2001) 4117-4123.
- [364] R.I. Dmitriev, A.V. Zhdanov, G. Jasionek, D.B. Papkovsky, Assessment of cellular oxygen gradients with a panel of phosphorescent oxygen-sensitive probes, *Analytical chemistry* 84(6) (2012) 2930-2938.

- [365] A. Nimmerjahn, F. Helmchen, In vivo labeling of cortical astrocytes with sulforhodamine 101 (SR101), Cold Spring Harbor protocols 2012(3) (2012) pdb. prot068155.
- [366] L. Jamieson, D.J. Harrison, C. Campbell, Chemical analysis of multicellular tumour spheroids, Analyst 140(12) (2015) 3910-3920.
- [367] S. Arai, M. Suzuki, S.-J. Park, J.S. Yoo, L. Wang, N.-Y. Kang, H.-H. Ha, Y.-T. Chang, Mitochondria-targeted fluorescent thermometer monitors intracellular temperature gradient, Chemical Communications 51(38) (2015) 8044-8047.
- [368] R. Battino, T.R. Rettich, T. Tominaga, The solubility of oxygen and ozone in liquids, Journal of physical and chemical reference data 12(2) (1983) 163-178.
- [369] J.A. Kim, Y. Kim, B.-M. Kwon, D.C. Han, The natural compound cantharidin induces cancer cell death through inhibition of heat shock protein 70 (HSP70) and Bcl-2-associated athanogene domain 3 (BAG3) expression by blocking heat shock factor 1 (HSF1) binding to promoters, Journal of Biological Chemistry 288(40) (2013) 28713-28726.
- [370] G.L. Semenza, Hypoxia and cancer, Cancer and Metastasis Reviews 26(2) (2007) 223.
- [371] L. Zheng, C.J. Kelly, S.P. Colgan, Physiologic hypoxia and oxygen homeostasis in the healthy intestine. A Review in the Theme: Cellular Responses to Hypoxia, American Journal of Physiology-Cell Physiology 309(6) (2015) C350-C360.
- [372] E.H. Sarsour, A.L. Kalen, P.C. Goswami, Manganese superoxide dismutase regulates a redox cycle within the cell cycle, Antioxidants & redox signaling 20(10) (2014) 1618-1627.

9. Acknowledgements

I would like to thank the many people who made this thesis possible.

I would like to express my gratitude to my supervisor Prof. Dmitri Papkovsky for giving me the opportunity to complete my PhD in his lab and for his support and advice during my time in Cork.

A big thank you to my Co-supervisor Dr. Ruslan Dmitriev, for all his help with experimental plans and ideas, practical help and drive when it came to publishing papers.

I want to extend a massive thank you to the other lab members who provided a fun friendly environment, providing much needed encouragement Neil, Irina, Selina Alicia, Alex, Barbara, Caroline.

Finally, I want to thank my family, who made this possible, for their encouragement, patience and endless support that allowed me to progress this far in my academic career.

***SFI, IPIC - Thesis funding**